UNIVERSITÀ DEGLI STUDI DI MILANO
FACOLTÀ DI SCIENZE MATEMATICHE, FISICHE E NATURALI
DOTTORATO DI RICERCA IN
FISICA, ASTROFISICA E FISICA APPLICATA

MEASUREMENT OF BRANCHING FRACTIONS OF B DECAYS TO $K_1(1270)\pi$ AND $K_1(1400)\pi$ AND DETERMINATION OF THE CKM ANGLE α FROM $B^0 \to a_1(1260)^{\pm}\pi^{\mp}$

Settore Scientifico Disciplinare FIS/04

Coordinatore: Prof. Marco Bersanelli
Tutore: Prof. Fernando Palombo
Cotutore: Prof. Stefano Forte

Tesi di Dottorato di:
Simone Stracka
Ciclo XXIII

Anno Accademico 2009-2010

To my parents

Contents

Introduction

In the Standard Model, *CP* violation in weak interactions involving quarks is parameterized by an irreducible complex phase in the Cabibbo-Kobayashi-Maskawa (CKM) quark-mixing-matrix. The precise determination of the CKM elements is a necessary ingredient for a stringent test of the Standard Model predictions, and is a crucial input for reducing the theoretical error in many New Physics searches with flavor, e.g., in the kaon sector.

The unitarity of the CKM matrix is typically expressed as a triangle relationship among its parameters, where the area of the so-called Unitarity Triangle visually depicts the amount of asymmetry between the decays of B particles and their antimatter counterparts. In the past few years, the *BABAR* and Belle experiments have been able to measure all three angles of the triangle from *CP* asymmetry measurements. The first asymmetry measurements in B particle decays, about ten years ago, allowed to determine β, which is now known to better than 5% precision. The angles α and γ, measured in much rarer processes, required several years of data taking before analyses could yield reliable answers. A remarkable feature is that the direct measurement of the angles of the Unitarity Triangle generates an area that is consistent with the area predicted by measurement of the sides.

The determination of α from time-dependent *CP* asymmetries in $b \to u\bar{u}d$ tree-dominated modes (such as $B \to \pi\pi$, $\rho\pi$, $\rho\rho$, and $a_1(1260)\pi$) is complicated by the fact that penguin (i.e., loop) contributions may be large, and occur with a different CKM phase than tree amplitudes. While the prospects for observing direct *CP* violation in these channels improve, in order to overcome penguin pollution and extract α cleanly one needs to introduce symmetry arguments, and use the measurements of a set of auxiliary B decay channels as an input. One of the strengths of the B-factories lies in their ability to use multiple approaches to the measurement of α, allowing the refinement of theoretical model-dependent estimates of the penguin and tree contributions by comparison with data in many channels. Independent measurements of this angle in different channels also provide a means to resolve discrete ambiguities that may emerge in the extraction of α. Finally, exploring the full spectrum of possible α determinations at B-factories can inform the strategies to measure this angle at other facilities.

Contrary to the $\sin 2\beta$ case, no theoretically and experimentally clean golden mode has been identified for the measurement of α. Until recently, α had been measured in $B \to \pi\pi$, $\rho\pi$, and $\rho\rho$ decays only. In addition to these modes, the time-dependent analysis of the decay $B^0 \to a_1(1260)^{\pm}\pi^{\mp}$ can also be used to extract an effective phase $\alpha_{\rm eff}$, which is equal to the weak phase α in the limit of vanishing penguin amplitudes. The effect of penguin contributions can be determined from the measurements of the branching fractions of the $B \to a_1(1260)K$, $B \to K_1(1270)\pi$, and $B \to K_1(1400)\pi$ decays. The $B \to a_1(1260)K$ decays have been recently observed by *BABAR*.

This dissertation describes the first observation of neutral B meson decays to $K_1(1270)\pi$ and $K_1(1400)\pi$ with the *BABAR* experiment. The analysis also includes the first measure-

ment of the branching fractions of $B^+ \to K_1(1270)^0\pi^+$ and $B^+ \to K_1(1400)^0\pi^+$ decays. The branching fractions in this modes provide the missing piece of input to constrain the model uncertainty due to penguin pollution in the extraction of α in the $B^0 \to a_1(1260)^{\pm}\pi^{\mp}$ channel.

In Chapter 1, I describe the CKM paradigm of *CP* violation, and report the current status of the measurement of the CKM angles. The theoretical background on the extraction of α in the $B^0 \to a_1(1260)^{\pm}\pi^{\mp}$ channel is also provided. In Chapter 2, an overview of the PEP-II accelerator and the *BABAR* detector, which collected the data on which this work is based, is presented. In Chapter 3, I introduce the K-matrix formalism used for the parameterization of the K_1 resonances. Chapter 4 is devoted to a discussion of the discriminating variables used in the reconstruction and selection of the B candidates. The analyses of charged and neutral B meson decays to $K_1(1270)\pi$ and $K_1(1400)\pi$ are reported in Chapter 5. Finally, in Chapter 6, I use the experimental results to extract bounds on the penguin-induced shifts in α.

Chapter 1

The CKM matrix and the Unitarity Triangle

In the Standard Model (SM) of electroweak interactions based on the $SU(2)_L \times U(1)_Y$ symmetry [1], *CP* violation in quark sector with three generations arises from a single irremovable phase in the mixing matrix describing the couplings of the charged W gauge bosons to the quarks [2, 3].

Charged current weak interactions can be written as

$$\mathcal{L}_W = -\frac{g}{\sqrt{2}} \left(\bar{u} \quad \bar{c} \quad \bar{t}\right)_L \gamma^\mu V \begin{pmatrix} d \\ s \\ b \end{pmatrix}_L W_\mu^+ + \text{h.c.}, \tag{1.1}$$

where g is the $SU(2)_L$ coupling constant, W_μ is the W boson field operator, and $\{u, c, t\}_L$ and $\{d, s, b\}_L$ are the left-handed quark field flavor eigenstates, with charges $Q = 2/3$ and $Q = -1/3$ respectively. The matrix of the couplings, called the Cabibbo-Kobayashi-Maskawa (CKM) matrix,

$$V = \begin{pmatrix} V_{ud} & V_{us} & V_{ub} \\ V_{cd} & V_{cs} & V_{cb} \\ V_{td} & V_{ts} & V_{tb} \end{pmatrix}, \tag{1.2}$$

is a 3×3 unitary matrix ($VV^\dagger = V^\dagger V = I$), thus depending on nine parameters, three real angles and six phases. The number of phases can be reduced to one by a redefinition of the phases of the quark fields. An explicit "standard parameterization" in terms of three mixing angles θ_{12}, θ_{13}, θ_{23}, and a phase δ, with a particular quark fields phase convention, is [4]

$$V = \begin{pmatrix} c_{12}c_{13} & s_{12}c_{13} & s_{13}e^{-i\delta} \\ -s_{12}c_{23} - c_{12}s_{23}s_{13}e^{i\delta} & c_{12}c_{23} - s_{12}s_{23}s_{13}e^{i\delta} & s_{23}c_{13} \\ s_{12}s_{23} - c_{12}c_{23}s_{13}e^{i\delta} & -c_{12}s_{23} - s_{12}c_{23}s_{13}e^{i\delta} & c_{23}c_{13} \end{pmatrix}, \tag{1.3}$$

where $c_{ij} \equiv \cos\theta_{ij}$ and $s_{ij} \equiv \sin\theta_{ij}$, $0 \leq \theta_{ij} \leq \pi/2$, and $0 \leq \delta \leq 2\pi$.

Following the experimental observation of a hierarchy $s_{13} \ll s_{23} \ll s_{12} \ll 1$ between the mixing angles [5]

$$|V_{ij}| = \begin{pmatrix} 0.97428 \pm 0.00015 & 0.2253 \pm 0.0007 & 0.00347^{+0.00016}_{-0.00012} \\ 0.2252 \pm 0.0007 & 0.97345^{+0.00015}_{-0.00016} & 0.0410^{+0.0011}_{-0.0007} \\ 0.00862^{+0.00026}_{-0.00020} & 0.0403^{+0.0011}_{-0.0007} & 0.999152^{+0.000030}_{-0.000045} \end{pmatrix}, \tag{1.4}$$

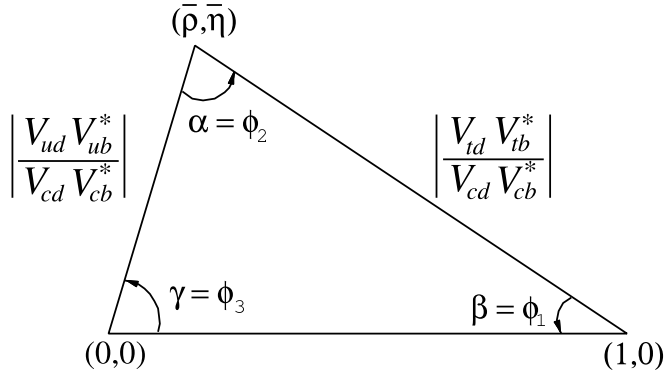

Figure 1.1: Sketch of the unitarity triangle [5].

Wolfenstein proposed an expansion of the CKM matrix in terms of the Cabibbo parameter $\lambda \simeq |V_{us}| \approx 0.23$ [6]. The following definitions of the real parameters A, λ, η, ρ ($\bar{\eta}$, $\bar{\rho}$) are used:

$$s_{12} \equiv \lambda, \quad s_{23} \equiv A\lambda^2, \quad s_{13}e^{-i\delta} \equiv \frac{A\lambda^3}{1-\lambda^2/2}(\rho - i\eta) \equiv \frac{A\lambda^3(\bar{\rho} - i\bar{\eta})\sqrt{1-A^2\lambda^4}}{\sqrt{1-\lambda^2}[1 - A^2\lambda^4(\bar{\rho} - i\bar{\eta})]}, \quad (1.5)$$

which ensure that $\bar{\rho} + i\bar{\eta} = -(V_{ud}V_{ub}^*)/(V_{cd}V_{cb}^*)$ is phase-convention-independent.

The Wolfenstein representation of V is easily derived:

$$V = \begin{pmatrix} 1-\lambda^2/2 & \lambda & A\lambda^3(\rho - i\eta) \\ -\lambda & 1-\lambda^2/2 & A\lambda^2 \\ A\lambda^3(1-\rho-i\eta) & -A\lambda^2 & 1 \end{pmatrix} + O(\lambda^4).$$

Unitarity of the CKM matrix V requires that $V_{ji}^*V_{jk} = V_{ij}^*V_{kj} = \delta_{ik}$. Of particular relevance is the relation

$$V_{ub}^*V_{ud} + V_{cb}^*V_{cd} + V_{tb}^*V_{td} = 0, \quad (1.6)$$

which describes the so-called Unitarity Triangle (UT), typically used to pictorially represent the irreducible *CP* violating phase as its sides are nearly of the same order of magnitude in length. The UT can be rotated by a conventional phase so that $V_{cb}^*V_{cd}$ is real, and scaled by dividing the length of all sides by $|V_{cd}^*V_{cb}|$. As shown in Fig. 1.1, two vertices have coordinates $(0,0)$ e $(1,0)$, while the coordinates of the third vertex (apex) in terms of the Wolfenstein parameters are, neglecting terms of order λ^4, given by $(\bar{\rho}, \bar{\eta})$.

The lengths of the two complex sides are

$$\left|\frac{V_{ub}^*V_{ud}}{V_{cb}^*V_{cd}}\right| = \sqrt{\bar{\rho}^2 + \bar{\eta}^2} = \frac{1 - \lambda^2/2 + O(\lambda^4)}{\lambda}\left|\frac{V_{ub}}{V_{cb}}\right|, \quad (1.7)$$

$$\left|\frac{V_{tb}^*V_{td}}{V_{cb}^*V_{cd}}\right| = \sqrt{(1-\bar{\rho})^2 + \bar{\eta}^2} = \frac{1 + O(\lambda^4)}{\lambda}\left|\frac{V_{td}}{V_{cb}}\right|. \quad (1.8)$$

The three angles, denoted by α, β, and γ, are defined as

$$\alpha \equiv \arg\left[-\frac{V_{tb}^*V_{td}}{V_{ub}^*V_{ud}}\right], \quad \beta \equiv \arg\left[-\frac{V_{cb}^*V_{cd}}{V_{tb}^*V_{td}}\right], \quad \gamma \equiv \arg\left[-\frac{V_{ub}^*V_{ud}}{V_{cb}^*V_{cd}}\right]. \quad (1.9)$$

Information on the angles α, β and γ can be obtained from the measurement of *CP*-violating B_u and B_d decays. The redundant measurement of these quantities in several processes involving B-meson decays constitute a consistency check of the validity of the SM.

1.1 The B meson system

The light $B \equiv B_{u,d}$ mesons consist of the four pseudoscalar ($J^P = 0^-$) mesons

$$B^+ = u\bar{b}, \qquad B^0 = d\bar{b}, \tag{1.10}$$

$$B^- = \bar{u}b, \qquad \overline{B}^0 = \bar{d}b, \tag{1.11}$$

with masses $m_{B^+} = 5279.1 \pm 0.4$ MeV/c^2 and $m_{B^0} = 5279.5 \pm 0.5$ MeV/c^2, and mean lives of the order of 1.6 ps ($\tau_{B^+} = 1.638 \pm 0.011$ ps, $\tau_{B^0} = 1.525 \pm 0.009$ ps) [5].

1.1.1 Mixing of neutral mesons

Due to the presence of non-flavor-conserving weak processes, the effective Hamiltonian of the $B^0\overline{B}^0$ system is not diagonal in the $\{B^0, \overline{B}^0\}$ base, so that mixing effects occur. For a weakly-decaying neutral meson X^0 (e.g. K^0, D^0, B_d or B_s) an arbitrary linear combination of the flavor eigenstates

$$a|X^0\rangle + b|X^0\rangle \tag{1.12}$$

mixes according to the time-dependent Schrödinger equation

$$i\frac{\partial}{\partial t}\begin{pmatrix} a \\ b \end{pmatrix} = H_{\text{eff}}\begin{pmatrix} a \\ b \end{pmatrix}, \tag{1.13}$$

with

$$H_{\text{eff}} = \begin{pmatrix} H_0 & H_{12} \\ H_{21} & H_0 \end{pmatrix} = M - i\frac{\Gamma}{2} = \begin{pmatrix} M_0 & M_{12} \\ M_{12}^* & M_0 \end{pmatrix} - \frac{i}{2}\begin{pmatrix} \Gamma_0 & \Gamma_{12} \\ \Gamma_{12}^* & \Gamma_0 \end{pmatrix}, \tag{1.14}$$

where the M and Γ matrices describe the mixing and decay of the neutral mesons, respectively. Assuming CPT invariance implies $H_{11} = H_{22}$, $M_{21} = M_{12}^*$ and $\Gamma_{21} = \Gamma_{12}^*$. Each of the off-diagonal elements can be complex: the angle in the complex plane of M_{12} represents the phase of the mixing, while Γ_{12} represents the (complex) coupling of X^0 and $\bar{X}^0$ to common decay modes (for example, $B^0/\bar{B}^0 \to J/\psi K_S^0$ or $\pi^+\pi^-$).

The mass eigenstates are the eigenvectors of the effective Hamiltonian H_{eff}

$$\begin{aligned} |X_L\rangle &= p|X^0\rangle + q|\bar{X}^0\rangle \\ |X_H\rangle &= p|X^0\rangle - q|\bar{X}^0\rangle \end{aligned} \tag{1.15}$$

where $|X_L\rangle$ and $|X_H\rangle$ are the lighter and heavier mass eigenstates, and p and q are complex numbers:

$$\frac{q}{p} = \sqrt{\frac{M_{12}^* - \frac{i}{2}\Gamma_{12}^*}{M_{12} - \frac{i}{2}\Gamma_{12}}}; \quad \sqrt{|p|^2 + |q|^2} = 1. \tag{1.16}$$

The eigenvalues λ_L e λ_H of Eq. (1.14) are:

$$\lambda_L = M_L - i\frac{\Gamma_L}{2}, \quad \lambda_H = M_H - i\frac{\Gamma_H}{2}. \tag{1.17}$$

where M_L and M_H are the masses of the eigenstates $|X_L\rangle$ and $|X_H\rangle$, respectively, and Γ_L and Γ_H their widths. We define

$$M_d \equiv \frac{M_H + M_L}{2} = M_0, \quad \Gamma_d \equiv \frac{\Gamma_H + \Gamma_L}{2} = \Gamma_0. \tag{1.18}$$

We now specialize to the case of the B_d system. The evaluation of the Standard Model amplitudes for the $|\Delta B| = 2$ process $B^0 \leftrightarrow \overline{B}^0$, determined at quark level by the box diagrams $(b\bar{d}) \leftrightarrow (\bar{b}d)$ (Fig. 1.2), leads to [7]:

$$\left|\frac{\Gamma_{12}}{M_{12}}\right| = O\left(\frac{m_b^2}{m_t^2}\right) \ll 1, \tag{1.19}$$

$$\Delta M_d \equiv \frac{M_H - M_L}{2} = 2|M_{12}|, \tag{1.20}$$

$$\Delta\Gamma_d \equiv \frac{\Gamma_H - \Gamma_L}{2} \approx -2|\Gamma_{12}|, \tag{1.21}$$

$$\frac{q}{p} \approx e^{-2i\beta}, \tag{1.22}$$

where in the last line the same quark field phase convention adopted for the standard parameterization of the CKM matrix has been used, and we have made the phase choice $CP(B^0) = \overline{B}^0$.

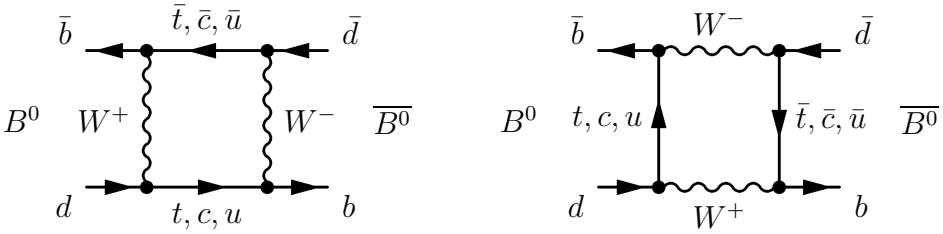

Figure 1.2: Feynman diagrams mixing $B^0 - \overline{B}^0$.

Here, the lifetime difference $\Delta\Gamma_d$ between the two mass eigenstates is small compared with the mixing frequency ($\Delta\Gamma_d/\Delta M_d = O(10^{-2}) \ll 1$). Since $\Delta M_d/\Gamma_d$ has been measured to be (0.774 ± 0.008), then $|\Delta\Gamma_d|/\Gamma_d = 0.009 \pm 0.037 \ll 1$. This is due to the large mass of the B meson and thus great available phase space for flavor-specific decays, which dominate the partial width (in contrast, e.g., to the neutral K system) and give equivalent contributions (by CPT symmetry) to the width of both neutral B eigenstates. The resulting lack of decay suppression of either eigenstate implies nearly equivalent lifetimes.

$q/p \approx e^{-2i\beta}$ is almost a pure phase, and the expected deviation of $|q/p|$ from 1 is $|q/p| - 1 \approx 5 \times 10^{-4}$ [7]. The time evolution of neutral B mesons which are initially created (at time $t = 0$) as pure flavor eigenstates can be written as:

$$|B^0_{phys}(t)\rangle = f_+(t)|B^0\rangle + (q/p)f_-(t)|\overline{B}^0\rangle \tag{1.23}$$

$$|\overline{B}^0_{phys}(t)\rangle = f_+(t)|\overline{B}^0\rangle + (p/q)f_-(t)|B^0\rangle \tag{1.24}$$

where, neglecting $\Delta\Gamma_d/\Gamma_d$, the functions $f_\pm(t)$ are

$$f_+(t) = e^{-iM_d t}e^{-\Gamma_d t/2}\cos(\Delta M_d t/2), \tag{1.25}$$

$$f_-(t) = e^{-iM_d t}e^{-\Gamma_d t/2} i \sin(\Delta M_d t/2). \tag{1.26}$$

At the B factories, the $B^0\overline{B}^0$ pair originating from the $e^+e^- \to \Upsilon(4S) \to B^0\overline{B}^0$ process is produced in a coherent $L = 1$ state

$$S(t = 0) = \frac{B^0\overline{B}^0 - \overline{B}^0 B^0}{\sqrt{2}}. \tag{1.27}$$

The time evolution of the two B mesons is then such that at any time, until one particle decays, there is exactly one B^0 and one $\overline{B}^0$:

$$S(t) = e^{-2iM_d t} e^{-\Gamma_d t} \frac{B^0\overline{B}^0 - \overline{B}^0 B^0}{\sqrt{2}}. \tag{1.28}$$

As soon as one of the two B mesons decays to a final state that is accessible only to B^0 or $\overline{B}^0$, the other follows a time evolution given by Eqs. 1.23 and 1.24, where t is now the difference between its proper time and the decay instant of the former B.

1.2 *CP* violation in B decays

Three types of *CP* violation can potentially be observed at B physics experiments:

1. *CP* violation in decay (often referred to as direct *CP* violation): this occurs when multiple amplitudes with different weak phases as well as different strong phases contribute to a given final state; the result is visible as differing magnitude of the amplitude of a decay versus its *CP* conjugate.

2. *CP* violation purely in mixing (or indirect *CP* violation): this occurs when the mass eigenstates of a neutral meson are different from the *CP* eigenstates.

3. *CP* violation in the interference between decays of mixed and unmixed mesons (or in the interference between mixing and decay): this occurs for decays which are common to a neutral meson and its antiparticle.

1.2.1 *CP* violation in decay

CP violation in decay is observed as the difference between the decay rate of a particle to a final state and the decay rate of its antiparticle to the corresponding charge-conjugate final state, and can occur for both neutral and charged B meson decays. It is usually expressed as a branching-fraction asymmetry

$$A_{CP} \equiv \frac{\mathcal{B}(\overline{B} \to \overline{f}) - \mathcal{B}(B \to f)}{\mathcal{B}(\overline{B} \to \overline{f}) + \mathcal{B}(B \to f)} = \frac{|\overline{A}_{\overline{f}}|^2 - |A_f|^2}{|\overline{A}_{\overline{f}}|^2 + |A_f|^2}, \tag{1.29}$$

where $\overline{A}_{\overline{f}}$ and A_f are the total $\overline{B} \to \overline{f}$ and $B \to f$ decay amplitudes, respectively:

$$A_f = \sum_i |A_i| e^{i(\phi_i + \delta_i)}, \qquad \overline{A}_{\overline{f}} = \eta_{CP} \sum_i |A_i| e^{i(-\phi_i + \delta_i)}, \tag{1.30}$$

where η_{CP} is the *CP* eigenvalue, ϕ are the weak phases (i.e., phases that change sign under *CP*), and δ are the strong phases (i.e., phases that do not change sign under *CP*). *CP* violation can only occur if there are at least two interfering processes contributing to the total decay amplitude with non-equal weak and strong phases, so that the numerator of the asymmetry is nonzero:

$$|\overline{A}_{\overline{f}}|^2 - |A_f|^2 = 2\eta_{CP} \sum_{i,j} |A_i||A_j| \sin(\phi_i - \phi_j) \sin(\delta_i - \delta_j). \tag{1.31}$$

1.2.2 *CP* violation in mixing

The mixing formalism for neutral mesons has been discussed in Sec. 1.1.1. *CP* violation occurs when $|q/p| \neq 1$, which can be clearly understood as a difference in how B^0 and $\overline{B}^0$ mesons mix. This type of *CP* violation is negligibly small in the B system, the currently best measurements giving $|q/p| = 1.0002 \pm 0.0028$ [8], which is consistent with unity.

1.2.3 *CP* violation in interference between decay and mixing

Final states which may be reached from either B^0 or $\overline{B}^0$ decays may exhibit a third type of *CP* violation, which results from the interference between the direct decay of the meson into the final state and the alternate path of first mixing into the anti-meson and then decaying into the final state. Both q/p and $\overline{A}_f/A_f$, representing the contribution from mixing and from the decay amplitudes, respectively, appear in the expression for the quantity

$$\lambda_f \equiv \eta_{CP} \frac{q}{p} \frac{\overline{A}_f}{A_f}, \tag{1.32}$$

where η_{CP} is the *CP* eigenvalue of the final state. When $|\lambda_{CP}| = 1$, *CP* violation may result from $\lambda_{CP} \neq 1$ ($\mathrm{Im}(\lambda_{CP}) \neq 0$), even if $|q/p| = 1$ and $|\overline{A}_f/A_f| = 1$, i.e., there is no *CP* violation in either mixing or decay. This case corresponds to *CP* violation in the interference between decays to the final state f with and without mixing. This effect can be observed experimentally only in the difference in the time-dependent decay rates of B^0 and $\overline{B}^0$ mesons:

$$\begin{aligned} A_{CP}(t) &\equiv \frac{\Gamma(\overline{B}^0 \to f)(t) - \Gamma(B^0 \to f)(t)}{\Gamma(\overline{B}^0 \to f)(t) + \Gamma(B^0 \to f)(t)}, & (1.33)\\ &= \frac{2\,\mathrm{Im}(\lambda_f)}{1+|\lambda_f|^2} \sin(\Delta M_d t) - \frac{1-|\lambda_f|^2}{1+|\lambda_f|^2} \cos(\Delta M_d t), & (1.34)\\ &= S \sin(\Delta M_d t) - C \cos(\Delta M_d t), & (1.35) \end{aligned}$$

where ΔM_d is the $B^0 - \overline{B}^0$ mixing frequency. The coefficient S quantifies *CP* violation in decay-mixing interference, while C is a measure of direct *CP* violation. (The direct *CP* asymmetry $A_{CP} = C$.) By construction, the two parameters satisfy the relation $S^2 + C^2 \leq 1$, equivalent to the trivial condition $|Im(\lambda_f)| \leq |\lambda_f|$.

1.3 Measurement of β

The decay amplitudes for the modes $b \to c\bar{c}s$ $b \to s\bar{s}s$ and $b \to c\bar{c}d$ are related to the angle β.

$$\begin{aligned} A(c\bar{c}s) &= V_{cb}V_{cs}^*(T + P^c - P^t) + V_{ub}V_{us}^*(P^u - P^t) & (1.36)\\ A(s\bar{s}s) &= V_{cb}V_{cs}^*(P^c - P^t) + V_{ub}V_{us}^*(P^u - P^t) & (1.37)\\ A(u\bar{u}s) &= V_{cb}V_{cs}^*(P^c - P^t) + V_{ub}V_{us}^*(T + P^u - P^t) & (1.38) \end{aligned}$$

where the unitarity (GIM) relations among the CKM elements have been used to express $V_{tb}V_{ts}^*$ in terms of $V_{ub}V_{us}^*$ and $V_{cb}V_{cs}^*$.

Here, T is the contribution of the tree diagrams, excluding the CKM factors. Similarly, P^q are the q-mediated penguin contributions, excluding the CKM factors. The term $V_{ub}V_{us}^*$ carries a phase $e^{-i\gamma}$ relative to $V_{cb}V_{cs}^*$, but is doubly Cabibbo-suppressed by a factor $\lambda^2 = 0.0513 \pm 0.0005$, so that the impact on the *CP* violation observables is negligible. The gluonic and electroweak penguins have the same phase structure. In addition, the electroweak penguin contribution is typically of order $O(10\%)$ of the gluonic contributions [9]. β can therefore be cleanly extracted, up to a two-fold ambiguity in the range $[0, 180]^\circ$, from the coefficient S of the $\sin(\Delta M_d \Delta t)$ term in the time-dependent *CP* asymmetry (Eq. 1.33).

1.3.1 $b \to c\bar{c}s$ decays

The angle β of the Unitarity Triangle can be accurately measured from the time-dependent *CP* asymmetry (Eq. 1.33) in the "golden modes" $f = (c\bar{c})K^0$, such as $J/\psi K_S^0$, $\psi(2S)K_S^0$. With this method *BABAR* and Belle find:

$$\sin 2\beta = 0.687 \pm 0.028(\text{stat}) \pm 0.012(\text{syst}) \text{ (\textit{BABAR} [10])} \quad (1.39)$$

$$\sin 2\beta = 0.650 \pm 0.029(\text{stat}) \pm 0.018(\text{syst}) \text{ (Belle [11, 12])} \quad (1.40)$$

and the world average is:

$$\sin 2\beta = 0.673 \pm 0.023 \text{ [8]}. \quad (1.41)$$

One of the two solutions, $\beta \approx 21^\circ$, is in excellent agreement with the value predicted from the CKM fits to the Unitarity Triangle constraints. The solution with $\cos 2\beta < 0$ is excluded by *BABAR* at 86% CL from the study of the time- and angular-dependent distribution of neutral B decays to the mixed-CP $J/\psi K^{*0}$ ($K^{*0} \to K_S^0\pi^0$) final state [13].

1.3.2 $b \to c\bar{c}d$ and $b \to s\bar{s}s$ decays

The phenomenology of these rare decays is the same as for the $c\bar{c}s$ decays. A parameter $\sin 2\beta_{\text{eff}}$, where β_{eff} denotes an effective value of β, can be extracted from these penguin (loop) dominated decays. Measurable differences ΔS between the values of $\sin 2\beta$ in penguin-dominated modes and the $J/\psi K_S^0$ measurement can signal the presence of New Physics contributions in the loop. In some NP scenario, such deviations can be $\approx O(1)$ [14].

A background to ΔS measurements as a tool for NP searches are the doubly-Cabibbo suppressed tree contributions, which may also introduce nonzero ΔS. The Standard Model effect is predicted in most models to be a positive shift in ΔS [15].

The size of this shift is related to the ratio of tree to penguin amplitudes, which depends on the decay mode. Theoretical estimates for this ratio are affected by large uncertainties for most decay modes, with the notable exception of the $K_S K_S K^0$ and ϕK^0 modes (in which the tree amplitudes don't contribute at leading order), and $\eta' K^0$ (in which the gluon penguin amplitude is enhanced).

The $\eta' K^0$ channel provides the most precise measurement of S in a penguin dominated mode:

$$S_{\eta' K^0} = 0.57 \pm 0.08(\text{stat}) \pm 0.02(\text{syst}) \text{ (\textit{BABAR} [16])}, \quad (1.42)$$

$$S_{\eta' K^0} = 0.64 \pm 0.10(\text{stat}) \pm 0.04(\text{syst}) \text{ (Belle [11])}. \quad (1.43)$$

Although this is one of the theoretically cleanest modes, the observed discrepancy between $S_{J/\psi K_S^0}$ and $S_{\eta' K^0}$ is not significant.

1.4 Measurement of γ

The most popular methods for determining γ at the B-factories are based on the time-integrated analysis of the $B^- \to f_D K^{(*)-}$ decays, where the final state f_D is accessible either via intermediate $D^{(*)0}$ or $\overline{D}^{(*)0}$ mesons. This channel receives contributions from the color-suppressed $b \to u$ transition $B^- \to \overline{D}^{(*)0} K^{(*)-}$, as well as from the color-favored $b \to c$ transition $B^- \to D^{(*)0} K^{(*)-}$: γ can therefore be extracted by measuring the interference of these two paths, which occurs when $\overline{D}^0$ and D^0 both decay to f_D. The sensitivity to γ depends on the amount of interference, and henceforth on the relative magnitude r_B of the color-suppressed B-decay amplitude compared to the color-allowed one.

Several methods have been proposed, each one associated to a particular class of D-decay final states f_D, that use $B^\pm$ decays to pose constraints on the cartesian coordinates $x_\pm \equiv r_B \cos(\delta_B \pm \gamma)$ and $y_\pm \equiv r_B \cos(\delta_B \pm \gamma)$, where δ_B denotes the relative strong phase between the $b \to u$ and $b \to c$ transition.

The Gronau-London-Wyler (GLW) method [17] is based on the reconstruction of D^0 and $\overline{D}^0$ decays to CP-even (e.g., K^+K^-) and CP-odd (e.g., $K^0_S\pi^0$) eigenstates $f_{CP\pm}$, while the Atwood-Dunietz-Soni (ADS) method [18] relies on the reconstruction of D^0 decays to a doubly-Cabibbo-suppressed (DCS) final state f_{ADS} (e.g., $B^- \to D^0 K^-$ or $B^- \to D^{*0} K^-$ ($D^{*0} \to D^0\{\pi^0, \gamma\}$), with $D^0 \to K^+\pi^-$). Each GLW or ADS channel contributes two experimental observables, i.e., the branching ratio and the B^+/B^- asymmetry of the Cabibbo-suppressed decay:

$$R_{GLW} \equiv \frac{\mathcal{B}(B^- \to [f_{CP\pm}]_{D^0} K^-) + \mathcal{B}(B^+ \to [f_{CP\pm}]_{D^0} K^+)}{\mathcal{B}(B^- \to D^0 K^-) + \mathcal{B}(B^+ \to \overline{D}^0 K^+)} = 1 + r_B^2 \pm 2 r_B \cos\gamma \cos\delta_B,$$

$$A_{GLW} \equiv \frac{\mathcal{B}(B^- \to [f_{CP\pm}]_{D^0} K^-) - \mathcal{B}(B^+ \to [f_{CP\pm}]_{D^0} K^+)}{\mathcal{B}(B^- \to [f_{CP\pm}]_{D^0} K^-) + \mathcal{B}(B^+ \to [f_{CP\pm}]_{D^0} K^+)} = \pm 2 r_B \sin\gamma \sin\delta_B / R_{GLW},$$

$$R_{ADS} \equiv \frac{\mathcal{B}(B^- \to [f_{ADS}]_{D^0} K^-) + \mathcal{B}(B^+ \to [f_{ADS}]_{D^0} K^+)}{\mathcal{B}(B^- \to [\overline{f}_{ADS}]_{D^0} K^-) + \mathcal{B}(B^+ \to [\overline{f}_{ADS}]_{D^0} K^+)} = r_D^2 + r_B^2 + 2 r_D r_B \cos\gamma \cos(\delta_B + \delta_D),$$

$$A_{ADS} \equiv \frac{\mathcal{B}(B^- \to [f_{ADS}]_{D^0} K^-) - \mathcal{B}(B^+ \to [f_{ADS}]_{D^0} K^+)}{\mathcal{B}(B^- \to [\overline{f}_{ADS}]_{D^0} K^-) + \mathcal{B}(B^+ \to [\overline{f}_{ADS}]_{D^0} K^+)} = 2 r_D r_B \sin\gamma \sin(\delta_B + \delta_D) / R_{ADS},$$

where r_D and δ_D are the magnitude ratio and the strong phase difference of the doubly-Cabibbo-suppressed and the Cabibbo-allowed D^0 amplitudes in ADS channels, $\overline{f}_{ADS}$ (the CP conjugate of f_{ADS}) is the Cabibbo-allowed D^0 decay, and the notation $[f]_{D^0}$ indicates that the final state f is produced from the decay of a D^0 or $\overline{D}^0$. For each channel, the number of unknown (at least three, $\{\gamma, r_B, \delta_B\}$) exceeds the number of observables, so that the combination of several channels is necessary to constrain the system of unknowns.

The Giri-Grossmann-Soffer-Zupan (GGSZ) method [19] is based on the reconstruction of Cabibbo-favored D decays to three-body (or multi-body) self-conjugate final states, such as $K^0_S\pi^+\pi^-$. A Dalitz plot analysis of a three-body final state of the D meson allows one to obtain all the information required for the determination of γ in a single decay mode. The decay amplitudes of the admixed D^0 and $\overline{D}^0$ state produced in the $B^+ \to DK^+$ and $B^- \to DK^-$ processes as a function of Dalitz plot variables $m^2_+ = m^2_{K^0_S\pi^+}$ and $m^2_- = m^2_{K^0_S\pi^-}$

are

$$f_{B^+} = f_D(m_+^2, m_-^2) + r_B e^{i(\delta_B+\gamma)} f_D(m_-^2, m_+^2)\,, \quad (1.44)$$
$$f_{B^-} = f_D(m_-^2, m_+^2) + r_B e^{i(\delta_B-\gamma)} f_D(m_+^2, m_-^2)\,, \quad (1.45)$$

where $f_D(m_+^2, m_-^2)$ is the amplitude of the $D^0 \to K_S^0\pi^+\pi^-$ decay.

Both the ADS and GGSZ method rely on some previous knowledge of the D-decay parameters, that can be provided by the independent analysis of large D samples produced at the B-factories (introducing a model to describe the variation of the D-decay strong phase across the Dalitz plot) or by the input from the charm-factories.

From the combination of all the input from the B factories, γ is known to a precision of about 11°, up to a two-fold ambiguity. The two solutions are $\gamma = (-106 \pm 11)^\circ$ and $\gamma = (74 \pm 11)^\circ$ [20].

1.5 Measurement of α

The angle α can be measured from the study of charmless B decays dominated by the $b \to u\bar{u}d$ transition, such as B decays to $\pi\pi$, $\rho\pi$, $\rho\rho$, and $a_1(1260)\pi$. The interference between the direct tree decay (which carries the weak phase γ: Fig. 1.3, left) and decay after $B^0\overline{B}^0$ mixing (which carries an additional phase 2β) results in a time-dependent decay-rate asymmetry that is sensitive to the angle $2\beta + 2\gamma = 2\pi - 2\alpha$.

If only the tree amplitude contributes to the decay to a CP eigenstate, $S = \sin(2\alpha)$ and $C = 0$ (if the final state is not a CP eigenstate, an additional strong phase $\hat{\delta}$ between the two contributing tree amplitudes emerges). However, $b \to u\bar{u}d$ transitions receive sizeable contributions from penguin (loop) amplitudes (Fig. 1.3, right), which carry different strong and weak phases. This contribution can result in nonzero direct CP-violation ($C \neq 0$) and modifies S into

$$S = \sin(2\alpha_{\rm eff})\sqrt{1 - C^2}. \quad (1.46)$$

The angle $\alpha_{\rm eff}$ coincides with α in the limit of vanishing penguin contributions. In order to constrain $\Delta\alpha \equiv \alpha - \alpha_{\rm eff}$, several techniques have been devised, based on the SU(2) isospin symmetry (for decays to a CP-eigenstate, such as $B^0 \to \pi^+\pi^-, \rho^+\rho^-$, and in the Dalitz plot analysis of the three-body $\pi^+\pi^-\pi^0$ decays), or on the SU(3) approximate flavor symmetry (for decays to a non CP-eigenstate, such as $B^0 \to \rho^\pm\pi^\mp, a_1(1260)^\pm\pi^\mp$). In the following sections, we limit the discussion to *BABAR* measurements.

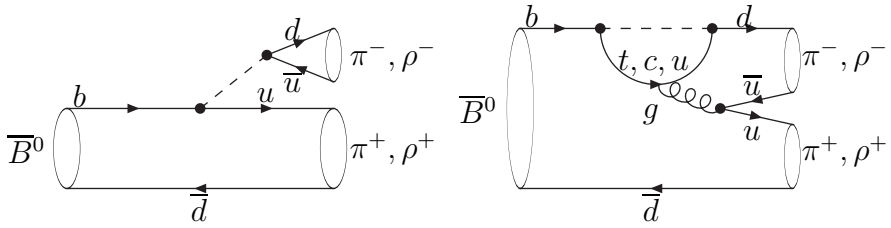

Figure 1.3: The tree (left) and penguin (right) diagrams contributing to "charmless" B decays such as $B \to \pi\pi$, $B \to \rho\rho$, and $B \to \rho\pi$.

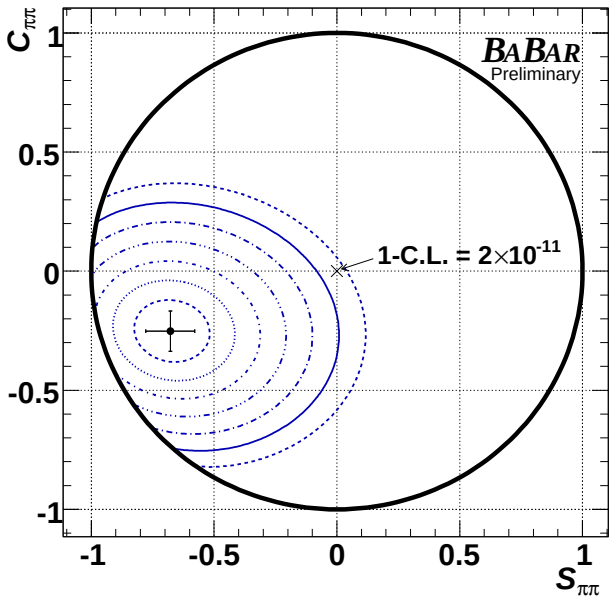

Figure 1.4: $S^{+-}_{\pi\pi}$ and $C^{+-}_{\pi\pi}$ in $B^0 \to \pi^+\pi^-$: the central values, errors, and confidence-level (C.L.) contours, calculated from the square root of the change in the value of $-2\ln\mathcal{L}$ compared with its value at the minimum [21]. The systematic errors are included. The measured value is 6.7σ from the point of no CP violation ($S^{+-}_{\pi\pi} = 0$ and $C^{+-}_{\pi\pi} = 0$).

1.5.1 Isospin analysis of $B \to \pi\pi$ decays

Originally it was believed that α could be extracted, in a straightforward way analogous to that used for β, from the time-dependent evolution of neutral B decays to the CP-even eigenstate $f = \pi^+\pi^-$. This analysis represents a prototype for α measurements. The amplitude of this process is

$$A(u\bar{u}d) = V_{tb}V^*_{td}P^t + V_{cb}V^*_{cd}P^c + V_{ub}V^*_{ud}(T + P^u), \tag{1.47}$$

which can be rewritten, expressing $V_{cb}V^*_{cd}$ in terms of $V_{tb}V^*_{td}$ and $V_{ub}V^*_{ud}$ as

$$A(u\bar{u}d) = V_{tb}V^*_{td}(P^t - P^c) + V_{ub}V^*_{ud}(T + P^u - P^c), \tag{1.48}$$

which has the form

$$A(u\bar{u}d) = Te^{i\gamma} + P. \tag{1.49}$$

In the $\pi\pi$ system, however, the penguin pollution is greatest, and the tree (T) and penguin (P) amplitudes each contribute, with relative weak (ϕ) and strong (δ) phases, with comparable magnitudes. Direct CP violation, which is given by $A_{CP} = 2\sin\phi\sin\delta/(|T/P| + |P/T| + 2\cos\phi\cos\delta)$, can therefore be within observational reach.

From the time distribution of $B^0 \to \pi^+\pi^-$ decays a non-zero CP violation asymmetry $S^{+-}_{\pi\pi} = -0.68 \pm 0.10 \pm 0.03$ was observed with significance 6.3σ [21], as shown in Fig. 1.4. A non-zero direct CP violation asymmetry $C^{+-}_{\pi\pi} = -0.25 \pm 0.08 \pm 0.02$ was also extracted with significance 3.0σ [21].

In principle, α could be also measured from the time-dependent analysis of $B^0 \to \pi^0\pi^0$ decays. However, at present-day B factories no reliable vertex information can be extracted for this channel, and $S^{00}_{\pi\pi}$ can not be determined. At future very high luminosity Super

Flavor factories, conversions into electron positron pairs of the photons originating from the π^0 decays could be used to determine the vertex of the $B^0 \to \pi^0\pi^0$ decay [22].

The rates and *CP* asymmetries of $B^0 \to \pi^+\pi^-$ and $B^0 \to \pi^0\pi^0$ decays can be combined with the results for the $B^+ \to \pi^+\pi^0$ mode in a model-independent isospin analysis [23]. Under the isospin symmetry, $B \to \pi\pi$ amplitudes can be decomposed in isospin $I = 0$ (A_0) and $I = 2$ (A_2) amplitudes. By virtue of Bose statistics, $I = 1$ contributions are forbidden, and the following relations hold [23]:

$$(1/\sqrt{2})A^{+-} = A_2 - A_0 \tag{1.50}$$

$$A^{00} = 2A_2 + A_0,\ A^{+0} = 3A_2, \tag{1.51}$$

where A^{ij} ($\overline{A}^{ij}$) are the amplitudes of B ($\overline{B}$) decays to the $\pi^i\pi^j$ final state. This yields the complex triangle relations:

$$\frac{1}{\sqrt{2}}A^{+-} = A^{+0} - A^{00} \tag{1.52}$$

$$\frac{1}{\sqrt{2}}\overline{A}^{+-} = \overline{A}^{-0} - \overline{A}^{00}. \tag{1.53}$$

Tree amplitudes receive contributions from both A_0 and A_2, while gluonic penguin diagrams are pure $I = 0$ amplitudes and do not contribute to the $B^+ \to \pi^+\pi^0$ amplitudes. Possible contributions from electroweak penguins (EWP), which do not obey SU(2) isospin symmetry, are assumed to be negligible and are therefore ignored. Under this assumption, $|A^{+0}| = |\overline{A}^{-0}|$ (a sizeable contribution from EWPs would result in $|A^{+0}| \neq |\overline{A}^{-0}|$ and would be signalled by an evidence of direct *CP* violation in $B^+ \to \pi^+\pi^0$ decays). If A^{+0} and $\overline{A}^{-0}$ are aligned with a suitable choice of phases, the relations (1.52) and (1.53) can be represented in the complex plane by two triangles (Fig. 1.5), and the phase difference between A^{+-} and $\overline{A}^{+-}$ is $2\Delta\alpha$.

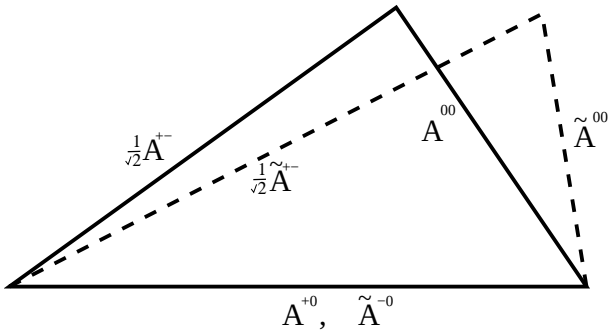

Figure 1.5: Triangles in the complex plane describing the isospin relations Eq. (1.52) and Eq. (1.53).

Constraints on the CKM angle α and on the penguin contribution $\Delta\alpha$ are obtained from a $1 - C.L.$ scan over the parameters of interest, α and $|\Delta\alpha|$. $\Delta\alpha$ is extracted with a four-fold ambiguity (which can be graphically represented as a flip of either triangle around A^{+0}). An additional two-fold ambiguity arises from the trigonometric relation $S^{+-}_{\pi\pi} = \sin(2\alpha_{\rm eff})\sqrt{1 - C^{+-2}_{\pi\pi}}$, which results in a global eight-fold ambiguity on α in the range $[0, 180]^\circ$.

The results are shown in Fig. 1.6. A value $\Delta\alpha < 43^\circ$ at 90% confidence level (C.L.) is obtained, which dominates the uncertainty on α [21]. Considering only the solution

consistent with the results of global CKM fits, α is in the range $[71, 109]^\circ$ at the 68% C.L. [21].

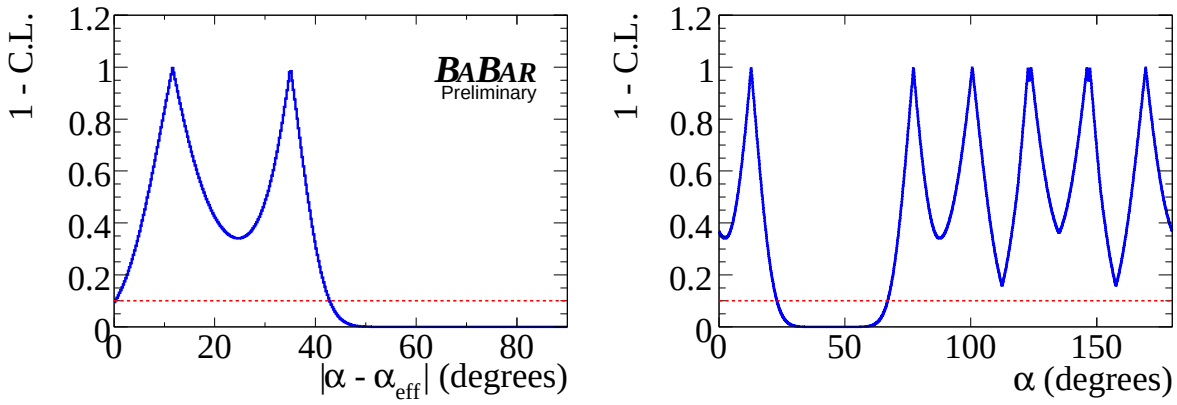

Figure 1.6: Left: Projection of the $1-C.L.$ scan on $\Delta\alpha$ for the $\pi\pi$ system. Right: Projection of the $1 - C.L.$ scan on α for the $\pi\pi$ system.

1.5.2 Isospin analysis of $B \to \rho\rho$ decays

With respect to $B \to \pi\pi$ decays, $B \to \rho\rho$ decays have a more favorable penguin to tree amplitude ratio. Moreover, the BF for $B^0 \to \rho^+\rho^-$ decays is greater than that for $B^0 \to \pi^+\pi^-$ decays by a factor of ≈ 5. Finally, the $B^0 \to \rho^0\rho^0$ decay (the analog of $B^0 \to \pi^0\pi^0$) can be reconstructed from a final state consisting of all charged tracks, with enough efficiency to allow for a measurement of $S^{00}_{\rho\rho}$ with the present statistics.

In $B^0 \to \rho^+\rho^-$ transitions, a pseudo-scalar particle decays into two vector mesons. Three helicity states ($H = 0, \pm 1$), with different CP transformation properties, can therefore contribute to the decay [24]. The $H = 0$ state corresponds to longitudinal polarization and is CP-even, while the transverse polarization states $H = +1$ and $H = -1$ (which are superpositions of S-, P-, and D-wave amplitudes) have not a definite CP eigenvalue.

The analysis of the angular distribution of $B^0 \to \rho^+\rho^-$ decays allows to determine the longitudinal polarization fraction f_L:

$$\frac{1}{\Gamma}\frac{d^2\Gamma}{d\cos\theta_1 d\cos\theta_2} \propto 4 f_L \cos^2\theta_1 \cos^2\theta_2 + (1 - f_L)\sin^2\theta_1 \sin^2\theta_2, \quad (1.54)$$

where θ_1 (θ_2) is the angle between the daughter π^0 and the direction opposite to the B direction in the ρ^+ (ρ^-) rest frame, as shown in Fig. 1.7. Isospin relations similar to Eq. (1.52) and (1.53) hold separately for each polarization state.

Since experimental measurements have shown the decay to be dominated by the longitudinal (CP-even) polarization, it is not necessary to separate the definite CP contributions of the transverse polarization by means of a full angular analysis.

A second complication arises because the ρ mesons have finite width, thus allowing for the two ρ mesons in the decay to have different masses. Since the Bose-Einstein symmetry does not hold, in this case, the wave function of the $\rho\rho$ system can be anti-symmetric, and isospin $I = 1$ amplitudes are allowed, breaking the isospin relations (1.52) and (1.53) [25]. The stability of the fitted CP-violation parameters against the restriction

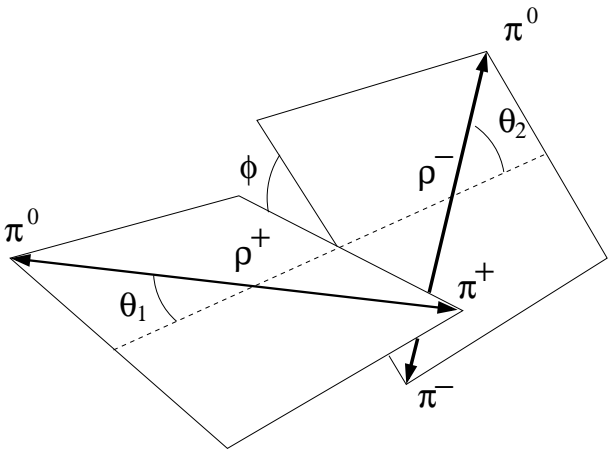

Figure 1.7: Definition of the θ_1 and θ_2 angles in $B \to \rho\rho$ decays.

of the $\pi\pi$ invariant mass window used to select the ρ candidates shows however that possible isospin violation effects are below the current sensitivity. Model-dependent uncertainties from flavor-symmetry breaking have been estimated to be of order $1^\circ - 2^\circ$.

The BF's of $B^+ \to \rho^+\rho^0$ and $B^0 \to \rho^+\rho^-$ measured by *BABAR* are very similar and much higher than that for the $B^0 \to \rho^0\rho^0$ penguin transition [26–28]. As a consequence, the isospin triangles do not close, i.e., $|A^{+-}|/\sqrt{2} + |A^{00}| < |A^{+0}|$. This results in a degeneracy of the eight-fold ambiguity on α into a four-fold ambiguity, corresponding to peaks in the vicinity of 0°, 90° (two degenerate peaks), 180°, as shown in Fig. 1.8. A value $-1.8^\circ < \Delta\alpha < 6.7^\circ$ at 68% C.L. is obtained. Considering only the solution consistent with the results of global CKM fits, $\alpha = 92.4^{+6.0}_{-6.5}$ [28, 29].

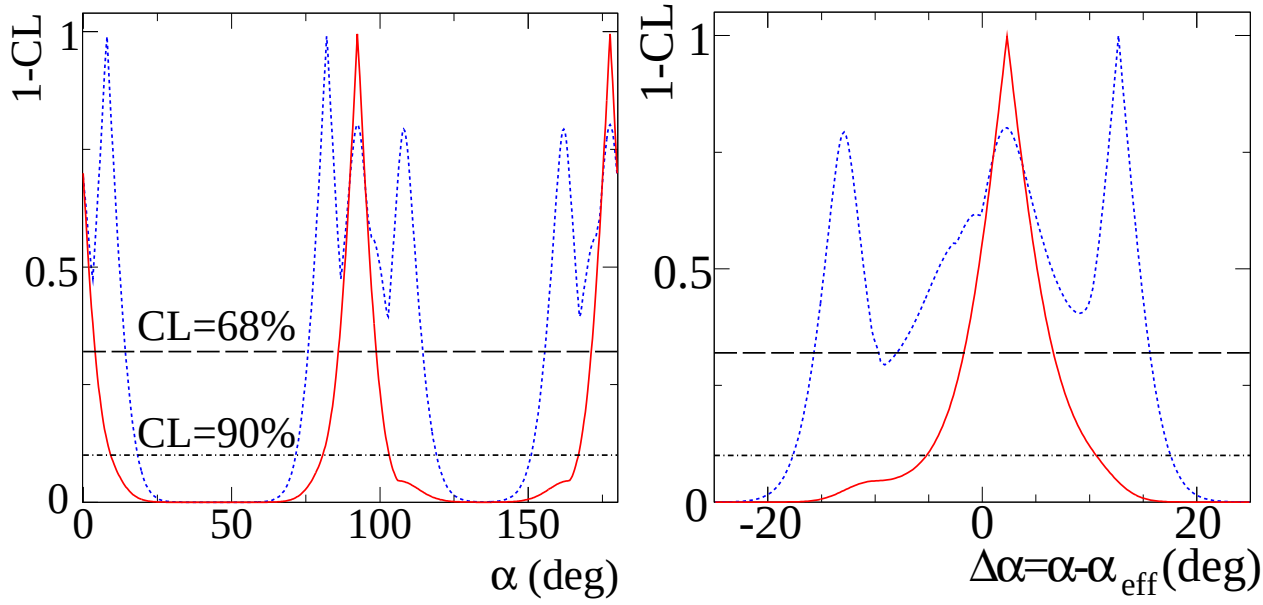

Figure 1.8: Left: Projection of the $1-C.L.$ scan on $\Delta\alpha$ for the $\rho\rho$ system. Right: Projection of the $1 - C.L.$ scan on α for the $\rho\rho$ system.

1.5.3 Time dependent Dalitz plot analysis of $B^0 \to \pi^+\pi^-\pi^0$ decays

The $\rho^\pm\pi^\mp$ final state is not a *CP* eigenstate. For the $\rho\pi$ channel, therefore, two time-dependent distributions can be analyzed, for the $\rho^+\pi^-$ and the $\rho^-\pi^+$ final states, respectively. An isospin analysis for these final states would require solving a set of higher-order algebraic equations, and hence the solution would be severely obscured by a very high number of discrete ambiguities. An analysis based on the approximate SU(3) symmetry [30], similar to the one discussed in the next section, could instead be performed.

As $B \to \rho\pi$ decays result in a three-body final state, an alternative path consists in performing a time-dependent Dalitz plot analysis of the $B \to \pi^+\pi^-\pi^0$ decays [31]. This method exploits the interference between the intermediate ρ resonances to extract a value of α without ambiguities in the range $[0, 180]^\circ$ and without relying on measurements of any auxiliary channels.

The amplitude $A_{3\pi}$ of the $B^0 \to \pi^+\pi^-\pi^0$ transition receives contributions from $B^0 \to \rho^+\pi^-$, $B^0 \to \rho^-\pi^+$, and $B^0 \to \rho^0\pi^0$, and can be written as

$$A_{3\pi}(s_+, s_-) \;=\; f_+(s_+, s_-)\, A_+ + f_-(s_+, s_-)\, A_- + f_0(s_+, s_-)\, A_0, \tag{1.55}$$

where the subscript "+" represents $\rho^+\pi^-$, "−" is for $\rho^-\pi^+$, and "0" is for $\rho^0\pi^0$; $s_+ = (p_+ + p_0)^2$, $s_- = (p_- + p_0)^2$, and p_+, p_-, and p_0 are the four-momenta of the π^+, π^-, and π^0, respectively. The kinematic functions f_i and $\overline{f}_i$ are the products of Breit-Wigner functions to describe the $\pi\pi$ lineshape and an angular function to describe the helicity distribution.

The Dalitz plot has a time distribution

$$\begin{aligned} |A(t, s_+, s_-)|^2 \;\propto\; e^{-\Gamma|t|}\Bigg\{ & (|A_{3\pi}|^2 + |\overline{A}_{3\pi}|^2) \;- \\ & q_{\rm tag}(|A_{3\pi}|^2 - |\overline{A}_{3\pi}|^2)\cos(\Delta m\,\Delta t) \;+ \\ & q_{\rm tag}\, 2\,{\rm Im}\left(\frac{q}{p} A^*_{3\pi}\overline{A}_{3\pi}\right)\sin(\Delta m\,\Delta t)\Bigg\}, \end{aligned} \tag{1.56}$$

where $q_{\rm tag}$ equals $+1\,(-1)$ when the tag-side B decays as a $B^0(\overline{B}^0)$. From a fit to the time-dependence of the Dalitz plot it is possible to determine the six complex amplitudes A_i and $\overline{A}_i$ (12 real parameters), and α is then obtained via the relationship

$$e^{i2\alpha} \;=\; \frac{\overline{A}_+ + \overline{A}_- + 2\overline{A}_0}{A_+ + A_- + 2A_0}. \tag{1.57}$$

From such an analysis, *BABAR* finds at the 68% C.L. $\alpha = (87^{+45}_{-13})^\circ$ [32].

1.6 Weak phase α from $B^0 \to a_1^\pm(1260)\pi^\mp$

It is possible to use the experimental information from the TD CPV analysis of $B^0 \to a_1^\pm\pi^\mp$ decays [33], and from the branching fraction measurements of $B^0 \to a_1^\pm\pi^\mp$ [34], $B^0 \to a_1^- K^+$, $B^+ \to a_1^+ K^0$ [35], and $B^0 \to K_1^+\pi^-$, $B^+ \to K_1^0\pi^+$ decays (measured in this work), to extract the CKM angle α.

In order to exploit the experimental information to constrain this angle we follow the Gronau and Zupan paper [36] to identify a convenient parameterization of the amplitudes

$$A_+ \equiv A(B^0 \to a_1^+\pi^-), \qquad A_- \equiv A(B^0 \to a_1^-\pi^+), \tag{1.58}$$
$$\overline{A}_+ \equiv A(\overline{B}^0 \to a_1^-\pi^+), \qquad \overline{A}_- \equiv A(\overline{B}^0 \to a_1^+\pi^-). \tag{1.59}$$

These amplitudes can be expressed in terms of "tree" ($t_\pm$) and "penguin" ($p_\pm$) amplitudes, with different strong phases (implicit in the definition of p and t) and relative weak phase γ:

$$A_\pm = \; e^{i\gamma}t_\pm + p_\pm, \quad \overline{A}_\pm = e^{-i\gamma}t_\pm + p_\pm. \tag{1.60}$$

We can express the time-dependence of $B^0 \to a_1^\pm\pi^\mp$ decay rates as

$$F_{Q_{\rm tag}}^{a_1^\pm\pi^\mp}(\Delta t) \quad \propto \quad (1 \pm \mathcal{A}_{CP})\frac{e^{-|\Delta t|/\tau}}{8\tau}\Bigg\{1 + Q_{\rm tag} \times \Big[(S \pm \Delta S)\sin(\Delta m_d \Delta t) - (C \pm \Delta C)\cos(\Delta m_d \Delta t)\Big]\Bigg\},$$

where $Q_{\rm tag} = +1(-1)$ if the tag-side B decays as a B^0 ($\overline{B}^0$), $\tau = 1.525 \pm 0.009$ ps [5] is the mean B lifetime, $\Delta m_d = 0.507 \pm 0.005$ ps^{-1} [5] is the B^0-$\overline{B}^0$ mixing frequency, and $\mathcal{A}_{CP}$ is the time- and flavor-integrated CP asymmetry

$$\mathcal{A}_{CP} \equiv \frac{|A_+|^2 + |\overline{A}_-|^2 - |A_-|^2 - |\overline{A}_+|^2}{|A_+|^2 + |\overline{A}_-|^2 + |A_-|^2 + |\overline{A}_+|^2}.$$

The parameters C and ΔC parameterize the flavor-dependent direct CP violation and the asymmetry between the CP-averaged rates $\bar{\mathcal{B}}(a_1^+\pi^-)$ and $\bar{\mathcal{B}}(a_1^-\pi^+)$, respectively [36]:

$$C + \Delta C = \frac{|A_+|^2 - |\overline{A}_-|^2}{|A_+|^2 + |\overline{A}_-|^2}, \qquad C - \Delta C = \frac{|A_-|^2 - |\overline{A}_+|^2}{|A_-|^2| + \overline{A}_+|^2},$$

while S and ΔS

$$S + \Delta S = \frac{2\,{\rm Im}(e^{-2i\beta}\overline{A}_- A_+^*)}{|A_+|^2 + |\overline{A}_-|^2}, \qquad S - \Delta S = \frac{2\,{\rm Im}(e^{-2i\beta}\overline{A}_+ A_-^*)}{|A_-|^2 + |\overline{A}_+|^2}.$$

The quantities

$$2\alpha_{\rm eff}^\pm \pm \hat{\delta} = \arg\left(e^{-2i\beta}\overline{A}_\pm A_\mp^*\right), \tag{1.61}$$

with

$$2\alpha_{\rm eff}^\pm \equiv \arg\left(e^{-2i\beta}\overline{A}_\pm A_\pm^*\right),$$
$$\hat{\delta} \equiv A_-^* A_+,$$

are then experimentally accessible from the inversion of (1.61):

$$2\alpha_{\rm eff}^\pm \pm \hat{\delta} = \arg\left(e^{-2i\beta}\overline{A}_\pm A_\mp^*\right) = \arcsin\left(\frac{S \pm \Delta S}{\sqrt{1 - (C \pm \Delta C)^2}}\right). \tag{1.62}$$

Table 1.1: Summary of the eight solutions to (1.63), in absence of penguin contributions.

α	$\pi/4-\hat{\delta}/2$	$\pi/2+\alpha$	$3\pi/4-\hat{\delta}/2$	$\pi/4+\hat{\delta}/2$	$\pi/2-\alpha$	$3\pi/4+\hat{\delta}/2$	$\pi-\alpha$
$\hat{\delta}$	$\pi/2-2\alpha$	$\pi+\hat{\delta}$	$3\pi/2-2\alpha$	$-\pi/2+2\alpha$	$-\hat{\delta}$	$-3\pi/2+2\alpha$	$\pi-\hat{\delta}$

The quantities $\alpha_{\rm eff}^{\pm}$ reduce to α in case of negligible penguin contributions:

$$\begin{aligned} e^{-2i\beta}\overline{A}_{\pm}A_{\pm}^{*} &= e^{-2i\beta}e^{-2i\gamma}\left[|t_{\pm}|^2\left(1+2r_{\pm}e^{i\gamma}\cos\delta_{\pm}+r_{\pm}^2e^{2i\gamma}\right)\right] \\ &= e^{2i\alpha}\left[|t_{\pm}|^2\left(1+2r_{\pm}e^{i\gamma}\cos\delta_{\pm}+r_{\pm}^2e^{2i\gamma}\right)\right]. \end{aligned}$$

The above expression can be rewritten as

$$\begin{aligned} e^{-2i\beta}\overline{A}_{\pm}A_{\pm}^{*} &= e^{-2i\beta}e^{-2i\gamma}\left[e^{2i\Delta\alpha^{\pm}}\left|\overline{A}_{\pm}A_{\pm}^{*}\right|\right] \\ &= e^{2i\alpha}\left[e^{2i\Delta\alpha^{\pm}}\left|\overline{A}_{\pm}A_{\pm}^{*}\right|\right] \\ &= e^{2i(\alpha+\Delta\alpha^{\pm})}\left(\left|\overline{A}_{\pm}\right|^2+\left|A_{\pm}^{*}\right|^2\right)\frac{1}{2}\sqrt{1-(\mathcal{A}_{CP}^{\pm})^2}, \end{aligned}$$

where $2\Delta\alpha^{\pm}=2(\alpha_{\rm eff}^{\pm}-\alpha)=\arg\left(1+2r_{\pm}e^{i\gamma}\cos\delta_{\pm}+r_{\pm}^2e^{2i\gamma}\right)$.

The strong phase $\hat{\delta}$ can be averaged out from (1.62), yielding an effective value of α

$$\alpha_{\rm eff}=\frac{1}{2}\left[\arcsin\left(\frac{S+\Delta S}{\sqrt{1-(C+\Delta C)^2}}\right)+\arcsin\left(\frac{S-\Delta S}{\sqrt{1-(C-\Delta C)^2}}\right)\right], \qquad (1.63)$$

which is determined up to an eightfold ambiguity in the range $[0,180]^{\circ}$. The set of ambiguities on $\alpha_{\rm eff}$, in absence of penguin contributions, is summarized in Table 1.1.

We now introduce the *CP* asymmetries $\mathcal{A}_{CP}^{\pm}$ in $B^0\to a_1^{\pm}\pi^{\mp}$ decays, that are related to the time- and flavor-integrated charge asymmetry $\mathcal{A}_{CP}^{a_1\pi}$ [33] by

$$\mathcal{A}_{CP}^{+}=-\frac{\mathcal{A}_{CP}^{a_1\pi}(1+\Delta C)+C}{1+\mathcal{A}_{CP}^{a_1\pi}C+\Delta C}, \quad \mathcal{A}_{CP}^{-}=\frac{\mathcal{A}_{CP}^{a_1\pi}(1-\Delta C)-C}{1-\mathcal{A}_{CP}^{a_1\pi}C-\Delta C}.$$

We are thus lead to:

$$\begin{aligned} \left|e^{-i\gamma}A_{\pm}-e^{i\gamma}\overline{A}_{\pm}\right|^2 &= 4p_{\pm}^2\sin^2\gamma \\ &= |A_{\pm}|+\left|\overline{A}_{\pm}\right|-2\,{\rm Re}\left(e^{2i\gamma}A_{\pm}^{*}\overline{A}_{\pm}\right) \\ &= \left(\left|\overline{A}_{\pm}\right|^2+\left|A_{\pm}^{*}\right|^2\right)\left[1-\sqrt{1-(\mathcal{A}_{CP}^{\pm})^2}\cos2\Delta\alpha^{\pm}\right]. \end{aligned} \qquad (1.64)$$

It is possible to relate the $B^0\to a_1^{\pm}\pi^{\mp}$ decays with the corresponding $\Delta S=1$ decays, $B\to a_1K$ and $B\to K_{1A}\pi$, where K_{1A} is a nearly equal mixture of the $K_1(1270)$ and $K_1(1400)$ resonances and belongs to the same SU(3) flavor multiplet as the a_1 meson (see Chapter 3). The $\Delta S=1$ transitions are particularly sensitive to the presence of penguin amplitudes because the ratios of penguin-to-tree amplitudes are enhanced by a CKM factor $(\overline{\lambda})^{-2}$ ($\overline{\lambda}=0.23$) over the corresponding ratios in $\Delta S=0$ decays. Similar SU(3)-based approaches have been proposed for the extraction of α in the $\pi^+\pi^-$ [37], $\rho^{\pm}\pi^{\mp}$ [30], and $\rho^+\rho^-$ channels [38, 39].

For the strangeness changing decay amplitudes, we write:

$$A(B^+ \to a_1^+ K^0) = -(\overline{\lambda})^{-1}\frac{f_K}{f_\pi}p_-, \qquad A(B^0 \to a_1^- K+) = \frac{f_K}{f_\pi}[-(\overline{\lambda})^{-1}p_- + e^{i\gamma}\overline{\lambda}t_-],$$
$$A(B^+ \to K_{1A}^0\pi^+) = -(\overline{\lambda})^{-1}\frac{f_{K_{1A}}}{f_{a_1}}p_+, \qquad A(B^0 \to K_{1A}^+\pi^-) = \frac{f_{K_{1A}}}{f_{a_1}}[-(\overline{\lambda})^{-1}p_+ + e^{i\gamma}\overline{\lambda}t_+],$$

where $\overline{\lambda} = |V_{us}|/|V_{ud}| = |V_{cd}|/|V_{cs}|$, and f_π, f_K, f_{a_1}, $f_{K_{1A}}$ are decay constants. To improve the precision of the analysis, factorizable SU(3) breaking factors are included in the above expression, and are given by the ratios of meson decay constants under the assumption that form factors do not differ much from one another. We have neglected nonfactorizable SU(3) breaking corrections and contributions from exchange and annihilation diagrams (contributing to $\Delta S = 0$ and $\Delta S = 1$ decays, respectively), which are formally $1/m_b$ suppressed relative to tree and penguin amplitudes [36].

We now define the following ratios of CP-averaged rates [36]:

$$R_+^0 \equiv \frac{\bar{\lambda}^2 f_{a_1}^2 \bar{\mathcal{B}}(K_{1A}^+\pi^-)}{f_{K_{1A}}^2 \bar{\mathcal{B}}(a_1^+\pi^-)}, \quad R_-^0 \equiv \frac{\bar{\lambda}^2 f_\pi^2 \bar{\mathcal{B}}(a_1^- K^+)}{f_K^2 \bar{\mathcal{B}}(a_1^-\pi^+)},$$
$$R_+^+ \equiv \frac{\bar{\lambda}^2 f_{a_1}^2 \bar{\mathcal{B}}(K_{1A}^0\pi^+)}{f_{K_{1A}}^2 \bar{\mathcal{B}}(a_1^+\pi^-)}, \quad R_-^+ \equiv \frac{\bar{\lambda}^2 f_\pi^2 \bar{\mathcal{B}}(a_1^+ K^0)}{f_K^2 \bar{\mathcal{B}}(a_1^-\pi^+)},$$

where $\bar{\mathcal{B}}(f) \equiv \frac{1}{2}\mathcal{B}(B \to f) + \mathcal{B}(\overline{B} \to \overline{f})$. The CP-averaged rates for $B \to a_1\pi$ are calculated as

$$\bar{\mathcal{B}}(a_1^+\pi^-) = \frac{1}{2}\mathcal{B}(a_1^\pm\pi^\mp)(1 + \Delta C + \mathcal{A}_{CP}^{a_1\pi} C),$$
$$\bar{\mathcal{B}}(a_1^-\pi^+) = \frac{1}{2}\mathcal{B}(a_1^\pm\pi^\mp)(1 - \Delta C - \mathcal{A}_{CP}^{a_1\pi} C),$$

where $\mathcal{B}(a_1^\pm\pi^\mp)$ is the flavor-averaged branching fraction of neutral B decays to $a_1(1260)^\pm\pi^\mp$ [34]. In terms of the above parameterization, we can write:

$$R_\pm^0 = \frac{r_\pm^2 + 2r_\pm z_\pm \overline{\lambda}^2 + \overline{\lambda}^4}{1 + r_\pm^2 - 2r_\pm z_\pm}, \quad R_\pm^+ = \frac{r_\pm^2}{1 + r_\pm^2 - 2r_\pm z_\pm}, \tag{1.65}$$

where $z_\pm = \cos\delta_\pm \cos(\alpha + \beta)$, $r_t \equiv |t_-/t_+|$, $\delta_t \equiv \arg(t_-/t_+)$, $r_\pm \equiv |p_\pm/t_\pm|$, and $\delta_\pm \equiv \arg(p_\pm/t_\pm)$. The above equations are solved to write $r_\pm$ in terms of $z_\pm$ and $R_\pm^0$ or $R_\pm^+$ [30]:

$$r_\pm = \frac{\sqrt{(R_\pm^0 + \overline{\lambda}_\pm^2)^2 z_\pm^2 + (1 - R_\pm^0)(R_\pm^0 - \overline{\lambda}_\pm^4)} - (R_\pm^0 + \overline{\lambda}_\pm^2) z_\pm}{1 - R_\pm^0} \tag{1.66}$$

$$= \frac{\sqrt{{R_\pm^+}^2 z_\pm^2 + (1 - R_\pm^+)R_\pm^+} - R_\pm^+ z_\pm}{1 - R_\pm^+}, \tag{1.67}$$

where only the positive solutions have been taken. These expressions are monotonically decreasing functions of $z_\pm$, so that the penguin-over-tree ratios $r_\pm$ are bracketed by their values at $z_\pm = \pm 1$:

$$\frac{\sqrt{R_\pm^0} - \overline{\lambda}_\pm^2}{1 + \sqrt{R_\pm^0}} < \frac{|p_\pm|}{|t_\pm|} < \frac{\sqrt{R_\pm^0} + \overline{\lambda}_\pm^2}{1 - \sqrt{R_\pm^0}}, \tag{1.68}$$

$$\frac{\sqrt{R_\pm^+}}{1 + \sqrt{R_\pm^+}} < \frac{|p_\pm|}{|t_\pm|} < \frac{\sqrt{R_\pm^+}}{1 - \sqrt{R_\pm^+}}. \tag{1.69}$$

Substituting $R_\pm^+$ in Eq. 1.64 it is possible to derive the following inequalities involving $\Delta\alpha^\pm$:

$$\cos 2\Delta\alpha^\pm = \frac{1 - 2R_\pm^+ \sin^2\gamma}{\sqrt{1-(\mathcal{A}_{CP}^\pm)^2}} \geq \frac{1-2R_\pm^+}{\sqrt{1-(\mathcal{A}_{CP}^\pm)^2}}. \tag{1.70}$$

Similar inequalities involving $R_\pm^0$ are derived by noting that

$$\frac{\bar{\lambda}^2 f_{a_1}^2 \bar{\mathcal{B}}(K_{1A}^+\pi^-)}{f_{K_{1A}}^2 |p_\pm|^2} = 1 + 2r_\pm^{-1}\overline{\lambda}^2 z_\pm + r_\pm^{-2}\overline{\lambda}^4 \tag{1.71}$$

and $[1 - \cos^2\delta_\pm \cos^2\gamma + (\cos^2\delta_\pm \cos^2\gamma - 2x\cos\delta_\pm\cos\gamma + x^2)] \geq \sin^2\gamma$, where $x = r_\pm^{-1}\overline{\lambda}^2$, so that

$$\cos 2\Delta\alpha^\pm \geq \frac{1-2R_\pm^0}{\sqrt{1-(\mathcal{A}_{CP}^\pm)^2}}. \tag{1.72}$$

In Chapter 6, solving this system of inequalities allows to calculate bounds on $|\Delta\alpha| = \frac{1}{2}(\Delta\alpha^+ + \Delta\alpha^-)$.

Chapter 2

The *BABAR* experiment

2.1 Overview

Exploring *CP* violation in the B system and its potential impact on the Standard Model, baryogenesis, and cosmology, requires copious production of B mesons, accurate measurement of the B flight time and flavor, and reasonably low background for reconstruction.

The asymmetric e^+e^- B-factories operated at a center-of-momentum (CM) energy $\sqrt{s} = 10.58$ GeV fulfill these requirements. This energy corresponds to the mass of the $\Upsilon(4S)$ resonance, a $b\overline{b}$ bound state lying just above the open flavor threshold, that decays almost exclusively to approximately equal numbers of $B^0\overline{B}^0$ and B^+B^- pairs [5]. The $\Upsilon(4S)$ resonance thus provides a very clean environment for B reconstruction, with a very favorable ratio of $b\overline{b}$ production compared to lighter quark pairs production (Table 2.1). A typical $\Upsilon(4S) \to B\overline{B}$ event has on average ten charged particles and twenty photons, as compared with the hundreds of charged particles in events recorded at hadronic colliders, which can also be used to study b-hadron decays.

$e^+e^- \to$	Cross section (nb)
$b\overline{b}$	1.05
$c\overline{c}$	1.30
$s\overline{s}$	0.35
$u\overline{u}$	1.39
$d\overline{d}$	0.35
$\tau^+\tau^-$	0.94
$\mu^+\mu^-$	1.16
e^+e^-	≈ 40

Table 2.1: Approximate production cross sections at PEP-II ($\sqrt{s} = 10.58$ GeV). Bhabha cross section is an effective cross section for production within the detector acceptance.

As it is produced in e^+e^- annihilation through a virtual photon, angular momentum conservations ensures the $\Upsilon(4S)$ resonance carries the same spin and parity as the photon, i.e., it is a vector. Since B mesons are pseudoscalars, the $B\overline{B}$ pair from the $\Upsilon(4S)$ decay evolves in a coherent P-wave and the two mesons have opposite flavor before one of them decays, in accordance with Bose statistics. Thus, it is possible to infer the flavor of a

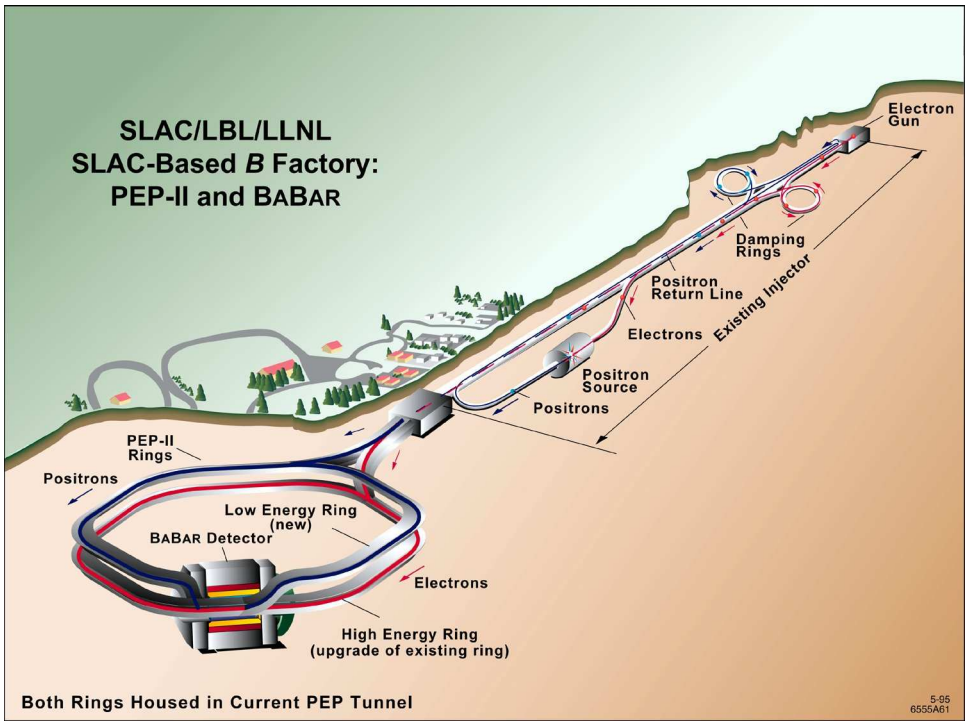

Figure 2.1: The PEP-II asymmetric storage ring and the SLAC linear accelerator. The SLAC linac is the injector for PEP-II. The single interaction point of PEP-II is at Interaction Region 2, where *BABAR* is situated.

reconstructed B candidate ($B_{\rm rec}$) from the flavor of the other B in the $\Upsilon(4S)$ event ($B_{\rm tag}$) at the time of its decay. This can be done through charge correlations of the $B_{\rm tag}$ daughters without fully reconstructing its decay. Such flavor "tagging" of the other B in turn allows the measurement of time-dependent CP asymmetries in reconstructed final states to which both B^0 and $\overline{B}^0$ can decay. The decay rate of $B_{\rm rec}$ is measured as a function of the difference in decay times of the two B's, $\Delta t \equiv t_{B_{\rm rec}} - t_{B_{\rm tag}}$.

Since the lifetime of the B mesons is of order $\tau = 1.5$ ps, if the two B mesons were produced in the laboratory frame the two decay vertices would be separated by only about 30 μm, a distance that couldn't be resolved by typical silicon-vertex detectors, which have a spatial vertex resolution of about 50 μm. To bring the average decay-vertex separation within the resolution reach of silicon-detector technology, the B factories adopted an asymmetric configuration in which the electron and positron beams collide with different energies. The resulting $B\overline{B}$ system is thus boosted in the laboratory frame and the distance between the decay vertices in the laboratory frame is dilated along the beam direction.

2.2 The PEP-II asymmetric collider

Two asymmetric B-factories have been built: PEP-II/*BABAR* (part of the accelerator complex at SLAC, shown in Fig. 2.1) and KEK-B/Belle. The PEP-II B-factory [40] consists of two storage rings built one above the other in the previously existing PEP (Positron-Electron Project) tunnel. The construction project reutilized much of SLAC's existing PEP facility: the lower ring (high energy ring, HER), which stores electrons, was an upgrade

of the PEP collider; the upper ring (low energy ring, LER), used for positrons, was newly constructed.

The rings are matched to the 3.2-kilometer-long SLAC linear accelerator, which acts as a particle injector. The positrons are generated partway along the linear accelerator by directing high-energy electrons onto a cooled rotating tungsten target. Both the electrons and positrons are stored in damping rings, where the spatial and momentum spread of the beams are reduced, before they are reinjected into the linac and accelerated to the collision energies. The electron and positron beams are then extracted from the linac and directed to the PEP-II storage rings, where they are made to collide.

PEP-II was primarily designed to operate at a CM energy of 10.58 GeV to study time-dependent *CP* violation asymmetries in the B meson system. Most of the data is taken at this CM energy; however, approximately 10% of the data are taken 40 MeV below the resonance peak energy (off-resonance data), in order to allow studies of non-resonant background in data. In addition, *BABAR* also collected world-record samples at the $\Upsilon(2S)$ and $\Upsilon(3S)$ CM energies: at the end of its operations, the physics program of PEP-II/*BABAR* encompassed the study of rare B meson decays, τ and charm physics, charmonium and bottomonium spectroscopy, and two-photon physics.

A plot of PEP-II integrated luminosity as a function of time is shown in Fig. 2.2. PEP-II has delivered 557 fb^{-1} [41], while KEK-B integrated luminosity has exceeded 1 ab^{-1} [42]. The work in this thesis is based on the *BABAR* dataset collected at the $\Upsilon(4S)$ resonance, corresponding to an integrated luminosity of 413 fb^{-1} and $N_{B\overline{B}} = (454.3 \pm 5.0) \times 10^6$ produced $B\overline{B}$ pairs.

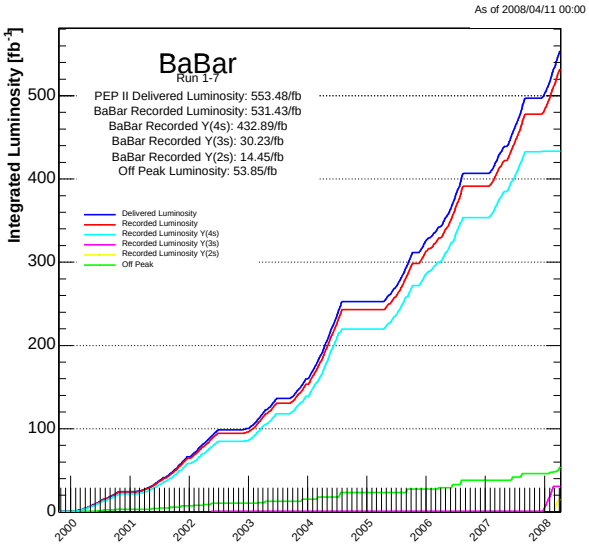

Figure 2.2: PEP-II-*BABAR* integrated luminosity since startup.

2.3 The *BABAR* detector

When PEP-II is operated at 10.58 GeV, 9.0 GeV electrons and 3.1 GeV positrons collide head-on in the single interaction point of PEP-II, where *BABAR* is located. This configu-

ration provides a relativistic boost of $\beta\gamma = 0.56$ to the CM system, corresponding to an average separation $\beta\gamma c\tau \approx 250\,\mu$m between the decay vertices of the two B mesons in a $\Upsilon(4S)$ event.

The *BABAR* detector is a large, multi-purpose hermetic detector with several components [43]. Surrounding the interaction point is a five-layer double-sided silicon vertex tracker that provides precision measurements near the collision point of charged particle tracks in the planes transverse to and along the beam direction. A 40-layer drift chamber surrounds the SVT. Both of these tracking devices operate in the 1.5 T magnetic field of a superconducting solenoid to provide measurements of the momenta of charged particles. Charged hadron identification is achieved through measurements of particle energy loss in the tracking system and of the Cerenkov angle obtained from a detector of internally reflected Cerenkov light (DIRC). A CsI(Tl) electromagnetic calorimeter (EMC) provides photon detection and electron identification. Finally, the instrumented flux return (IFR) of the magnet allows discrimination of muons from pions and detection of K_L^0 mesons.

The structure of the *BABAR* detector is shown in Fig. 2.3 and Fig. 2.4. The detector has a cylindrical geometry in the inner zone and a hexagonal shape in the outermost; the central body is called "barrel" and is enclosed by two "endcaps". In the *BABAR* coordinate system, the z-axis is directed along the axis of the solenoid magnet, the y-axis is vertical, and the x-axis is horizontal and points toward the external part of the PEP-II ring. To maximize the geometric acceptance for the boosted $\Upsilon(4S)$ decays, the geometrical center is offset from the beam-beam interaction point towards forward polar angles, i.e. in the direction of the boost.

2.3.1 The silicon vertex tracker (SVT)

Together, the silicon vertex tracker (SVT) and the central tracking drift chamber (DCH) form the charged particle tracking system. Precise and efficient measurement of track four-momentum is necessary to fully reconstruct B meson decays, which tend to have multiple charged decay products. In addition, good vertex and Δz resolution and accurate track extrapolation to the outer subdetectors are essential for event reconstruction and background subtraction.

The SVT is the most relevant detector for the measurement of time dependent *CP* asymmetries in *BABAR*. Its purpose is to provide precise reconstruction of charged particle trajectories and decay vertices near the interaction region. Many of the decay products of the B mesons have low transverse momentum p_T. The SVT must provide stand-alone tracking for particles with transverse momentum less than 120 MeV/c, the minimum that can be measured reliably in the DCH alone. Beyond the stand-alone tracking capability, the SVT provides the best measurement of track angles, which is required to achieve the design resolution for the Cerenkov angle for high momentum tracks.

The design of the SVT is illustrated in Fig. 2.5 and consists of five layers of double-sided silicon strip sensors, organized in 6, 6, 6, 16, and 18 modules. The geometrical acceptance of SVT is about 90% of the solid angle in the CM system. The modules of the inner three layers are straight, while the modules of layers 4 and 5 are arch-shaped (Fig. 2.6) to minimize the amount of silicon required to cover the solid angle, and increase the crossing angle for particles near the edges of acceptance.

The five layers and the long radial separation between SVT detector layers provide both standalone track pattern recognition and refinement of drift chamber tracks via addition

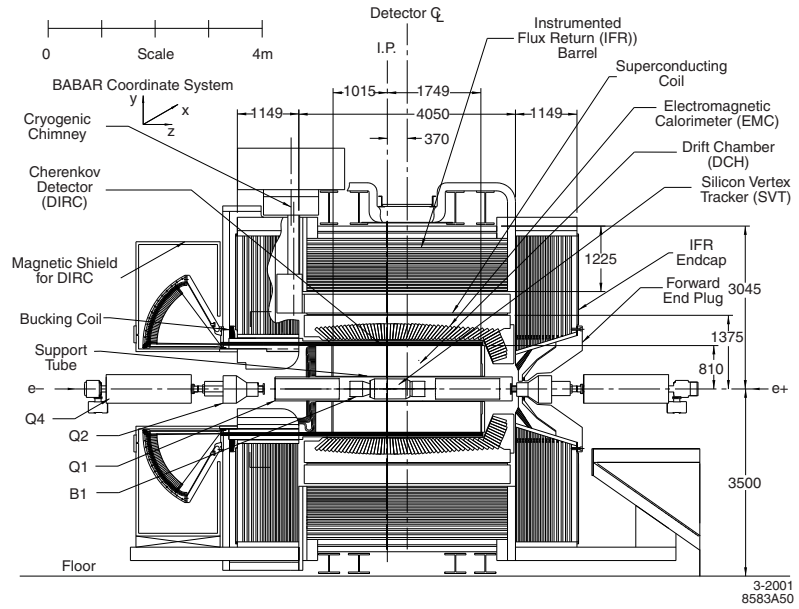

Figure 2.3: Longitudinal view of the *BABAR* detector.

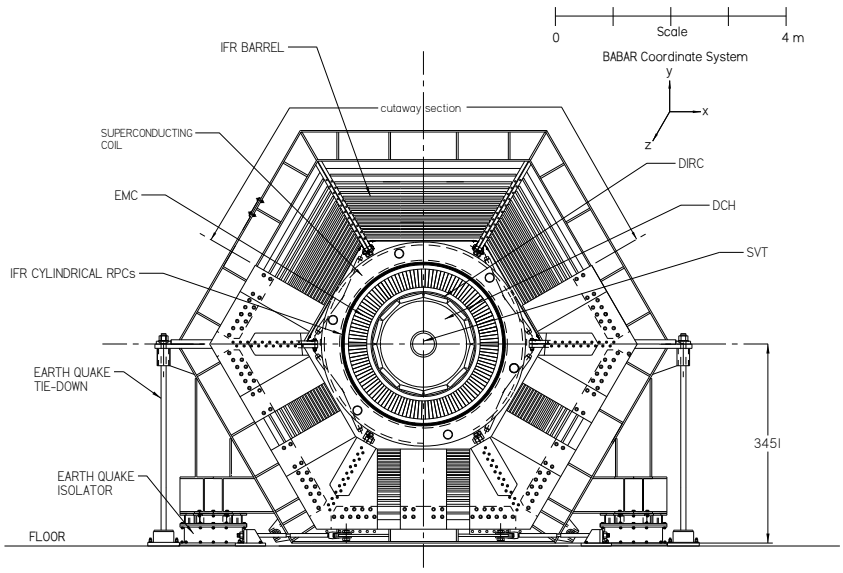

Figure 2.4: End view of the *BABAR* detector.

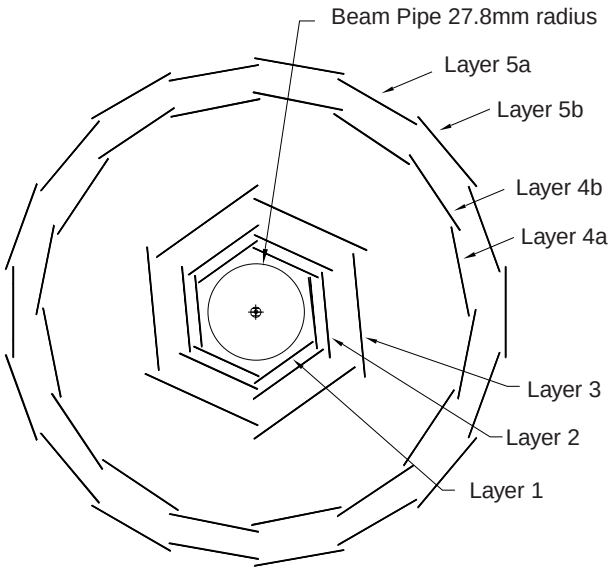

Figure 2.5: Transverse view of the SVT.

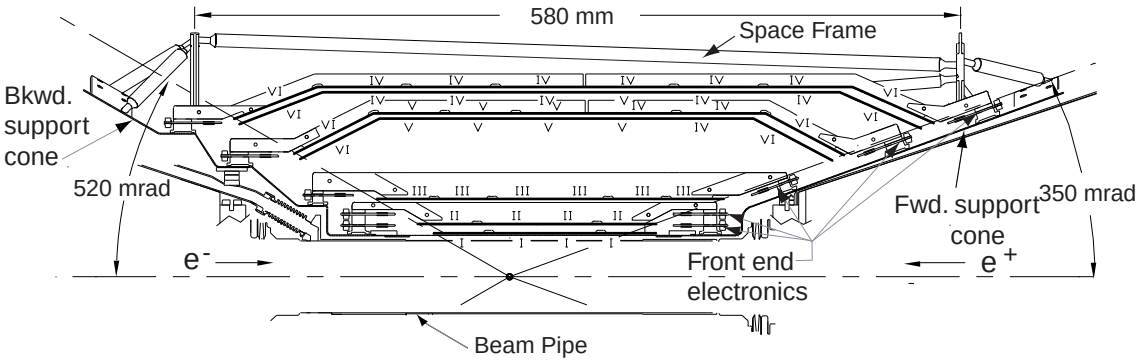

Figure 2.6: Longitudinal section of the SVT.

of SVT hits. The inner three layers perform the impact parameter measurement and are located as close to the beampipe as possible, since the trajectory of the particles farther away is affected by multiple scattering within the detector. The outer layers are necessary for pattern recognition and low p_T tracking, and are closer to the drift chamber to facilitate matching of SVT tracks with DCH tracks. To fulfill the physics requirements, the spatial resolution for perpendicular tracks must be 10–15 μm in the three inner layers and about 40 μm in the two outer layers.

The silicon sensors are 300 μm-thick high sensitivity n-type substrates, with p^+ and n^+ strips running orthogonally on opposite sides: the ϕ measuring strips run parallel to the beam, while the z measuring strips are oriented transversely to the beam axis. As high-energy particles pass through the sensor they ionize the material, producing electron-hole pairs, that migrate under an applied depletion voltage of $\sim 25 - 35$ V. The strips are AC-coupled to the electronic read-out (only approximately half the strips are read out). The signal is then amplified and discriminated with respect to a signal threshold by front-end electronics. The time over threshold of the signal is related to the charge of the signal and is read out by the data acquisition system for triggered events. The resulting information on the ionization energy loss dE/dx provides a 2σ separation between kaons and pions up to 500 MeV/c and between kaons and protons above 1 GeV/c.

The offline reconstruction has the responsibility for the alignment of each SVT module. Alignment is critical for the accuracy of vertexing and of track reconstruction, and is done in two steps. The local SVT alignment uses dimuon and cosmic ray events to calibrate the relative position of each of the 340 wafers. The global alignment then determines the overall position and rotation of the SVT with respect to the DCH.

Being the innermost detector, the SVT has been designed to withstand a high dose of integrated ionizing radiation, up to a lifetime-integrated dose of 2 Mrad. To limit the exposure, the SVT includes a radiation protection system consisting of PIN diodes (doped p-type and n-type semiconductor regions separated by an intrinsic semiconducting region) and diamond diode sensors located in close proximity to the beam. These monitors can abort the colliding beams in the event of sudden high instantaneous or prolonged background levels that could damage the hardware components.

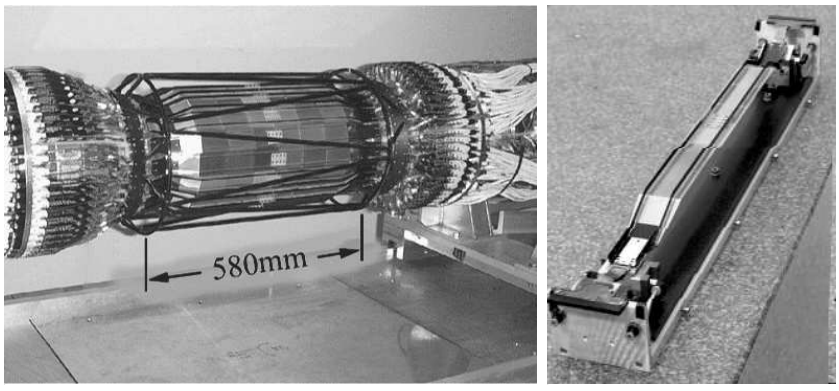

Figure 2.7: Left: fully assembled SVT. The silicon sensors of the outer layer are visible, as is the carbon-fiber space frame (black structure) that surrounds the silicon. Right: an SVT arch module.

2.3.2 The drift chamber (DCH)

For $p_t \geq 100$ MeV/c, *BABAR* measurement of charged particles momenta is dominated by the DCH, a multi-wire proportional chamber. The DCH provides particle identification information based on the measurement of the ionization energy loss (dE/dx) for low momentum particles (< 700 MeV/c), and those in the extreme forward and backward directions that fall outside the geometric acceptance of the DIRC. The DCH also serves in reconstructing longer-lived particles (such as K_S^0's) that decay away from the interaction region outside of the SVT.

The DCH measures the trajectory of charged particles by the ionization of an 80:20 helium:isobutane gas mixture as the particle passes through the detector. The ionized electrons from the gas drift towards gold-coated tungsten-rhenium sense wires held at high voltage ($\sim$ 1900V); as they are accelerated, they ionize other molecules of gas producing a shower of negative charge deposited on the sense wire. The positively ionized gas molecules produced in the shower are attracted by gold-coated aluminium grounded field wires, arranged in a hexagonal pattern, that surround the sense wire.

The position of the primary ionization clusters is derived from timing of the leading edge of the amplified signal from the sense wire, while the total charge induced on the wire is a measure of the ionization energy loss, dE/dx. Samples of cosmic muons and dilepton events are used to calculate isochrones (distances of equal drift time) from which the drift time to distance relation is determined. A typical dE/dx resolution of 7.5% is estimated from a sample of Bhabha events.

The final design adopted for the DCH is illustrated in Fig. 2.8. The hexagonal drift cells are arranged in 40 cylindrical layers; the layers are grouped into 10 superlayers. Two of the four layers in each superlayer are directed along the z-axis, while the other two are set at small stereo angles relative to the two axial layers, thus providing a measurement of the longitudinal (z) position of tracks with good ($\sim$ 1 mm) resolution. The DCH has a typical position resolution of 140 μm.

The achieved resolution on transverse momentum is

$$\sigma_{p_t}/p_t = (0.13 \pm 0.01)\% \cdot p_t + (0.45 \pm 0.03)\%, \tag{2.1}$$

where p_t is given in units of GeV/c. The first contribution comes from the curvature error due to finite spatial measurement resolution; the second contribution, dominating at the low momenta that characterize B decays, is due to multiple Coulomb scattering. The choice of low-mass aluminum field-wires and of a helium-based gas mixture is aimed at minimizing the material within the chamber volume, to reduce the impact of multiple scattering on p_t resolution.

2.3.3 The DIRC

The detector of internally reflected Cerenkov light (DIRC) is designed to provide a good $\pi - K$ separation over the momentum range 700 MeV/c – 4.2 GeV/c, while minimizing the amount of material in front of the EMC.

The DIRC principle uses internal reflection within quartz bars, which serve as radiators as well as light guides, to propagate Cerenkov light to readout phototubes while preserving the Cerenkov angle. This requires extremely flat surfaces in order to avoid dispersing the reflected angles. The Cerenkov angle contains information on particle type via the relation

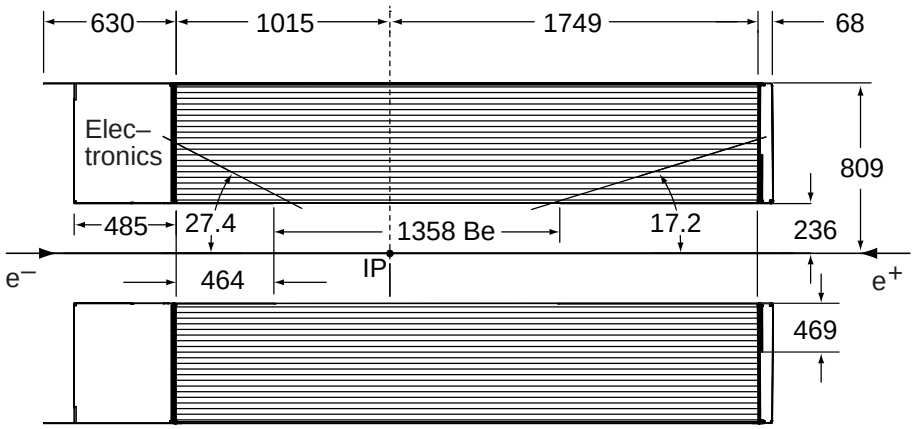

Figure 2.8: Longitudinal section of the drift chamber.

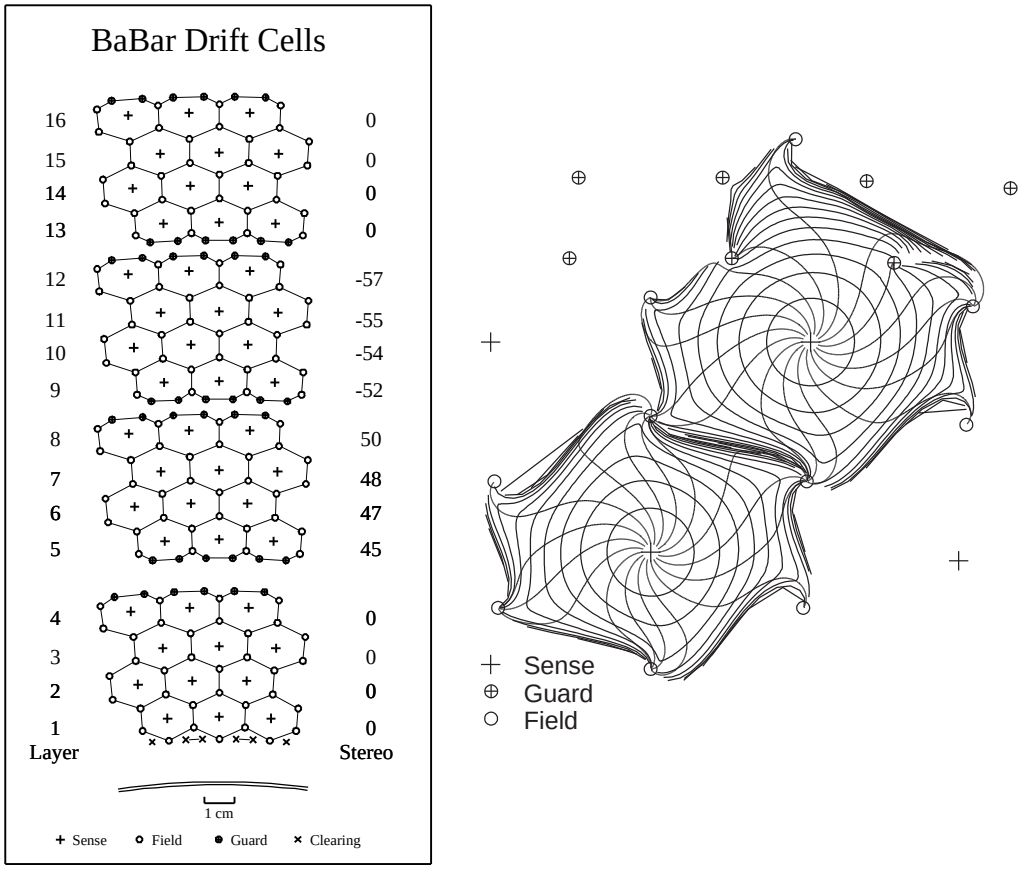

Figure 2.9: Left: schematic layout of the drift cells for the four innermost superlayers. The numbers on the right side give the stereo angles in mrad of sense wires in each layer. Right: DCH cell drift isochrones for cells in layers 3 and 4 (axial). Isochrones are at 100 ns intervals.

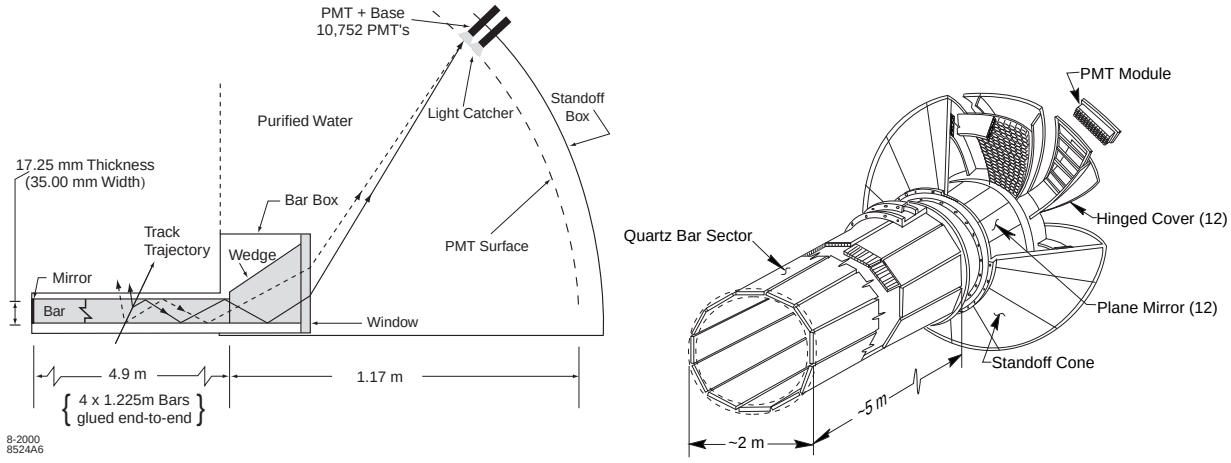

Figure 2.10: Schematics of the DIRC fused silica radiator bar and imaging region.

$\cos\theta_C = 1/n\beta$, with β being the particle velocity normalized to the speed of light, and n being the mean index of refraction (= 1.473 for fused silica). Fused, synthetic silica quartz is used due to the excellent optical surface it allows through polishing, as well as other favorable properties such as long attenuation length, low chromatic dispersion, small radiation length, and radiation hardness. At the backward end of the bars, the photons pass through a standoff box filled with purified water that has a similar refractive index of $n = 1.346$, so that refraction at the silica-water boundary is minimized. A mirror is placed at the end opposite the standoff box to collect light internally reflected toward the opposite end of the detector. The rear surface of the standoff box is instrumented with photomultiplier tubes (PMTs), which collect the photons, convert them to electrons with photocathodes, and amplify the signal using the gas-avalanche principle. As the standoff box is located outside the solenoid magnet, it is possible to limit the magnetic field in its volume to about 1 Gauss with a bucking coil that counteracts the field of the solenoid, so that conventional PMTs, which do not tolerate high magnetic fields, can be used.

The emission angle and the arrival time of the Cerenkov photons are reconstructed from the observed space-time coordinates of the PMT signals and then transformed into the Cerenkov coordinates (θ_C, ϕ_C and δ_t) via a maximum likelihood fit. The time interval between the t_0 of the event and the time at which an hit in the PMTs occurs is measured with a resolution of 1.5 ns. Timing gives information on the photon propagation angles, providing an independent measurement of the Cerenkov angle, and is critical for background hit rejection, resolving ambiguities, and separation of hits from differing tracks within an event.

Based on the position and timing of the PMT signals from the DIRC, coupled with the particle position and angle from the tracking system, the Cerenkov angle can be overconstrained and measured with a resolution of ~ 3 mrad. At 3 GeV/c, this results in $\pi - K$ separation of $4.2\,\sigma$.

2.3.4 The electromagnetic calorimeter (EMC)

The EMC is designed to operate within the 1.5-T magnetic field and detect electromagnetic showers from photons and electrons, with excellent energy and angular resolution over

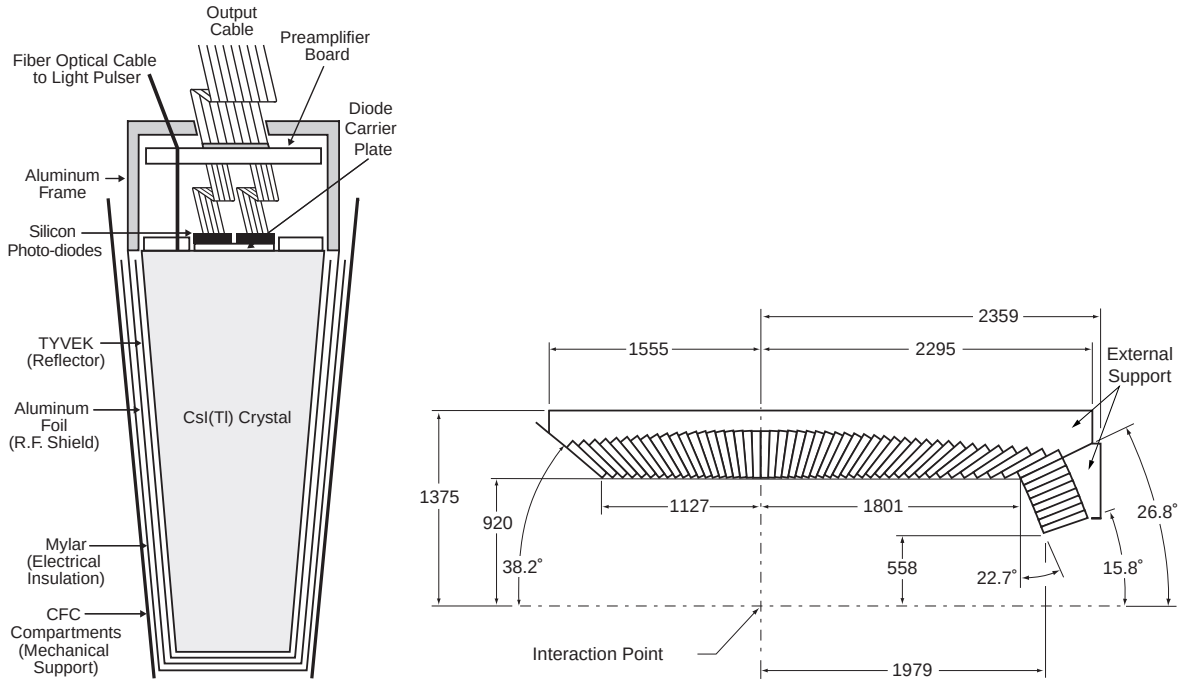

Figure 2.11: Longitudinal cross section of the EMC (left). Schematic of a wrapped CsI(Tl) crystal and read out package (right). Dimensions are in mm.

the energy range from 20 MeV to 9 GeV. This functionality is necessary to reconstruct π^0 and η two-photon decays, as well as for identification of high-energy photons from radiative B decays.

BABAR uses a thallium-doped cesium iodide (CsI(Tl)) crystal calorimeter in order to achieve the necessary energy and angular resolution to meet these physics requirements. The EMC consists of a cylindrical barrel and a conical forward endcap, for a total of 6580 crystals, that cover $\sim 90\%$ of the CM acceptance. A diagram can be seen in Fig. 2.11.

The crystals have nearly square front and rear faces with a trapezoidal longitudinal cross-section. They act not only as a total-absorption scintillating medium, but also as a light guide to collect light at the silicon PIN photodiodes that are mounted on the rear surface.

The energy response of the EMC is calibrated using low-energy photons from a radioactive source and high-energy photons from radiative Bhabha events. As electromagnetic showers spread throughout several crystals, a reconstruction algorithm is used to associate activated crystals into clusters and either to identify them as photon candidates or to match individual maxima of deposited energy to extrapolated tracks from the DCH-SVT tracker. Additional PID is obtained from the spatial shape of the shower.

Energy resolution is determined, e.g., using $\chi_c \to J/\psi\gamma$ and Bhabha scattering events, to be

$$\frac{\sigma_E}{E} = \frac{(2.32 \pm 0.30)\%}{\sqrt[4]{E(\,\mathrm{GeV})}} \oplus (1.85 \pm 0.12)\%, \tag{2.2}$$

while angular resolution is determined by analyzing π^0 and η decays to two photons of

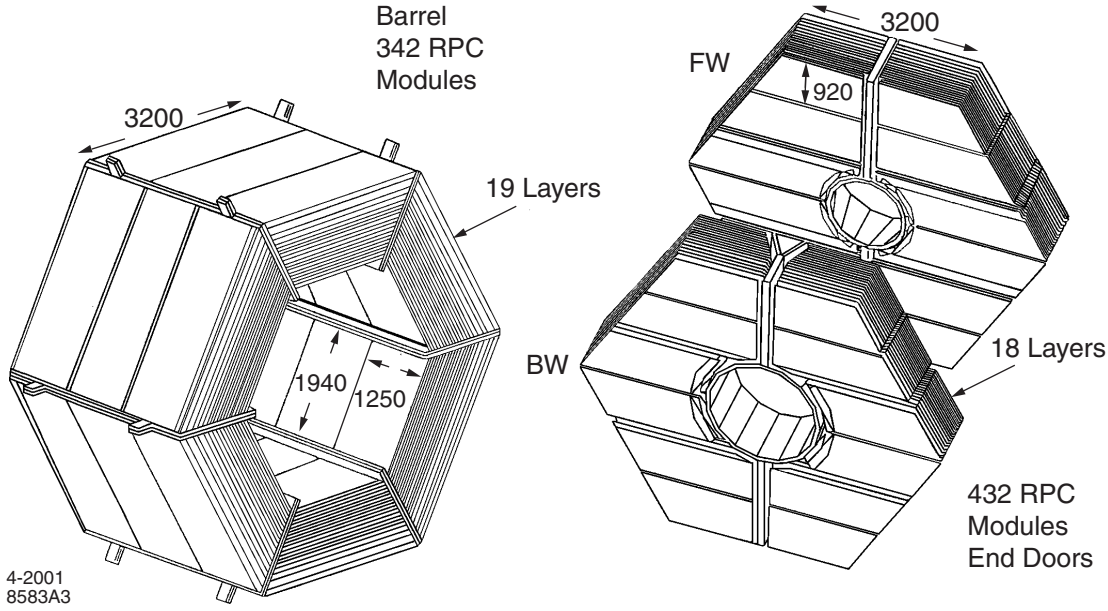

Figure 2.12: Overview of the barrel sectors and forward and backward end doors of the IFR. The shape of the RPC modules and their dimensions in mm are indicated.

equal energy to be

$$\sigma_\theta = \sigma_\phi = \frac{(3.87 \pm 0.07)\ \text{mrad}}{\sqrt{E(\,\text{GeV})}} \oplus (0.00 \pm 0.04)\ \text{mrad}. \tag{2.3}$$

In both cases, the first term is due to fluctuations in the number of photons and to electronic noise of the photon detector and electronics, while the second term arises from the non-uniformity of light collection, leakage and absorption due to materials between and in front of the crystals, and calibration uncertainties.

2.3.5 The instrumented flux return (IFR)

Detection of muons and neutral hadrons (primarily K_L^0's) is a necessary step for several *BABAR* measurements: muons are important, e.g., for the J/ψ reconstruction and for tagging the flavor of the non-signal B through semileptonic decays of the B or daughter D mesons in the event; K_L^0 detection allows the study of exclusive B decays to CP eigenstates.

The main requirements for the IFR are: a large solid angle coverage, good efficiency and high background rejection power for muons with momentum down to 1 GeV/c.

The IFR uses the steel flux return of the magnet as a muon filter and hadron absorber. Its layout is illustrated in Fig. 2.12. It consists of an hexagonal barrel region closed in the forward and backward directions by two endcaps that can be opened to access the inner part of the *BABAR* detector. Both the endcaps and the barrel region are layered and active detectors are inserted between the iron plates.

The IFR was originally equipped with 19 layers of resistive plate chambers (RPCs) in the barrel and 18 in the endcaps. In addition, two layers of cylindrical RPCs were installed between the EMC and the cryostat of the magnet to improve the matching between IFR and EMC showers. Resistive plate chambers consist of two highly-resistive bakelite planes

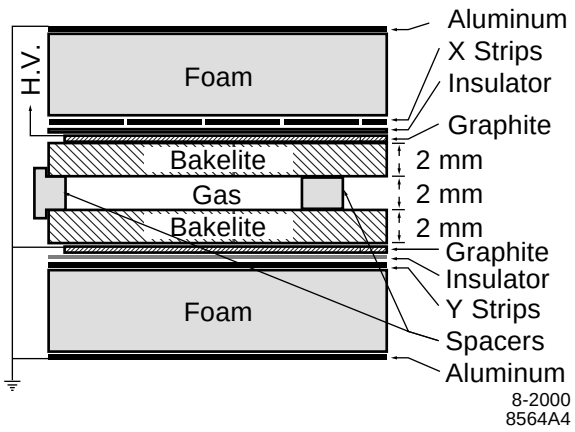

Figure 2.13: Cross section of a *BABAR* RPC.

closely separated by a gap filled with a gas mixture, held at a large potential voltage. The inside surface of the bakelite is smoothed with a linseed-oil coating so that the electric field is uniform, thus preventing discharges in the gas and large dark currents. The RPCs operate in "streamer" mode, wherein particles passing through the chamber ionize the gas, and the applied high voltage accelerates the resulting electrons into a controlled gas-discharge avalanche. The streamer signal is collected by inducing a charge in capacitatively-coupled read-out strips outside of the RPC. The gas gain in streamer mode is sufficient to produce a large signal independent of initial ionization, greatly simplifying the electronics read-out. A cross-sectional diagram of a planar RPC is shown in Fig. 2.13.

During the first year of operation, a large fraction of the RPC modules suffered significant losses in efficiency. It was found that linseed oil droplets had formed on the inner surface of the bakelite plates, probably because of high operating temperatures ($> 37°$ C). These accumulating droplets, under the high electric field, could "bridge the gap" between the plates, leading to discharge and large detector dead areas.

In 2002, new RPCs constructed under much stricter tolerances were installed into the forward endcap. The backward endcap was not retrofitted, as its acceptance in the CM frame is small. In the barrel, the RPCs were replaced with limited streamer tubes (LST) during two installation phases, in 2004 (top and bottom sextants) and 2006 (the other sextants). The outermost layer of RPCs (layer 19) was inaccessible in the upgrade, and was disconnected. To improve hadron absorption within the active region of the IFR, 6 layers of brass were installed every second layer starting with layer 5. The remaining twelve layers were filled with LSTs.

The LSTs consist of a PVC comb of seven or eight gas-filled cells with grounded graphite-coated walls and a central gold-plated beryllium-copper anode wire held at high voltage (Fig. 2.14 and Fig. 2.15). Similar to RPCs, the gas operates in streamer mode when ionized, with the charge collected on the high voltage sense wire while simultaneously inducing a charge on a plane, which is mounted below the tube. The LSTs are mounted with the wire directed along the beam (so as to provide information about the azimuthal angle of the hit), while the induced charge on the plane is detected using copper strips perpendicular to the wire direction and conveys the z coordinate.

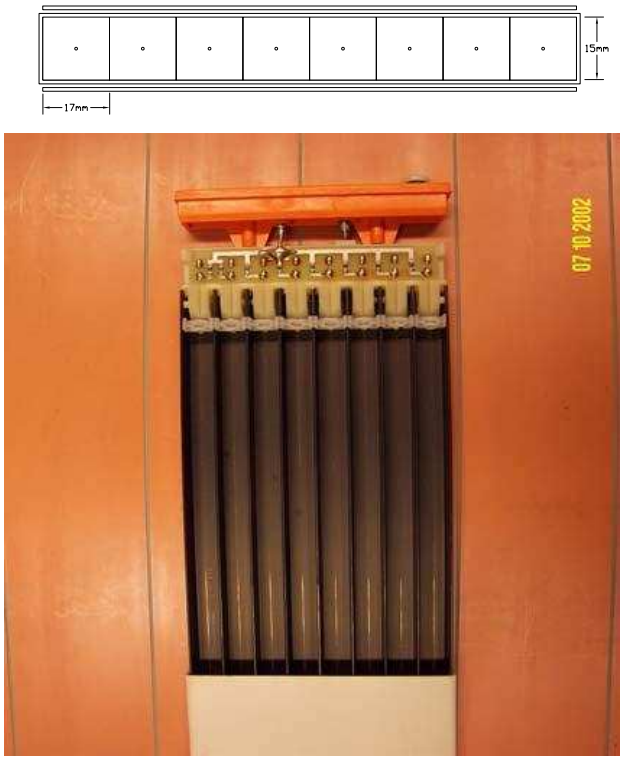

Figure 2.14: Sketch of an 8-cell module (top), and photo of an LST partially inserted in the sleeves (shown at the bottom of the picture).

2.3.6 The trigger

The *BABAR* trigger needs to provide a high efficiency, stable, and well-understood response for physics events. Since the events which pass the trigger must be fully reconstructed in the offline event reconstruction, the output rate must be no higher than 120 Hz to satisfy computing limitations of the offline processing farm. Since events with either a DCH track or a > 100 MeV EMC cluster occur at 20 kHz, the trigger is responsible for scaling this rate down by a factor of > 150 while accepting over 99% of B events, over 95% of hadronic continuum, and over 90% of $\tau^+\tau^-$ events. Online dead time is kept lower than 1%.

The *BABAR* trigger is implemented in two levels, a Level 1 hardware trigger (called L1), and a Level 3 software trigger (called L3). The L1 trigger consists of several dedicated microprocessor systems that analyze data from the front-end electronics of the DCH, EMC, and IFR to form primitive physics objects used to make the trigger decision. These include tracks of minimum transverse momentum that penetrate to a particular depth into the DCH and energy clusters in the EMC above set thresholds.

After an L1 accept decision, the L1 output is passed on to the L3 trigger, which consists of software-based algorithms run on a farm of commercial PCs. The L3 trigger also has access to the complete event data and refines the L1 decision with more sophisticated selections, such as requirements on a tracks distance of closest approach to the interaction point or the total invariant mass of an event.

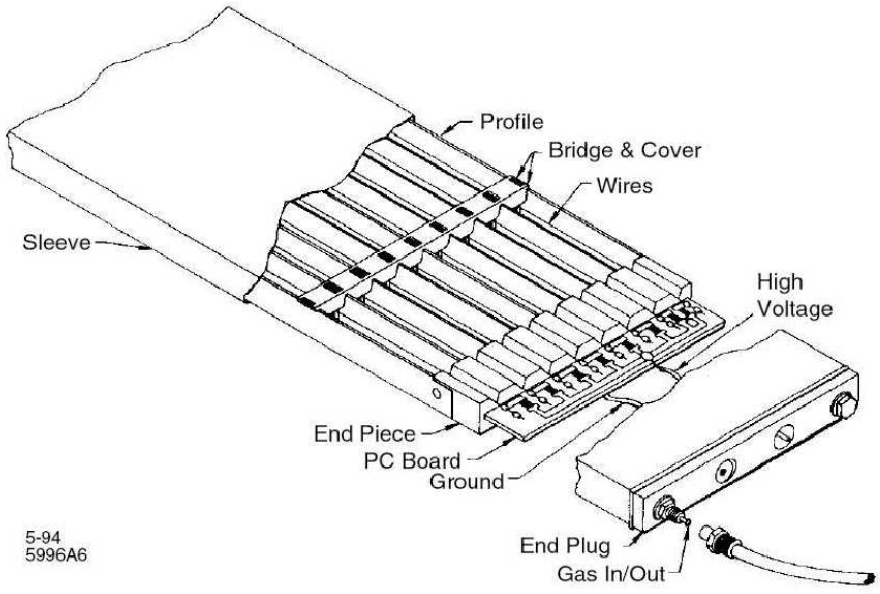

Figure 2.15: Diagram of a prototypical limited streamer tube.

Chapter 3

The strange axial vector mesons $K_1(1270)$ and $K_1(1400)$

3.1 Introduction

Introduced in 1966, SU(3) and the non-relativistic quark model have ever since allowed to correlate huge amounts of experimental data on elementary particles and their interactions. One of their main successes has been the classification of particles in spin-parity multiplets sharing similar properties.

Two nonets ($\mathbf{8} \oplus \mathbf{1}$) of spin-parity $J^P = 1^+$ mesons containing the light u, d, s quarks are expected, each identified by the $C-$parity of its $I = 1$, $I_3 = 0$ member, the $a_1(1260)^0$ ($C = +1$) and the $b_1(1235)^0$ ($C = -1$). The mesons belonging to these multiplets are the $a_1(1260)$, $f_1(1420)$, $f_1(1285)$, K_{1A}, and the $b_1(1235)$, $h_1(1380)$, $h_1(1170)$, K_{1B} [5].

The K_1 mesons (formerly also known as Q mesons), although observed in several reactions, have been most thoroughly studied in diffractive production processes $K^{\pm} \to K^{\pm}\pi^+\pi^- p$ [44, 45] and three-prong τ decays [46–49]. The partial wave analysis of the diffractive data shows a resonant contribution of a system $K\rho$ in the 1^+ waves with invariant mass ~ 1270 MeV/c^2, and a two-peak structure in the 1^+ $K^*\pi$ system, at ~ 1240 MeV and ~ 1400 MeV/c^2. In non-diffractive reactions (such as the baryon exchange reaction $K^- p \to \Sigma^-(K\pi\pi)^+$ [50], the hypercharge exchange reaction $\pi^- p \to (K\pi\pi)\Lambda$ [51], and $p\bar{p}$ annihilation [52, 53]) one often observes only one resonance. The most conclusive and high-statistics sample of $K_1(1270)$ and $K_1(1400)$ mesons was collected by the ACCMOR Collaboration with the WA3 experiment [45]. The WA3 fixed target experiment accumulated data from the reaction $K^- p \to K^-\pi^+\pi^- p$ with an incident kaon energy of 63 GeV. The partial wave analysis of the reaction final state is described in Sec. 3.4.

In the currently accepted description [5], the two peaks are associated with two partially overlapping resonances, the $K_1(1270)$ and the $K_1(1400)$, both decaying to the $K\pi\pi$ final state. Models including a higher number of resonances have also been proposed [54]. The masses, widths and decay modes of the K_1 mesons are briefly summarized in Table 3.1. The $K_1(1270)$ decays predominantly through the $K\rho$ intermediate state, while the decays of the $K_1(1400)$ proceed almost exclusively via the $K^*\pi$ channel. The experimental properties of the K_1 mesons suggest that the $K_1(1270)$ and the $K_1(1400)$ mesons are nearly equal admixtures of the strange members of the $C = +1$ and $C = -1$ octets [55–57], where the mixing is parameterized by a mixing angle θ_K; this is further discussed in Sec. 3.2.

Meson	J^P	M (MeV)	Γ (MeV)	Decay Modes	Fraction (Γ_j/Γ)
$K_1(1270)$	1^+	1273 ± 7	87 ± 7	$\Gamma_1 : K\rho$	$(42 \pm 6)\%$
				$\Gamma_2 : K_0^*(1430)\pi$	$(28 \pm 4)\%$
			90 ± 20 †	$\Gamma_3 : K^*(892)\pi$	$(16 \pm 5)\%$
				$\Gamma_4 : K\omega$	$(11.0 \pm 2.0)\%$
				$\Gamma_5 : Kf_0(1370)$	$(3.0 \pm 2.0)\%$
				$\Gamma_6 : \gamma K^0$	*seen*
				$(K^*\pi)_{\mathrm{D-wave}}/(K^*\pi)_{\mathrm{S-wave}}$	1.0 ± 0.7
$K_1(1400)$	1^+	1402 ± 7	174 ± 13	$\Gamma_1 : K^*(892)\pi$	$(94 \pm 6)\%$
				$\Gamma_2 : K\rho$	$(3.0 \pm 3.0)\%$
				$\Gamma_3 : Kf_0(1370)$	$(2.0 \pm 2.0)\%$
				$\Gamma_4 : K\omega$	$(1.0 \pm 1.0)\%$
				$\Gamma_5 : K_0^*(1430)\pi$	*not seen*
				$\Gamma_6 : \gamma K^0$	*seen*
				$(K^*\pi)_{\mathrm{D-wave}}/(K^*\pi)_{\mathrm{S-wave}}$	0.04 ± 0.01
$K^*(1410)$	1^-	1414 ± 15	232 ± 21	$\Gamma_1 : K^*(892)\pi$	$> 40\%$
				$\Gamma_2 : K\pi$	$(6.6 \pm 1.3)\%$
				$\Gamma_3 : K\rho$	$< 7\%$
				$\Gamma_4 : \gamma K^0$	*seen*
$K_2^*(1430)$	2^+	1425.6 ± 1.5	174 ± 13	$\Gamma_1 : K\pi$	$(49.9 \pm 1.2)\%$
				$\Gamma_2 : K^*(892)\pi$	$(24.7 \pm 1.5)\%$
				$\Gamma_4 : K\rho$	$(8.7 \pm 0.8)\%$
				non $K\pi\pi$ modes	
$K^*(1680)$	1^-	1717 ± 27	322 ± 110	$\Gamma_1 : K\pi$	$(38.7 \pm 2.5)\%$
				$\Gamma_2 : K\rho$	$(31.4^{+4.7}_{-2.1})\%$
				$\Gamma_3 : K^*(892)\pi$	$(29.9^{+2.2}_{-4.7})\%$

Table 3.1: Properties of selected strange mesons (†=estimate). Data are reproduced from Ref. [5].

3.2 The K_1 mixing angle

The complicated experimental picture described in the previous section has been attributed to the presence of two kaon resonances, the K_{1A} and K_{1B}, that belong to different $SU(3)$ octets. In the framework of SU(3) it is possible to define the analogs of the G parity, G_V and G_U, for the U and the V spin [58], respectively. The K_{1A} and K_{1B} are then eigenstates of G_V and G_U, although they are not eigenstates of G parity. If the Hamiltonian is invariant under SU(3) transformations, the K_{1A} and K_{1B} cannot mix, as they have opposite G_V parities ($G_V = -C$). When SU(3) is broken, however, the strange members of the $C = +1$ and $C = -1$ can mix, while for the corresponding non-strange states the G parity is still conserved and no mixing occurs.

The mixing relations can be written as:

$$|K_1(1400)\rangle = |K_{1B}\rangle \sin\theta_K + |K_{1A}\rangle \cos\theta_K, \quad (3.1)$$

$$|K_1(1270)\rangle = |K_{1B}\rangle \cos\theta_K - |K_{1A}\rangle \sin\theta_K, \quad (3.2)$$

where the $K_1(1270)$ and $K_1(1400)$ are the mass eigenstates. Different conventions exist for the mixing angle θ_K, and are discussed in Sec. 3.4.2.

A mechanism for the mixing of K_1 mesons was proposed in Ref. [57]. The K_{1A} and K_{1B} states are coupled one another via their decay channels $K^*\pi$ and $K\rho$ [57]:

$$|K_{1A}\rangle \leftrightarrow |K^*\pi\rangle \leftrightarrow |K_{1B}\rangle, \qquad |K_{1A}\rangle \leftrightarrow |K\rho\rangle \leftrightarrow |K_{1B}\rangle \quad (3.3)$$

No mixing is produced in the SU(3) limit, as a cancellation occurs between these concurring transitions.

The effect of a nonzero mixing angle θ_K is to enhance the $K^*\pi$ decay mode and suppress the $K\rho$ for one mass eigenstate, and vice versa for the other one. The value of θ_K has been investigated for many years using different approaches, relying on the available experimental information about the masses, the decay patterns, and the production rates of the $K_1(1270)$ and $K_1(1400)$ mesons in diffractive processes and τ decays [45, 49, 56, 59].

Although a consensus on the value of $|\theta_K|$ has not been reached, yet, most phenomenological papers are based on the values $|\theta_K| = 33°, 58°$ obtained in Ref. [59] from the masses and branching fractions of $K_1(1270)$ and $K_1(1400)$ rates. An analysis of the most recent data of τ decays points to the values $|\theta_K| = (69 \pm 16 \pm 19)°$ or $|\theta_K| = (49 \pm 16 \pm 19)°$ [49]. The ambiguities in the determination on θ_K can in principle be relieved by the study of B decays to $K_1(1270)\gamma$ and $K_1(1400)\gamma$ [61] and charmonium decays to $K_1(1270)^0\bar{K}^0$ and $K_1(1400)^0\bar{K}^0$ [62]. Although currently available data samples are probably too small, high-luminosity experiments at the charm threshold, such as BESIII [63], and future Super B-factories may be able to measure these transitions with sufficient precision.

In this work we extract all the relevant information about the K_1 system, including the θ_K mixing angle, from the K-matrix analysis of the ACCMOR data [45], discussed in Sec. 3.4.

3.3 K_1 resonances in B decays

The production of K_1 mesons in B decays has been observed in the $B \to J/\psi K_1(1270)$ [64], $B \to K_1(1270)\gamma$ [65], and $B \to K_1(1270)\phi$ [66] decay channels. Previous searches for the $B \to K_1(1400)\pi$ transitions resulted in the upper limits $B^0 \to K_1(1400)^+\pi^- < 1.1 \times 10^{-3}$ and $B^+ \to K_1(1400)^0\pi^+ < 2.6 \times 10^{-3}$ at the 90% confidence level (C.L.) [67].

Most searches for rare B meson decays to two-body systems containing an unstable particle, or resonance, rely on the so-called "quasi-two-body" approximation. This approximation rests on the assumption that the decay amplitude can be factorized in a product of sequential two-body decay amplitudes.

Several quasi-two-body decay chains can in principle result in the same multiparticle final state, and models usually have to accommodate for these extra contributions. In order to simplify the analysis of the experimental data, it is common practice to sum up the contribution from each different channel incoherently. Interference effects are either neglected (as in Refs. [64, 65]) or accounted for as sources of systematic uncertainty (as in Ref. [66]). There exist several circumstances under which this is a good approximation:

- the kinematic regions populated by each channel do not significantly overlap, as for two narrow resonances that are separated in mass by several times their widths;
- rapidly varying phases across the phase space are averaged out: they could be associated, e.g., to random combinations of final state particles at reconstruction level (i.e., combinatorial background);
- for selected observables, interference effects between two resonances with different spin-parity quantum numbers are negligible as long as acceptance effects do not spoil the orthogonality condition for the amplitudes (expressed by an integral over the phase space);

- interference with continuum background can be safely neglected, as the $q\overline{q}$ ($q = u, d, s, c$) event topology and kinematics are different from that of $\Upsilon(4S)$ events (as will be discussed in Chapter 4); the impact parameter for B meson daughters is larger, on average, than that for $q\overline{q}$ final state particles, as the B meson lifetime is $\gtrsim 1$ ps; the "tag-side" of the event in the $e^+e^- \to \Upsilon(4S) \to B\overline{B}$ process will be different from that in $e^+e^- \to q\overline{q}$ (tagging information is in fact sometimes used for background suppression).

The K_1 system represents a very special case, as it consists of two wide and overlapping resonances that share the same spin-parity assignment and decay to the same $K\pi\pi$ final state; interference between the two resonances can therefore be sizeable.

For B meson decays to three body final states, Dalitz Plot techniques have proven effective in accounting for the simultaneous presence of several interfering decay channels. For these transitions, the kinematics of the decay in the B rest frame can be fully parameterized in terms of two variables, and therefore represented on a plane. The complete description of a four body decay, in the rest frame of the decaying particle, requires instead five kinematic variables; the techniques devised so far to generalize the Dalitz Plot method to higher-dimensional spaces (e.g., for the analysis of the resonant structures in $D^0 \to K^-\pi^+\pi^+\pi^-$ [68,69]), do not retain the pictorial immediacy of the three-body Dalitz plot. In addition, $B \to K_1\pi$ transitions are expected to be rare, with branching fractions of order 10^{-6} calculated under the naïve factorization hypothesis [70, 71] or in the QCD factorization framework [72]. After accounting for the efficiency, the signal in the reconstructed sample for the $B \to K_1\pi$ analysis is therefore expected to consist of no more than a few hundred events. Although Dalitz Plot analyses have already been performed on three-body rare charmless B decays of comparable rate [73], the increased number of kinematic variables characterizing a four-body decay prevents a full amplitude analysis of the $B \to K_1\pi$ transition at the statistics collected by the present B-factories.

Our approach consists in a quasi-two-body analysis of the $B \to K_1\pi$ decays, in which a single K_1 component accounts for both $K_1(1270)$ and $K_1(1400)$. The primary information extracted in this analysis will therefore be the combined decay rate of B^0 (B^+) mesons into $K_1(1270)^+\pi^-$ and $K_1(1400)^+\pi^-$ ($K_1(1270)^0\pi^+$ and $K_1(1400)^0\pi^+$). (Charge conjugation is implied throughout the text). We allow for interference effects between the K_1 resonances in the three-body $K_1 \to K\pi\pi$ decays. These effects are expressed in terms of a set $\boldsymbol{\zeta}$ of two effective parameters for the relative contribution and phase of the $K_1(1270)$ and $K_1(1400)$ production amplitudes.

The exact interference pattern depends on the detailed distribution of the final state particles, i.e. on the masses, widths, and spins of all the possible intermediate states in the $K\pi\pi$ decay, and on the magnitude and phase of the amplitude for each decay channel. Under the quasi-two-body approximation, we characterize the propagation and decay of the K_1 resonances according to the results of the analysis of the $K\pi\pi$ system produced in diffractive reactions (Sec. 3.4). We'll postpone a detailed description of the model for B decays until Sec. 3.5.

Once the signal model has been defined, it is possible to derive the distributions for any relevant experimental observable from a full Monte Carlo (MC) simulation, taking into account the response of the detector [74]. As shown by previous analyses of B mesons decays to final states containing an axial-vector meson and a pseudoscalar meson [33–35], a particularly useful set of observables is represented by the energy-substituted mass $m_{\rm ES}$, the energy difference ΔE, the Fisher discriminant $\mathcal{F}$ constructed from a linear combination of

topological variables, the reconstructed $K\pi\pi$ invariant mass $m_{K\pi\pi}$, and an angular variable $\mathcal{H}$ related to the spin of the $K\pi\pi$ resonance. These observables are defined and discussed in Sec. 4. The $m_{K\pi\pi}$ distribution, in particular, is sensitive to the relative contribution of the $K_1(1270)$ and $K_1(1400)$ channels. The analytical description of the dependence of the $m_{K\pi\pi}$ distribution on the production parameters $\boldsymbol{\zeta}$ would require the parameterization of acceptance effects in several variables and the evaluation of a multi-dimensional phase space integral. Instead, we sample the $m_{K\pi\pi}$ distribution on the nodes of a grid in the two-dimensional space spanned by the production parameters $\boldsymbol{\zeta}$. At each node, the $m_{K\pi\pi}$ distribution is described with a non-parametrical template modeled upon a MC distribution generated according to the values of $\boldsymbol{\zeta}$ corresponding to that node. In this way it is possible to compare the $m_{K\pi\pi}$ distribution in data with each sampled distribution by means of a scan.

3.4 The partial wave analysis of the $K\pi\pi$ system

The PDG data are largely based on the results obtained by the ACCMOR Collaboration in Ref. [45]. There, a two-resonance, six-channel K-matrix model was used to describe the resonant $K\pi\pi$ $J^P = 1^+$ system in the $K^-p \to K^-\pi^+\pi^-p$ data collected by the WA3 experiment, both at low t' values ($0 \leq |t'| \leq 0.05$ GeV^2) and high t' values ($0.05 \leq |t'| \leq 0.7$ GeV^2, where $|t'|$ is the four momentum transfer squared with respect to the recoiling proton). The data is split into bins, 20 MeV/c^2 wide, of the $K\pi\pi$ invariant mass. For each invariant mass bin, a partial wave analysis [76–78] of the $K^+\pi^+\pi^-$ system was performed. The diffractive production of the ωK^- final state, with $\omega \to \pi^+\pi^-\pi^0$ was also observed, showing a single peaking structure consistent with the one observed in the $K^-\pi^+\pi^-$ final state at ~ 1270 MeV/c^2. However, the ωK data were not further analyzed [45].

The partial wave analysis allows to decompose the $K^+\pi^+\pi^-$ system in states of different spin-parity $J^P = 1^+$, and extract the intensities and relative phases of the contributions from distinct intermediate resonances, angular momenta, and magnetic substates.

In the isobar model the decay of the $K^+\pi^+\pi^-$ system is supposed to always proceed through an intermediate $K\pi$ or $\pi\pi$ state (the *isobar*), represented by a complex factor describing the dependence of the amplitude on the mass of the resonant two-body system (usually a Breit-Wigner function) multiplied with the appropriate spin-parity term. The 1^+ partial waves included by the ACCMOR Collaboration to model the low t' data are $1^+S0^+(K^*\pi)$, $1^+S0^+(\rho K)$, $1^+P0^+(K_0^*(1430)\pi)$, $1^+P0^+(f_0(1370)K)$, $1^+D0^+(K^*\pi)$, where the channels are identified by the notation J^PLM^η followed by the isobar and bachelor particles. With an abuse of notation, we have indicated the $(K\pi)_{\mathrm{S-wave}}$ and $(\pi\pi)_{\mathrm{S-wave}}$ isobars with $K_0^*(1430)$ and $f_0(1370)$, respectively: this notation is consistent with the PDG entries for the K_1 resonances [5]. Here J denotes the total angular momentum, P the parity, L the orbital angular momentum of the bachelor particle (in spectroscopic notation: S for $L = 0$, P for $L = 1$, D for $L = 2$, ...), M and η the magnetic substate of the $K\pi\pi$ system and the naturality of the exchange in the production process [77]. The intensity and phase relative to the $1^+S0^+(K^*\pi)$ amplitude are extracted for each channel.

The results of the partial wave analysis for $J^P = 1^+$ waves in low t' data are shown in Fig. 3.1. Points and error bars have been reproduced from Fig. 13 of Ref. [45] by reading the graphs from a scanned copy of the article (several software tools exist to extract data points from the digital version of a scientific publication). Following the paper by the ACCMOR Collaboration [45], we fit the intensity and phase differences for the 1^+ waves with a K-

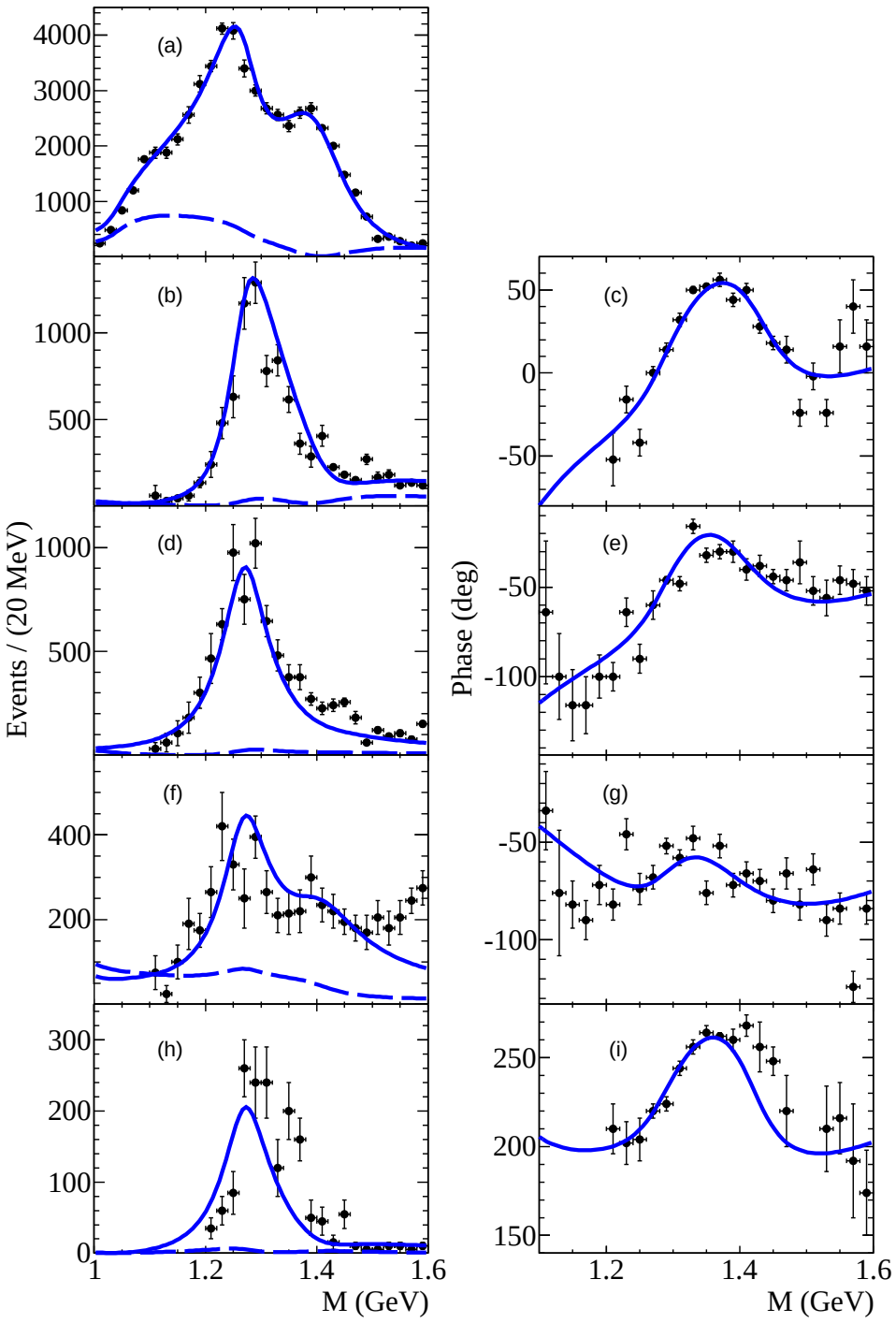

Figure 3.1: Points with error bars: results of the partial wave analysis of the $K^-\pi^+\pi^-$ system in low t' WA3 data [45] for $J^P = 1^+$ waves, reproduced from Fig. 13 in Ref. [45]. Intensity (left) and phase relative to the $1^+S0^+(K^*\pi)$ amplitude (right) for the (a) $1^+S0^+(K^*\pi)$, (b, c) $1^+S0^+(\rho K)$, (d, e) $1^+P0^+(K_0^*(1430)\pi)$, (f, g) $1^+P0^+(f_0(1370)K)$, and (h, i) $1^+D0^+(K^*\pi)$ channels. The solid lines represent the K-matrix model fit to data, and the dashed lines the contribution from the background.

matrix model in the *P-vector approach* [79]. We are induced to repeat the fit performed by ACCMOR by the fact that only a subset of the fitted values for the parameters of the model are reported in Ref. [45]. Furthermore, the observed intensity and phase shifts in Fig. 3.1 cannot be used directly, as they include the contribution of the background.

3.4.1 The model

A K-matrix formulation may be useful whenever two nearby and potentially overlapping resonances are present and the violation of the unitarity of the scattering amplitudes is of concern; it has been extensively used in the past to parameterize two-body reactions of the type $ab \to cd$.

The formulation of Ref. [79] generalizes the K-matrix formalism to describe the production of resonances in more complex reactions. The key assumption underlying the *P-vector approach* is that the two-body system in the final state is an isolated one and that the two particles do not interact with the rest of the final state in the production process.

Although the formulation adopted by ACCMOR for the K-matrix is not the most general possible, and although several parameterizations other than a K-matrix could be used [78], we are mainly concerned with obtaining a reliable description of the relative intensity and phases between the amplitudes of the different decay channels, for each one of the K_1 resonances.

ACCMOR's model accounts for the production of two K_1 resonances that are allowed to decay in six channels (the numbering will be retained throughout this work): 1) $1^+S0^+(K^*\pi)$, 2) $1^+S0^+(\rho K)$, 3) $1^+P0^+(K_0^*(1430)\pi)$, 4) $1^+P0^+(f_0(1370)K)$, 5) $1^+D0^+(K^*\pi)$ and 6) $1^+S0^+(\omega K)$. In the following, the index a will indicate the K_1 state of higher mass (i.e. the $K_1(1400)$), and the index b will denote the K_1 state of lower mass (i.e. the $K_1(1270)$). In order to be consistent with the partial wave analysis of the WA3 data, we describe the isobars in the model with the parameters reported in Table 3.2.

Isobar	Mean mass (GeV/c^2)	Width (GeV)	References
K^*	0.896	0.051	[5]
ρ	0.776	0.146	[5]
K_0^*	1.250	0.600	[45]
$f_0(1370)$	1.256	0.400	[80]
ω	0.783	0.008	[5]

Table 3.2: Parameters for the isobars used in the K-matrix model.

We parameterize the production amplitude for each channel in the reaction $K^-p \to (K^-\pi^+\pi^-)p$ as

$$F_i = e^{i\delta_i} \sum_j (\mathbf{1} - i\mathbf{K}\boldsymbol{\rho})^{-1}_{ij} P_j, \tag{3.4}$$

where the index i (and similarly j) represents the i^{th} channel [79]. The δ_i parameters are offset phases with respect to the $1^+S0^+(K^*\pi)$ channel ($\delta_1 \equiv 0$): they are introduced and left float in the fit in order to accommodate for any mismatch between the data and the assumptions made in the partial wave analysis or in the fitting amplitudes [45, 76, 81].

The K-matrix is real and symmetric by construction. The dominance of the two K_1 resonances in the dynamical behavior of the amplitudes is signalled by the presence of two

poles in the K-matrix **K**:

$$K_{ij} = \frac{f_{ai} f_{aj}}{M_a - M} + \frac{f_{bi} f_{bj}}{M_b - M}, \tag{3.5}$$

where M is the $K\pi\pi$ invariant mass, and the poles M_a and M_b are real [82]. Since the model comprises six channels, the K-matrix is a 6×6 matrix. The decay couplings $f_{\alpha i}$ ($\alpha = a, b$) are defined as the products

$$f_{\alpha i} = g_{\alpha_i} B_i^L(M) \tag{3.6}$$

of a decay constant $g_{\alpha i}$ (real, but allowed to be negative) and a centrifugal barrier factor B_i^L. The barrier factors B_i^L are given by [76]:

$$B_i^L(M) = \left[\frac{q_i(M)^2 R^2}{1 + q_i(M)^2 R^2} \right]^{L/2}, \tag{3.7}$$

where q_i is the breakup momentum in channel i. Typical values for the interaction radius squared R^2 [83] are in the range $5 < R^2 < 100$ GeV^{-2} [81] and the value $R^2 = 25$ GeV^{-2} is used.

As seen above, the physical resonances $K_1(1270)$ and $K_1(1400)$ are mixtures of the two SU(3) octet states K_{1A} and K_{1B}. Assuming that SU(3) violation manifests itself only in the mixing, we impose the following relations [45, 82]:

$$g_{a1} = \tfrac{1}{2}\gamma_+ \cos\theta_K + \sqrt{\tfrac{9}{20}}\gamma_- \sin\theta_K, \tag{3.8}$$

$$g_{b1} = -\tfrac{1}{2}\gamma_+ \sin\theta_K + \sqrt{\tfrac{9}{20}}\gamma_- \cos\theta_K, \tag{3.9}$$

$$g_{a2} = \tfrac{1}{2}\gamma_+ \cos\theta_K - \sqrt{\tfrac{9}{20}}\gamma_- \sin\theta_K, \tag{3.10}$$

$$g_{b2} = -\tfrac{1}{2}\gamma_+ \sin\theta_K - \sqrt{\tfrac{9}{20}}\gamma_- \cos\theta_K, \tag{3.11}$$

where γ_+ and γ_- are the couplings of the SU(3) octet states to the ρK and $K^*\pi$ S-wave channels:

$$\langle K^*\pi | K_{1A} \rangle = \tfrac{1}{2}\gamma_+ = \langle \rho K | K_{1A} \rangle, \tag{3.12}$$

$$\langle \rho K | K_{1B} \rangle = -\sqrt{\tfrac{9}{20}}\gamma_- = -\langle K^*\pi | K_{1B} \rangle. \tag{3.13}$$

Since the ωK data were not analyzed by the ACCMOR Collaboration [45], the parameters for the ωK channel are not fitted and the couplings to the ωK channel are fixed to $1/\sqrt{3}$ of the ρK couplings [45], as follows from the quark model.

The decay of the $K^-\pi^+\pi^-$ system can be expressed as the decay chain

$$K_1 \to V_3 + h_4,\ V_3 \to h_5 + h_6, \qquad h = \pi, K\ , \tag{3.14}$$

i.e., the isobar V_3 in the two body final state $V_3 + h_4$ is an unstable particle V_3 itself, that decays to the $h_5 + h_6$ system. Therefore, the $V_3 + h_4$ system is often referred to as a *quasi-two-body* final state. In order to account for the unstable nature of the isobar, the phase space for this decay chain is taken as the two particle phase space element evaluated

at the complex mass of V_3. The elements of the diagonal phase space matrix $\boldsymbol{\rho}(M)$ are therefore approximated with the (non-relativistic) form:

$$\rho_{ij}(M) = \frac{2\delta_{ij}}{M}\sqrt{\frac{2m^* m_4}{m^* + m_4}(M - m^* - m_4 + i\Delta)}, \tag{3.15}$$

where m_4 is the mass of the bachelor particle h_4, and m^* (Δ) is the pole mass (half width) of the intermediate resonance state V_3 [84].

The production vector $\mathbf{P}$ consists of a background term $\mathbf{D}$ [81, 85, 86] and a direct production term $\mathbf{R}$, according to the following relation among vector elements:

$$P_i = R_i + \sum_j (1 + i\tau K_{ij}) D_j, \tag{3.16}$$

where τ is a constant.

$\mathbf{R}$ is given by

$$R_i = \frac{f_{pa} f_{ai}}{M_a - M} + \frac{f_{pb} f_{bi}}{M_b - M}, \tag{3.17}$$

where f_{pa} and f_{pb} represent the amplitudes for producing the states $K_1(1400)$ and $K_1(1270)$, respectively, and are complex numbers. As the overall phase can be chosen arbitrarily, we assume f_{pa} to be real. We furthermore assume f_{pa} and f_{pb} don't depend on M.

A typical feature of diffractive reactions is the production of systems that show up as bumps at rather small masses but do not correspond to resonances [87]. Such systems seem to be produced in diffractive reactions only. A dynamical model (the Deck effect [88]) was proposed to describe the diffractive production of such nonresonant systems. This mechanism is connected with diffractive excitation seen as a general consequence of the composite nature of hadrons. Pictorially, a pion component in the incident hadron may be perturbed by the proton incoming at not too small an impact parameter [87]. A feature that could be ascribed to such a mechanism can be observed in Fig. 3.1(a) at $M \sim 1.1$ GeV/c^2.

The Deck background amplitudes are parameterized by a complex amplitude $D_i^{(0)} e^{i\phi_i}$ modulated by a mass dependence of the form proposed in Ref. [89]:

$$D_i = D_i^{(0)} e^{i\phi_i} \frac{1}{M^2 - M_K^2} B_i^L(M) \tag{3.18}$$

where M_K is the mass of the incident kaon. For the $1^+ D0^+(K^*\pi)$ channel we set $D_5^{(0)} = 0$ as in the ACCMOR analysis [45]. For the ωK channel we set $D_6^{(0)} = 0$ (choosing $D_6^{(0)} = 1/\sqrt{3} D_2^{(0)}$ doesn't affect the results appreciably).

Including the bare Deck amplitude Eq. 3.18 in the production vector $\mathbf{P}$ accounts for the effects of rescattering through the K_1 resonances, as illustrated in Ref. [81, 85, 90] for a K-matrix model with one resonance and one channel. The form in Eq. 3.16 represents the generalization to a K-matrix model with more resonances and more decay channels. The term multiplied by the constant τ in Eq. 3.16 (in the following, we'll refer to it as the "τ-term") is introduced when expressing the Deck background amplitude as proposed in Ref. [90]. In this model, the constant τ measures the separation in space of the produced particles. In particular, for localized production processes τ is large, while the spatially diffuse Deck mechanism corresponds to small values of τ. The ACCMOR Collaboration finds a value $\tau = 0.4$ to be appropriate for the small $|t'|$ region ($0 < |t'| < 0.05$ GeV^2)

considered here. This value was obtained from the analysis of the diffractive production of the 3π system [81, 91] and was used also for the analysis of the $K\pi\pi$ system, which relies on the same model.

The ACCMOR's fit to the results of the $K\pi\pi$ partial wave analysis was not sensitive to the value of τ [45]. It should be noted, however, that if τ is fixed to a nonzero value, the amount of background depends on the exact choice of the normalization used for the phase space term. In particular, if this choice greatly differs from the one used by the ACCMOR's Collaboration, fixing the same value $\tau = 0.4$ in the fit could result in the τ-term dominating the total background amplitude. Since the τ-term has the same poles as the direct production term R, overestimating τ would undermine the stability of the fit, that might therefore erroneously ascribe the peaking structures in Fig. 3.1 to background, as in Ref. [54] (Fig. 6). We choose therefore to fix τ to 0, so that we are left with a production term similar to the one used in [86]:

$$P_i = R_i + D_i. \tag{3.19}$$

This is a legitimate approximation, as the Deck background corresponds to small values of τ [90], as stated above.

3.4.2 Correspondence between different notations

Before proceeding to the fit, we want to clear any potential issues in the interpretation of the results, that may arise from the use, in the literature, of at least three different sets of notations. In this section we will illustrate the notations used in Refs. [45], [56], and [59], and identify the correspondence between the different conventions.

In order to uniform the notation, we'll use $|h\rangle$ to indicate $|K_1(1400)\rangle$ (i.e. $|Q_a\rangle$ in ACCMOR notation [45] and $|Q_2\rangle$ in SLAC notation [56]; "h" is for "higher mass") and $|l\rangle$ to indicate $|K_1(1270)\rangle$ (i.e. $|Q_b\rangle$ in ACCMOR notation [45] and $|Q_1\rangle$ in SLAC notation [56]; "l" is for "lower mass"). For the $|K_{1A}\rangle$ and $|K_{1B}\rangle$ states (A for the a_1 $C = +1$ multiplet, B for the b_1 $C = -1$ multiplet), we'll use $|+\rangle$ (for $C = +1$) and $|-\rangle$ (for $C = -1$), respectively.

For the couplings we'll retain the notation specific to each paper, therefore for the couplings of the $|+\rangle$ state we'll use γ_+ (ACCMOR [45]), g_K (SLAC [56]), f_a (Suzuki [59]); for the couplings of the $|-\rangle$ state we'll use γ_- (ACCMOR [45]), g_B (SLAC [56]), f_b (Suzuki [59]). As for the mixing angle, θ_K will refer to the ACCMOR convention (as this is the default notation in this work, K refers to K_1), θ_C to SLAC (C for Carnegie) and θ_S to Suzuki's notation [59].

Suzuki notation

In the Suzuki paper [59], the mixing relations are defined in Eq. (2.5) as:

$$\begin{aligned} |h\rangle &= |+\rangle \cos\theta_S - |-\rangle \sin\theta_S, \\ |l\rangle &= |+\rangle \sin\theta_S + |-\rangle \cos\theta_S. \end{aligned} \tag{3.20}$$

The couplings are defined in Eq. (2.3) and (2.4) [59]:

$$\begin{aligned}
\langle K^*\pi|h\rangle &= +\frac{1}{2}f_a\cos\theta_S + \frac{3}{\sqrt{20}}f_b\sin\theta_S, \\
\langle K^*\pi|l\rangle &= -\frac{1}{2}f_a\sin\theta_S + \frac{3}{\sqrt{20}}f_b\cos\theta_S, \\
\langle \rho K|h\rangle &= +\frac{1}{2}f_a\cos\theta_S - \frac{3}{\sqrt{20}}f_b\sin\theta_S, \\
\langle \rho K|l\rangle &= -\frac{1}{2}f_a\sin\theta_S - \frac{3}{\sqrt{20}}f_b\cos\theta_S.
\end{aligned} \tag{3.21}$$

The relative phases of the ρK and $K^*\pi$ decay amplitudes are opposite for the $C = +1$ and $C = -1$ state as stated in Ref. [57]:

$$\langle K^*\pi|+\rangle = -\langle \rho K|+\rangle, \quad \langle K^*\pi|-\rangle = +\langle \rho K|-\rangle. \tag{3.22}$$

ACCMOR notation

In the ACCMOR paper [45], the mixing relations are:

$$\begin{aligned}
|h\rangle &= +|+\rangle\cos\theta_K + |-\rangle\sin\theta_K, \\
|l\rangle &= -|+\rangle\sin\theta_K + |-\rangle\cos\theta_K,
\end{aligned} \tag{3.23}$$

while the couplings are defined as [45]:

$$\begin{aligned}
\langle K^*\pi|h\rangle &= +\frac{1}{2}\gamma_+\cos\theta_K + \frac{3}{\sqrt{20}}\gamma_-\sin\theta_K, \\
\langle K^*\pi|l\rangle &= -\frac{1}{2}\gamma_+\sin\theta_K + \frac{3}{\sqrt{20}}\gamma_-\cos\theta_K, \\
\langle \rho K|h\rangle &= +\frac{1}{2}\gamma_+\cos\theta_K - \frac{3}{\sqrt{20}}\gamma_-\sin\theta_K, \\
\langle \rho K|l\rangle &= -\frac{1}{2}\gamma_+\sin\theta_K - \frac{3}{\sqrt{20}}\gamma_-\cos\theta_K.
\end{aligned} \tag{3.24}$$

The relative phases of the ρK and $K^*\pi$ decay amplitudes are opposite to those in Suzuki [59]:

$$\langle K^*\pi|+\rangle = +\langle \rho K|+\rangle, \quad \langle K^*\pi|-\rangle = -\langle \rho K|-\rangle. \tag{3.25}$$

However, we can to redefine the sign of the $K^*\pi$ state so that the same relation as in Ref. [59] is obtained:

$$\begin{aligned}
\langle K^*\pi|h\rangle &= -\frac{1}{2}\gamma_+\cos\theta_K - \frac{3}{\sqrt{20}}\gamma_-\sin\theta_K, \\
\langle K^*\pi|l\rangle &= +\frac{1}{2}\gamma_+\sin\theta_K - \frac{3}{\sqrt{20}}\gamma_-\cos\theta_K, \\
\langle \rho K|h\rangle &= +\frac{1}{2}\gamma_+\cos\theta_K - \frac{3}{\sqrt{20}}\gamma_-\sin\theta_K, \\
\langle \rho K|l\rangle &= -\frac{1}{2}\gamma_+\sin\theta_K - \frac{3}{\sqrt{20}}\gamma_-\cos\theta_K.
\end{aligned} \tag{3.26}$$

It can be noticed that it is now possible to find a correspondence between the couplings in Suzuki convention [59] and those in ACCMOR convention [45] by identifying:

$$\theta_K \leftrightarrow -\theta_S, \quad \gamma_+ \leftrightarrow f_a, \quad \gamma_- \leftrightarrow -f_b. \tag{3.27}$$

SLAC notation

Finally, in the SLAC notation [56], the couplings are defined as:

$$\begin{aligned}
\langle K^*\pi|h\rangle &= -\frac{1}{2}g_K\sin\theta_C + \frac{3}{\sqrt{20}}g_B\cos\theta_C, \\
\langle K^*\pi|l\rangle &= +\frac{1}{2}g_K\cos\theta_C + \frac{3}{\sqrt{20}}g_B\sin\theta_C, \\
\langle \rho K|h\rangle &= -\frac{1}{2}g_K\sin\theta_C - \frac{3}{\sqrt{20}}g_B\cos\theta_C, \\
\langle \rho K|l\rangle &= +\frac{1}{2}g_K\cos\theta_C - \frac{3}{\sqrt{20}}g_B\sin\theta_C.
\end{aligned} \tag{3.28}$$

This choice corresponds to identifying:

$$\theta_C \leftrightarrow \frac{\pi}{2} - \theta_K, \quad g_K \leftrightarrow \gamma_+, \quad g_B \leftrightarrow -\gamma_-. \tag{3.29}$$

3.4.3 Ambiguities

There appear to be several ambiguities for the best fit of the K-matrix model to the ACCMOR data [45]. Here we identify and characterize the most relevant for the analysis. For simplicity we consider only the $K^*\pi$ and ρK S-wave channels (two intensities and one relative phase). As we have defined the Q_a meson to represent the state of higher mass, we have not considered ambiguities that can be reduced to an interchange of the Q_a and Q_b mass poles (i.e. $M_a \leftrightarrow M_b$).

In order to conduct this study, we have investigated the behavior of the ratio of $K^*\pi$ and ρK production amplitudes (Eq. 8 in Ref. [82]):

$$\alpha e^{i\beta} = \frac{f_{a2}(M_b - M) + g f_{b2}(M_a - M) + i\rho_1(f_{a2}f_{b1} - f_{a1}f_{b2})(g f_{a1} - f_{b1})}{f_{a1}(M_b - M) + g f_{b1}(M_a - M) + i\rho_2(f_{a1}f_{b2} - f_{a2}f_{b1})(g f_{a2} - f_{b2})}, \tag{3.30}$$

where we have defined (following ACCMOR):

$$f_{a1} \equiv \langle K^*\pi|h\rangle, \quad f_{b1} \equiv \langle K^*\pi|l\rangle, \quad f_{a2} \equiv \langle \rho K|h\rangle, \quad f_{b2} \equiv \langle \rho K|l\rangle, \tag{3.31}$$

and g is the ratio f_{pb}/f_{pa} of the production parameters for the $|h\rangle$ (f_{pa}) and $|l\rangle$ (f_{pb}) states. It is always possible to choose $f_{pa} > 0$ (i.e. real and positive).

We identify the following set of potential ambiguities (the others can result from a combination of any number of them):

1. $\theta_K \mapsto \theta_K + \pi$, $\gamma_\pm$ unchanged; $\theta_K \mapsto \theta_K + \pi$, $\gamma_\pm \mapsto -\gamma_\pm$; because of this, it is possible to restrict the discussion to values of θ_K in the $[-\pi/2, \pi/2]$ range;

2. $\theta_K \mapsto -\theta_K + \pi$, $\gamma_- \mapsto -\gamma_-$, $f_{pb} \mapsto -f_{pb}$, γ_+ unchanged;

3. $\theta_K \mapsto \theta_K - \pi/2$, $\gamma_+ \mapsto \gamma_-$, $\gamma_- \mapsto -\gamma_+$; however, this transformation doesn't leave $\alpha e^{i\beta}$ invariant: instead, $\alpha e^{i\beta} \mapsto -\alpha e^{i\beta}$, i.e. $\beta \mapsto \beta + \pi$. In the ACCMOR fit model, small phase shifts between the model and the data are allowed. They are accounted for by the "offset phases" δ_i; we anticipate from Sec. 3.4.4 that the fit to the ACCMOR data [45] yields $\theta_K \sim 70°$, and that this solution is associated to "small" (i.e. $|\delta_i| < 90°$) offset phases. The companion solution for $\theta_K \mapsto \theta_K - \pi/2$ is associated to offset phases of order π (i.e. $\delta_i \mapsto \delta_i + \pi$) and is therefore disfavored by data. We will not consider this ambiguity further.

3.4.4 Results of the fit

The production amplitudes were fitted to the intensity of the five $K\pi\pi$ channels in Fig. 3.1 together with the phases measured relative to $1^+S0^+(K^*\pi)$ amplitude [45].

We write the intensities as: [92]

$$I(M) = \frac{1}{2}\ |F_i(M)|^2\ \ \mathrm{Re}\,\rho_i(M), \tag{3.32}$$

while the relative phases are given by:

$$\psi(M) = \arg\left[\frac{F_i(M)}{F_1(M)}\right]. \tag{3.33}$$

Following the analysis of Section 3.4.3, we seek solutions corresponding to positive values of the γ_+ parameters, as found in the ACCMOR analysis [45]. The data sample consists of 215 bins. The results of this fit are displayed in Fig. 3.1 and show a good qualitative agreement with the results obtained by the ACCMOR Collaboration [45].

We obtain $\chi^2 = 855$, with 26 free parameters, while the ACCMOR Collaboration obtained $\chi^2 = 529$. We interpret this difference as due to slight inaccuracies in extracting the errors on the data points from the WA3 paper [45]. These discrepancies do not appreciably affect the extracted central values and errors of the parameters of the model, summarized in Table 3.3, and are therefore innocuous for the purposes of the present work. Although neither fit is formally a good one, the model succeeds in reproducing the relevant features of the data.

Figure 3.1 also shows the background only contribution to the intensity of each channel. We don't observe the large background contributions claimed in Ref. [54]. Instead, the Deck background accounts for the low-mass bump in the $1^+S0^+(K^*\pi)$ intensity, as expected. The K-matrix model after background-removal is shown in Fig. 3.2. In particular, the effect of the Deck background on the relative phases for each channel can be inferred from the plots.

The errors in Table 3.3 are of systematic origin and are derived by shifting the mass scale of the histogram by ± 20 MeV, corresponding to the interval of the binning. Errors have been calculated only for the parameters that enter the model for B decays, described in Sec. 3.5.

3.5 Model for K_1 mesons production in B decays

The K-matrix model introduced above has been adapted to describe the production of K_1 mesons in B decays in the quasi-two-body analysis outlined in Sec. 3.3. The Deck background is removed from the model, as Deck background is expected to be negligible in non-diffractive processes [92]. In this way, the K-matrix accounts for the K_1 signal contribution only, while the backgrounds arising from resonant and non-resonant B decays to the $(K\pi\pi)\pi$ final state will be taken into account separately.

The parameters of the K-matrix can be classified in two sets: the first set of parameters describes the propagation and decay of the K_1 resonances, while the second set describes the production of the K_1 system. This is illustrated pictorially in Fig. 3.3. The first set comprises the mass poles M_α ($\alpha = \{a, b\}$), the decay constants $g_{\alpha,i}$, and the offset phases. Under the factorization assumption, the values for these parameters can be fixed

Parameter	Fitted value	Values in Ref. [45]
M_a	1.40 ± 0.02	1.40 ± 0.02
M_b	1.16 ± 0.02	1.17 ± 0.02
θ	$72° \pm 3°$	$64° \pm 8°$
γ_+	0.75 ± 0.03	0.78 ± 0.1
γ_-	0.44 ± 0.03	0.54 ± 0.1
g_{a3}	0.02 ± 0.03	
g_{b3}	0.32 ± 0.01	
g_{a4}	-0.08 ± 0.02	
g_{b4}	0.16 ± 0.01	
g_{a5}	0.06 ± 0.01	
g_{b5}	0.21 ± 0.04	
δ_2	$-31° \pm 1°$	$\sim -30°$
δ_3	$82° \pm 2°$	$\sim 90°$
δ_4	$78° \pm 4°$	$\sim 90°$
δ_5	$20° \pm 9°$	$\sim 0°$
f_{pa}	18	11
$\mathrm{Re}(f_{pb})$	-22	-23
$\mathrm{Im}(f_{pb})$	5	-13
$\mathrm{Re}(D_1^{(0)}e^{i\phi_1})$	65	
$\mathrm{Im}(D_1^{(0)}e^{i\phi_1})$	21	
$\mathrm{Re}(D_2^{(0)}e^{i\phi_2})$	-30	
$\mathrm{Im}(D_2^{(0)}e^{i\phi_2})$	-14	
$\mathrm{Re}(D_3^{(0)}e^{i\phi_3})$	16	
$\mathrm{Im}(D_3^{(0)}e^{i\phi_3})$	9	
$\mathrm{Re}(D_4^{(0)}e^{i\phi_4})$	16	
$\mathrm{Im}(D_4^{(0)}e^{i\phi_4})$	-20	

Table 3.3: Parameters for the K-matrix model extracted from the fit to the WA3 data.

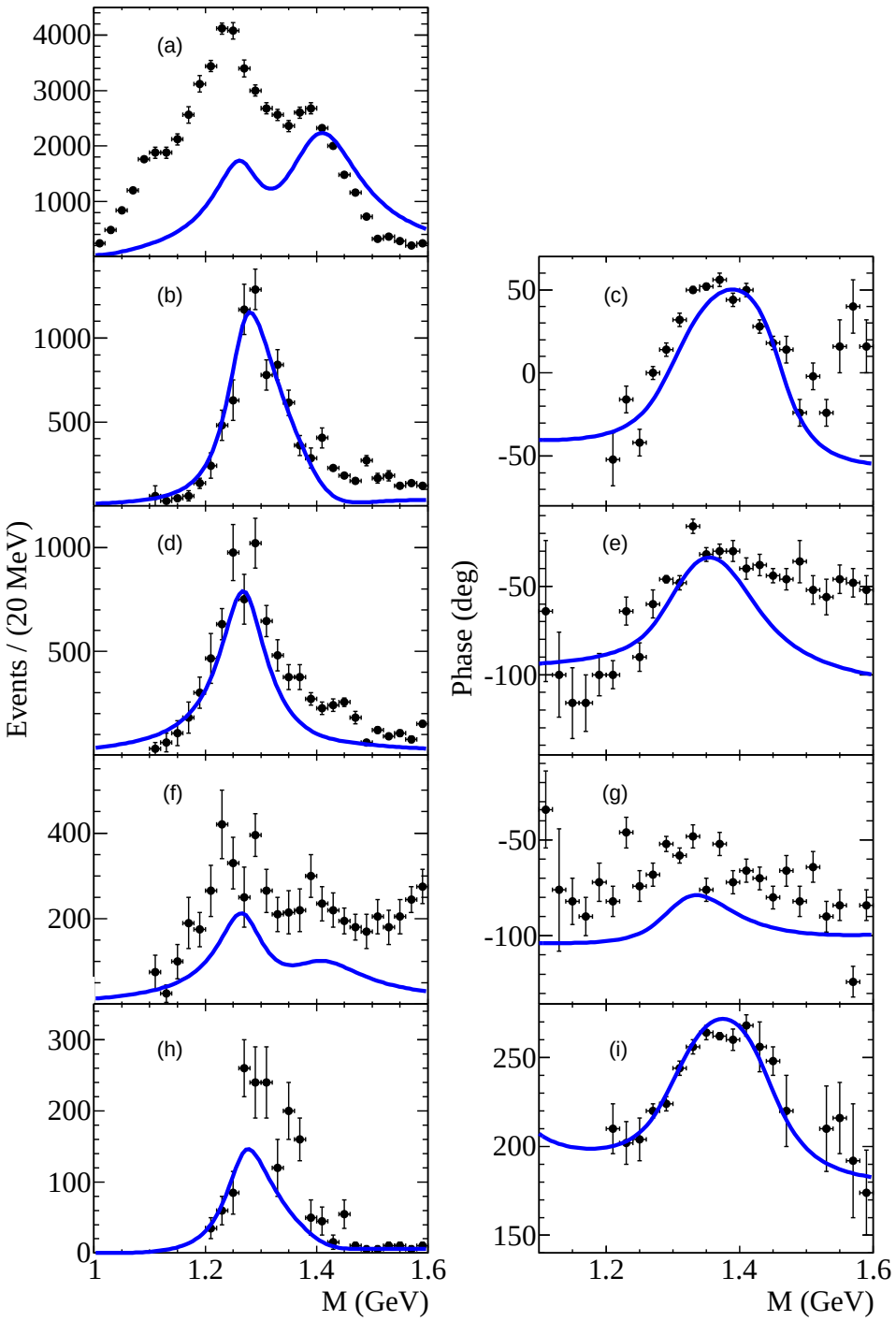

Figure 3.2: Points with error bars: results of the partial wave analysis of the $K^-\pi^+\pi^-$ system in low t' WA3 data [45] for $J^P = 1^+$ waves, reproduced from Fig. 13 in Ref. [45]. Intensity (left) and phase relative to the $1^+S0^+(K^*\pi)$ amplitude (right) for the (a) $1^+S0^+(K^*\pi)$, (b, c) $1^+S0^+(\rho K)$, (d, e) $1^+P0^+(K_0^*(1430)\pi)$, (f, g) $1^+P0^+(f_0(1370)K)$, and (h, i) $1^+D0^+(K^*\pi)$ channels. The solid lines represent the K-matrix model fit to data, after removing the contribution from the Deck background.

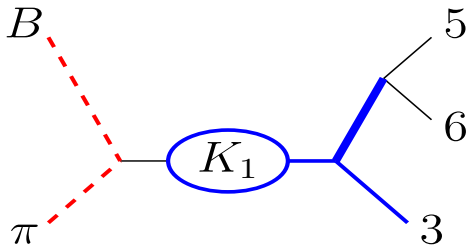

Figure 3.3: Diagram illustrating the K-matrix description of the production of K_1 resonances in B decays. The dashed line connecting the B meson to the π is associated to the P-vector, while the K_1 propagator and the K_1 decay are described by the K-matrix.

to those extracted from the fit to the ACCMOR data, since the decay of the K_1 mesons is independent on the production process.

The second set includes the complex production parameters f_{pa}, f_{pb}, that provide an effective parameterization of the interference effects in the $B \to K_1\pi$ process. Since one global phase is arbitrary, the production parameters can be written in terms of three real parameters. The production terms can be normalized so that $|f_{pa}|^2 + |f_{pb}|^2 = 1$, by introducing two real production parameters $\boldsymbol{\zeta} = (\vartheta, \phi)$: $f_{pa} \equiv \cos\vartheta$, $f_{pb} \equiv \sin\vartheta e^{i\phi}$, where $\vartheta \in [0, \pi/2]$, $\phi \in [0, 2\pi]$. In this parameterization, $\tan\vartheta$ represents the magnitude of the production constant for the $K_1(1270)$ resonance relative to that for the $K_1(1400)$ resonance, while ϕ is the relative phase. This parameterization is convenient when performing a scan over the production parameters $\boldsymbol{\zeta}$, since the physical ranges of ϑ and ϕ are finite. The third real parameter is the normalization of the signal contribution and is represented by the combined branching fraction of B decays to $K_1(1270)\pi$ and $K_1(1400)\pi$.

For given values of $\boldsymbol{\zeta}$, signal MC samples for B decays to the $(K\pi\pi)\pi$ final states can be generated by weighting the $(K\pi\pi)\pi$ population according to the amplitude $\sum_{i\neq\omega K}\langle K\pi\pi|i\rangle F_i$, where the term $\langle K\pi\pi|i\rangle$ consists of a factor describing the angular distribution of the $K\pi\pi$ system resulting from the K_1 decay, an amplitude for the resonant $\pi\pi$ and $K\pi$ systems, and isospin factors, and is calculated using the formalism described in Refs. [45, 76]. The ωK channel is excluded from the sum, since the $\omega \to \pi^+\pi^-$ branching fraction is only $(1.53^{+0.11}_{-0.13})\,\%$, compared to the branching fraction $(89.2 \pm 0.7)\,\%$ of the dominant decay $\omega \to \pi^+\pi^-\pi^0$ [5]. Most of the $K_1 \to \omega K$ decays therefore result in a different final state than the reconstructed one.

Mass distributions

For the $\pi\pi$ and $K\pi$ resonances, the following ℓ-wave Breit-Wigner parameterization is used [76]:

$$BW(m) = (\pi)^{-1/2}\frac{[m_0\Gamma(m)]^{1/2}}{(m_0^2 - m^2) - im_0\Gamma(m)} \tag{3.34}$$

with

$$\Gamma(m) = \Gamma(m_0)\frac{m_0}{m}\left[\frac{q(m)}{q(m_0)}\right]^{2\ell+1}\left[\frac{1 + R^2q^2(m_0)}{1 + R^2q^2(m)}\right]^{\ell}, \tag{3.35}$$

where m_0 is the nominal mass of the resonance, $\Gamma(m)$ is the mass-dependent width, $\Gamma(m_0)$ is the nominal width of the resonance, q is the breakup momentum of the resonance into the two-particle final state, and $R^2 = 25\ \text{GeV}^{-2}$.

The $K_0^*(1430)$ and $f_0(1370)$ amplitudes are also parameterized as Breit-Wigner functions. For the $K_0^*(1430)$ we assume a mass of 1.250 GeV and a width of 0.600 GeV [45], while for the $f_0(1370)$ we use a mass of 1.256 GeV and a width of 0.400 GeV [80]. As the resonant structure of the $(K\pi)_{\rm S-wave}$ and $(\pi\pi)_{\rm S-wave}$ systems is not well known, in Sec. 5.8 we replace the Breit-Wigner formulation for these channels with a phase-shift parameterization, and evaluate a systematic uncertainty.

Angular distributions

In Fig. 3.4 we show the reference frame [76] chosen to evaluate the distributions of the products of $B \to K_1\pi$ decays, where K_1 decays proceed through the intermediate resonances $X_s = \{K^*(892), K_0^*(1430)\}$ or $X_d = \{\rho, f_0(1370), \omega\}$. Final state particles are labeled with a subscript $\{k, l, m, n\}$, according to the following scheme: $B^0 \to K_1^+\pi_k^-$, $K_1^+ \to X_s^0\pi_l^+$, $X_s^0 \to K_m^+\pi_n^-$ or $B^0 \to K_1^+\pi_k^-$, $K_1^+ \to X_d^0 K_l^+$, $X_d^0 \to \pi_m^+\pi_n^-$ for neutral B meson decays, and $B^+ \to K_1^0\pi_k^+$, $K_1^0 \to X_s^+\pi_l^-$, $X_s^+ \to K_m^0\pi_n^+$ or $B^+ \to K_1^0\pi_k^+$, $K_1^0 \to X_d^0 K_l^0$, $X_d^0 \to \pi_m^+\pi_n^-$ for charged B meson decays. The angular distribution for the K_1 system produced in B decays can be expressed in terms of three independent angles (Θ, β, Φ). In the K_1 rest frame, we define the Y axis as the normal to the decay plane of the K_1, and orient the Z axis along the momentum of l (Fig. 3.4a). Θ and Φ are then the polar and azimuthal angles of the momentum of k, respectively, in the K_1 rest frame (Fig. 3.4b). We define β as the polar angle of the flight direction of m relative to the direction of the momentum of l (Fig. 3.4c).

In the helicity formalism, the angular function for the transition amplitude is given by [75]

$$A = \sum_{-j\le\lambda\le j} C(L, j, J|0, -\lambda) D^{J*}_{0,-\lambda}(\Phi, \Theta, -\Phi) d^j_{-\lambda,0}(\beta), \tag{3.36}$$

where the notation reflects the one in [76]. The resulting angular parts of the transition amplitudes for S-, P-, and D-wave decays of the K_1 axial vector ($J^P = 1^+$) mesons with scalar ($J^P = 0^+$) and vector ($J^P = 1^-$) intermediate resonances $X_{s,d}$ are given by:

$$A_S \propto \cos\Theta\cos\beta + \sin\Theta\sin\beta\cos\Phi, \tag{3.37}$$

$$A_P \propto \cos\Theta, \tag{3.38}$$

$$A_D \propto -2\cos\Theta\cos\beta + \sin\Theta\sin\beta\cos\Phi. \tag{3.39}$$

Isospin factors

For the most abundant K_1 decay channels we calculate:

$$\langle K^+\pi^-\pi^+|1^+S(K^*\pi)\rangle = \frac{\sqrt{2}}{3} A_S(\mathbf{p}_{\pi^+}, \mathbf{p}_{K^+}) BW_{\ell=0}(K^+\pi^-) \tag{3.40}$$

$$\langle K^+\pi^-\pi^+|1^+S(\rho K)\rangle = \frac{1}{\sqrt{6}} A_S(\mathbf{p}_{K^+}, \mathbf{p}_{\pi^+}) BW_{\ell=0}(\pi^+\pi^-) \tag{3.41}$$

$$\langle K^+\pi^-\pi^+|1^+P(K_0^*\pi)\rangle = \frac{\sqrt{2}}{3} A_P(\mathbf{p}_{\pi^+}, \mathbf{p}_{K^+}) BW_{\ell=1}(K^+\pi^-) \tag{3.42}$$

$$\langle K^+\pi^-\pi^+|1^+D(K^*\pi)\rangle = \frac{\sqrt{2}}{3} A_D(\mathbf{p}_{\pi^+}, \mathbf{p}_{K^+}) BW_{\ell=2}(K^+\pi^-) \tag{3.43}$$

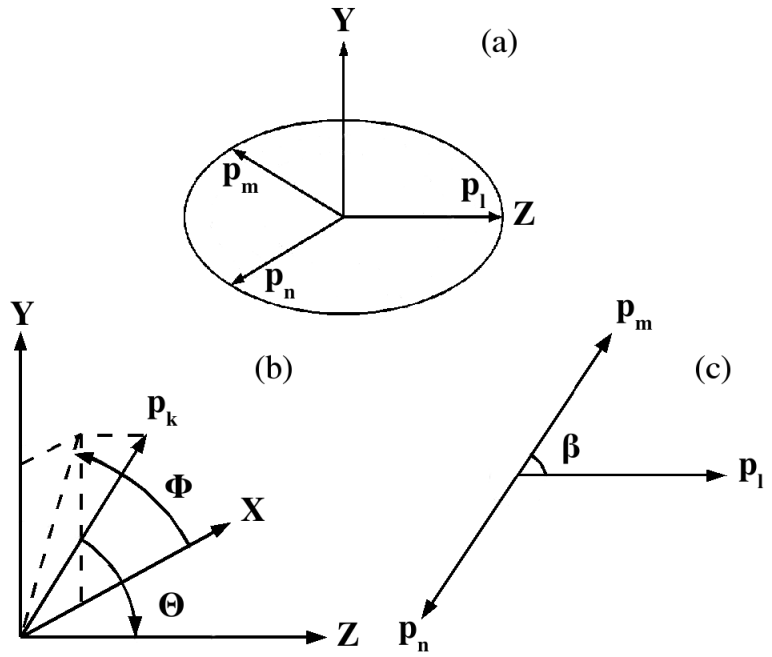

Figure 3.4: Reference frame for the angular distribution with an "l-type" isobar, as shown in [76]. For "n-type" and "m-type" isobars, the reference frame is obtained by means of a permutation of the indices.

where the numerical factors are SU(2) Clebsch-Gordan coefficients [5], while $BW(h^+h'^-)$ and $A_{S,P,D}$ are the normalized mass distribution and angular distribution, described in Sec. 3.5 and Sec. 3.5, respectively. These expressions can be compared to those in Appendix B of Ref. [93]. In the above expressions, the argument of the angular function specifies the permutation of the indices of the final state particles used in the definition of the reference frame relevant to each channel (Fig. 3.4). We point out that, in Eq. 3.41, the Clebsch-Gordan coefficient undergoes a change of sign under the interchange of the labels of the two pions, while $(\Theta, \Phi, \beta) \mapsto (\Theta, \pi + \Phi, \pi - \beta)$; the other equations, e.g., Eq. 3.40, are left unchanged.

For the other three-particles final states we obtain

$$\begin{aligned}
\langle K^0\pi^0\pi^+|1^+S(K^*\pi)\rangle &= \frac{1}{3}\left[A_S(\mathbf{p}_{\pi^+},\mathbf{p}_{K^0})BW_{\ell=0}(K^0\pi^0) - A_S(\mathbf{p}_{\pi^0},\mathbf{p}_{K^0})BW_{\ell=0}(K^0\pi^+)\right] \\
\langle K^0\pi^0\pi^+|1^+S(\rho K)\rangle &= \frac{1}{\sqrt{3}}A_S(\mathbf{p}_{K^0},\mathbf{p}_{\pi^+})BW_{\ell=0}(\pi^+\pi^0) \\
\langle K^0\pi^0\pi^+|1^+P(K_0^*\pi)\rangle &= \frac{1}{3}\left[A_P(\mathbf{p}_{\pi^+},\mathbf{p}_{K^0})BW_{\ell=1}(K^0\pi^0) - A_P(\mathbf{p}_{\pi^0},\mathbf{p}_{K^0})BW_{\ell=1}(K^0\pi^+)\right] \\
\langle K^0\pi^0\pi^+|1^+D(K^*\pi)\rangle &= \frac{1}{3}\left[A_D(\mathbf{p}_{\pi^+},\mathbf{p}_{K^0})BW_{\ell=2}(K^0\pi^0) - A_D(\mathbf{p}_{\pi^0},\mathbf{p}_{K^0})BW_{\ell=2}(K^0\pi^+)\right]
\end{aligned}$$

$$
\begin{aligned}
\langle K^+\pi_1^0\pi_2^0|1^+S(K^*\pi)\rangle &= \frac{1}{\sqrt{36}}\left[A_S(\mathbf{p}_{\pi_2^0},\mathbf{p}_{K^+})BW_{\ell=0}(K^+\pi_1^0)+A_S(\mathbf{p}_{\pi_1^0},\mathbf{p}_{K^+})BW_{\ell=0}(K^+\pi_2^0)\right]\\
\langle K^+\pi_1^0\pi_2^0|1^+S(\rho K)\rangle &= 0\\
\langle K^+\pi_1^0\pi_2^0|1^+P(K_0^*\pi)\rangle &= \frac{1}{\sqrt{36}}\left[A_P(\mathbf{p}_{\pi_2^0},\mathbf{p}_{K^+})BW_{\ell=1}(K^+\pi_1^0)+A_P(\mathbf{p}_{\pi_1^0},\mathbf{p}_{K^+})BW_{\ell=1}(K^+\pi_2^0)\right]\\
\langle K^+\pi_1^0\pi_2^0|1^+D(K^*\pi)\rangle &= \frac{1}{\sqrt{36}}\left[A_D(\mathbf{p}_{\pi_2^0},\mathbf{p}_{K^+})BW_{\ell=2}(K^+\pi_1^0)+A_D(\mathbf{p}_{\pi_1^0},\mathbf{p}_{K^+})BW_{\ell=2}(K^+\pi_2^0)\right]
\end{aligned}
$$

The same quantities relevant to the analysis of charged B decay modes are obtained in a straightforward way from the previous ones by taking the opposite hypercharge $Y=\frac{S}{2}$, i.e., by making the replacements $K^+\to\bar{K}^0$, $K^0\to K^-$:

$$
\begin{aligned}
\langle \overline{K}^0\pi^-\pi^+|1^+S(K^*\pi)\rangle &= \frac{\sqrt{2}}{3}A_S(\mathbf{p}_{\pi^+},\mathbf{p}_{\overline{K}^0})BW_{\ell=0}(\bar{K}^0\pi^-)\\
\langle \overline{K}^0\pi^-\pi^+|1^+S(\rho K)\rangle &= \frac{1}{\sqrt{6}}A_S(\mathbf{p}_{\overline{K}^0},\mathbf{p}_{\pi^+})BW_{\ell=0}(\pi^+\pi^-)\\
\langle \overline{K}^0\pi^-\pi^+|1^+P(K_0^*\pi)\rangle &= \frac{\sqrt{2}}{3}A_P(\mathbf{p}_{\pi^+},\mathbf{p}_{\overline{K}^0})BW_{\ell=1}(\bar{K}^0\pi^-)\\
\langle \overline{K}^0\pi^-\pi^+|1^+D(K^*\pi)\rangle &= \frac{\sqrt{2}}{3}A_D(\mathbf{p}_{\pi^+},\mathbf{p}_{\overline{K}^0})BW_{\ell=2}(\bar{K}^0\pi^-)
\end{aligned}
$$

$$
\begin{aligned}
\langle K^-\pi^0\pi^+|1^+S(K^*\pi)\rangle &= \frac{1}{3}\left[A_S(\mathbf{p}_{\pi^+},\mathbf{p}_{K^-})BW_{\ell=0}(K^-\pi^0)-A_S(\mathbf{p}_{\pi^0},\mathbf{p}_{K^-})BW_{\ell=0}(K^-\pi^+)\right]\\
\langle K^-\pi^0\pi^+|1^+S(\rho K)\rangle &= \frac{1}{\sqrt{3}}A_S(\mathbf{p}_{K^-},\mathbf{p}_{\pi^+})BW_{\ell=0}(\pi^+\pi^0)\\
\langle K^-\pi^0\pi^+|1^+P(K_0^*\pi)\rangle &= \frac{1}{3}\left[A_P(\mathbf{p}_{\pi^+},\mathbf{p}_{K^-})BW_{\ell=1}(K^-\pi^0)-A_P(\mathbf{p}_{\pi^0},\mathbf{p}_{K^-})BW_{\ell=1}(K^-\pi^+)\right]\\
\langle K^-\pi^0\pi^+|1^+D(K^*\pi)\rangle &= \frac{1}{3}\left[A_D(\mathbf{p}_{\pi^+},\mathbf{p}_{K^-})BW_{\ell=2}(K^-\pi^0)-A_D(\mathbf{p}_{\pi^0},\mathbf{p}_{K^-})BW_{\ell=2}(K^-\pi^+)\right]
\end{aligned}
$$

$$
\begin{aligned}
\langle \overline{K}^0\pi_1^0\pi_2^0|1^+S(K^*\pi)\rangle &= \frac{1}{\sqrt{36}}\left[A_S(\mathbf{p}_{\pi_2^0},\mathbf{p}_{\overline{K}^0})BW_{\ell=0}(\bar{K}^0\pi_1^0)+A_S(\mathbf{p}_{\pi_1^0},\mathbf{p}_{\overline{K}^0})BW_{\ell=0}(\bar{K}^0\pi_2^0)\right]\\
\langle \overline{K}^0\pi_1^0\pi_2^0|1^+S(\rho K)\rangle &= 0\\
\langle \overline{K}^0\pi_1^0\pi_2^0|1^+P(K_0^*\pi)\rangle &= \frac{1}{\sqrt{36}}\left[A_P(\mathbf{p}_{\pi_2^0},\mathbf{p}_{\overline{K}^0})BW_{\ell=1}(\bar{K}^0\pi_1^0)+A_P(\mathbf{p}_{\pi_1^0},\mathbf{p}_{\overline{K}^0})BW_{\ell=1}(\bar{K}^0\pi_2^0)\right]\\
\langle \overline{K}^0\pi_1^0\pi_2^0|1^+D(K^*\pi)\rangle &= \frac{1}{\sqrt{36}}\left[A_D(\mathbf{p}_{\pi_2^0},\mathbf{p}_{\overline{K}^0})BW_{\ell=2}(\bar{K}^0\pi_1^0)+A_D(\mathbf{p}_{\pi_1^0},\mathbf{p}_{\overline{K}^0})BW_{\ell=2}(\bar{K}^0\pi_2^0)\right]
\end{aligned}
$$

Contribution of the ωK channel

The contribution of the ωK channel is not included into the calculation of the $K\pi\pi$ Dalitz plot population [45], but it is taken into account when evaluating the overall efficiencies for the reconstruction of B decays, corrected for the branching fraction of the K_1 decay to the reconstructed final state.

The correction is calculated by first considering the production amplitude for the $K^+\pi^+\pi^-$ final state in the ρK channel. According to the above calculations, and omitting the angular dependence, we obtain

$$F_2\langle K^+\pi^-\pi^+|1^+S(\rho K)\rangle = F_2\frac{1}{\sqrt{6}}\frac{[m_\rho\Gamma_\rho(m)]^{1/2}}{\left(m_\rho^2-m^2\right)-im_\rho\Gamma_\rho(m)}. \tag{3.44}$$

The amplitude associated to the ωK channel is then given by:

$$F_6\langle K^+\pi^-\pi^+|1^+S(\omega K)\rangle = F_6\frac{1}{\sqrt{2}}\frac{\left[m_\omega\Gamma_\rho(m)\frac{\Gamma_{\omega\to 2\pi}}{m_\omega}\frac{m_\rho}{\Gamma_{\rho\to 2\pi}})\right]^{1/2}}{(m_\omega^2-m^2)-im_\omega\Gamma_\omega(m)}, \tag{3.45}$$

where we use the following values [5], expressed in MeV:

$$\begin{aligned}\Gamma_{\omega\to 2\pi} &= (14.4\pm 2.3)\times 10^{-2},\\ \Gamma_{\rho\to 2\pi} &= 146.4\end{aligned}$$

and the $\frac{1}{\sqrt{2}}$ factor arises because of the convention used [82, 93]. The contribution of the ωK channel is finally rescaled for the $\omega\to\pi^+\pi^-$ branching fraction, which is equal to $(1.70\pm 0.27)\%$.

3.6 Kinematics

The kinematics of the quasi-two-body decay $B\to h_4+P$, $P\to h_3+D$, $D\to h_1+h_2$, where the h_i's are pseudoscalar particles, can be expressed in terms of several Mandelstam-like variables. These are defined as:

$$\begin{aligned}s_i &\equiv (Q-p_i)^2,\\ t_{ij} &\equiv (Q-p_i-p_j)^2,\end{aligned}$$

where $Q=p_1+p_2+p_3+p_4$. Only five of these variables are independent.

The relevant quantities for the calculation of the amplitudes in Sec. 3.5 can be expressed as follows (the label P or D in parenthesis indicates that the quantity is evaluated in the rest frame of P or D, respectively):

$$\begin{aligned}E_{1(P)} &= \frac{m_B^2+2m_1^2+m_4^2-t_{23}-s_1}{2\sqrt{s_4}}\\ E_{2(P)} &= \frac{m_B^2+2m_2^2+m_4^2-t_{13}-s_2}{2\sqrt{s_4}}\\ E_{3(P)} &= \frac{m_B^2+2m_3^2+m_4^2-t_{12}-s_3}{2\sqrt{s_4}}\\ E_{4(P)} &= \frac{m_B^2-m_4^2-s_4}{2\sqrt{s_4}}\\ |\vec{p}_{i(P)}| &= \sqrt{E_{i(P)}^2-m_i^2}\end{aligned}$$

$$E_{1(D)} = \frac{t_{34} - m_2^2 + m_1^2}{2\sqrt{t_{34}}}$$
$$E_{3(D)} = \frac{s_4 - t_{34} - m_3^2}{2\sqrt{t_{34}}}$$
$$|\vec{p}_{i(D)}| = \sqrt{E_{i(D)}^2 - m_i^2}$$

$$\vec{p}_{3(P)} \cdot \vec{p}_{4(P)} = \frac{s_3 - m_B^2 - m_3^2}{2} + E_{3(P)}\left(\sqrt{s_4} + E_{4(P)}\right)$$
$$\vec{p}_{1(P)} \cdot \vec{p}_{3(P)} = \frac{m_1^2 + m_3^2 - t_{24}}{2} + E_{1(P)}E_{3(P)}$$
$$\vec{p}_{1(P)} \cdot \vec{p}_{4(P)} = \frac{s_1 - m_B^2 - m_1^2}{2} + E_{1(P)}\left(\sqrt{s_4} + E_{4(P)}\right)$$
$$\vec{p}_{1(D)} \cdot \vec{p}_{3(D)} = \frac{m_1^2 + m_3^2 - t_{24}}{2} + E_{1(D)}E_{3(D)}$$

$$\cos\Theta = \frac{\vec{p}_{3(P)}}{|\vec{p}_{3(P)}|} \cdot \frac{\vec{p}_{4(P)}}{|\vec{p}_{4(P)}|}$$
$$\cos\beta = \frac{\vec{p}_{1(D)}}{|\vec{p}_{1(D)}|} \cdot \frac{\vec{p}_{3(D)}}{|\vec{p}_{3(D)}|}$$
$$\cos\Phi = \frac{\vec{p}_{1(P)} - \left(\vec{p}_{1(P)} \cdot \hat{p}_{3(P)}\right)\hat{p}_{3(P)}}{\left|\vec{p}_{1(P)} - \left(\vec{p}_{1(P)} \cdot \hat{p}_{3(P)}\right)\hat{p}_{3(P)}\right|} \cdot \frac{\vec{p}_{4(P)} - \left(\vec{p}_{4(P)} \cdot \hat{p}_{3(P)}\right)\hat{p}_{3(P)}}{\left|\vec{p}_{4(P)} - \left(\vec{p}_{4(P)} \cdot \hat{p}_{3(P)}\right)\hat{p}_{3(P)}\right|}$$

3.7 Monte Carlo production

We have generated about 900 000 events using `EvtGen` [94] with a user defined module, which modulates the $K^+\pi^-\pi^+\pi^-$ phase space according to the amplitude A_{gen}:

$$\begin{aligned} |A_{\rm gen}|^2 \;=\; & |BW_{K_1}|^2 \cdot \left(0.24 \cdot |BW_{K^*}|^2 + 0.43 \cdot |BW_\rho|^2 + 0.20 \cdot |BW_{K_0^*}|^2\right) + \\ & |BW_{K_1'}|^2 \cdot \left(0.81 \cdot |BW_{K^*}|^2 + 0.13 \cdot |BW_\rho|^2\right), \end{aligned} \tag{3.46}$$

where:

$$BW_i = \frac{\sqrt{\Gamma_i}}{(m - m_i) + i\Gamma_i/2}. \tag{3.47}$$

Γ_i and m_i are the width and mean mass of the resonance i, respectively, and their value is set according to Table 3.2; m is the invariant mass of the resonant particles. The amplitude is not Bose-symmetrized: we estimate that the effect of neglecting Bose-symmetrization in signal MC is of order 0.5%, which corresponds to the fraction of events for which $s_2 > s_4$. The output of the `EvtGen` simulation is passed to the simulation of the full detector response.

The events generated with the simplified model described above are weighted in order to obtain the MC distributions associated to different values of the production terms. The

weight of each event is the ratio of the squared amplitude $A(\boldsymbol{\zeta})$ calculated as in Sec. 3.4.1 to the squared amplitude A_{gen} (3.46):

$$w(\boldsymbol{\zeta}) = \frac{|A(\boldsymbol{\zeta})|^2}{|A_{\text{gen}}|^2}. \tag{3.48}$$

The weights are calculated from generator level information. In Fig. 3.5 and Fig. 3.8, the obtained angular distributions in the reweighted datasets for different spin-parity configurations are compared to those obtained from the `EvtGen` built-in models in order to ensure that our custom implementation of reweighting is reliable and compatible with the results of the default simulation procedure.

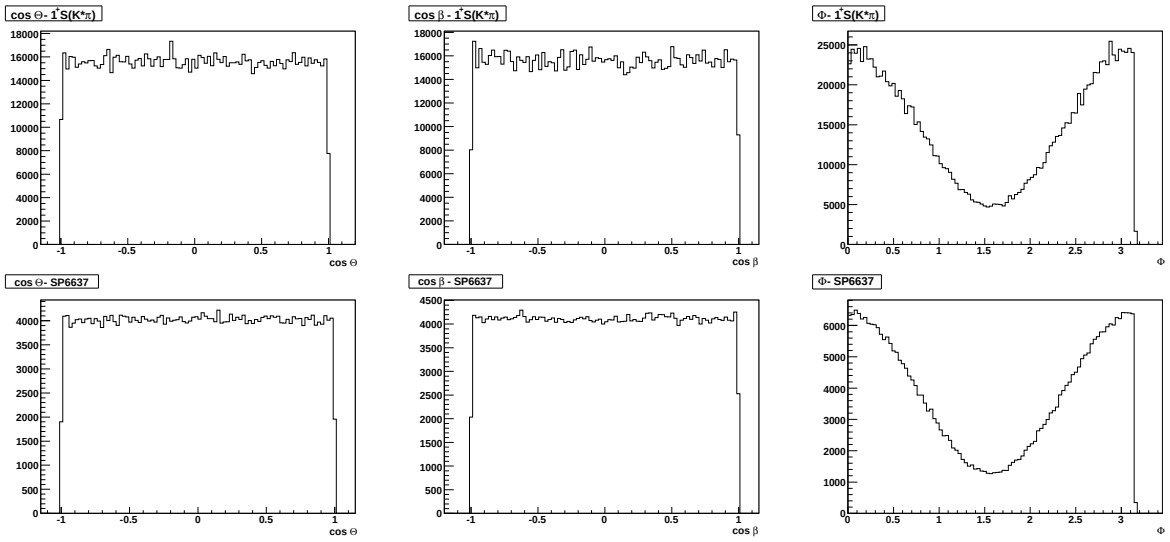

Figure 3.5: Angular distributions in reweighted (first row) and default (second row) MC samples ($(K^*\pi)_{S-wave}$ channel).

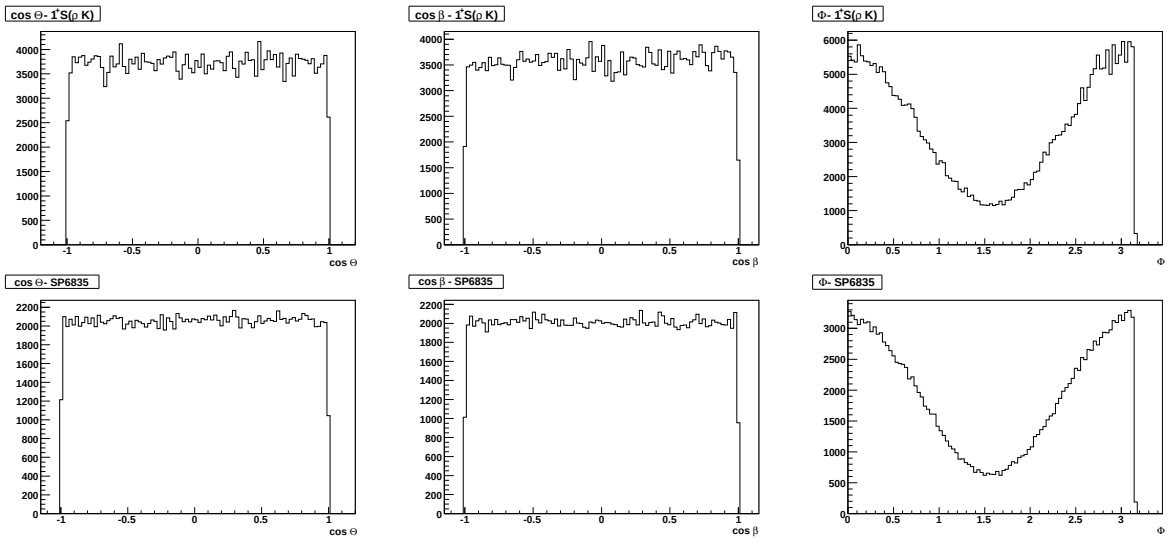

Figure 3.6: Angular distributions in reweighted (first row) and default (second row) MC samples (ρK channel).

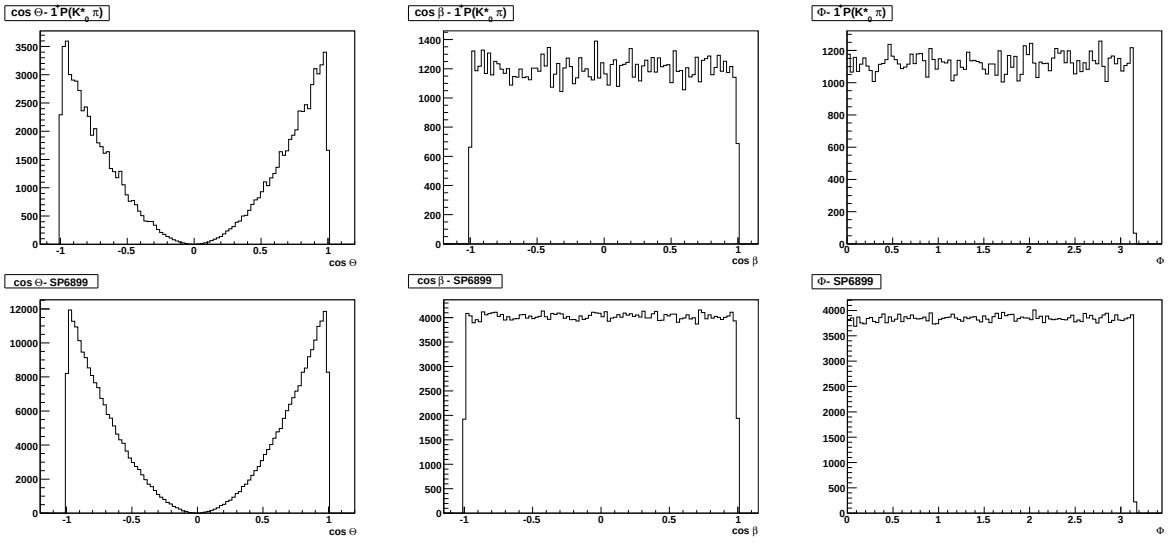

Figure 3.7: Angular distributions in reweighted (first row) and default (second row) MC samples ($(K_0^*\pi)$ channel).

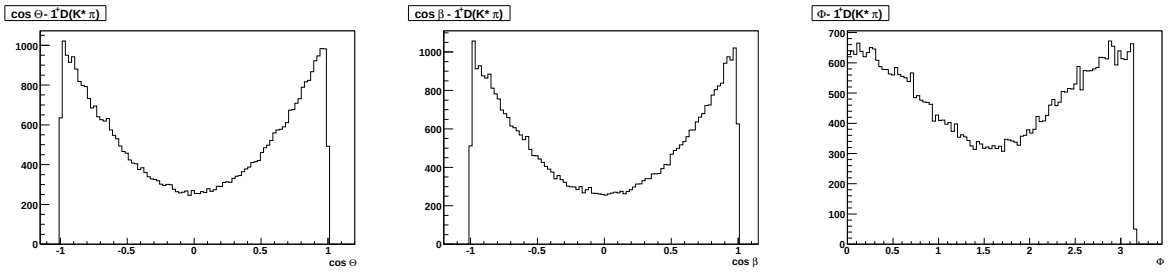

Figure 3.8: Angular distributions in reweighted MC sample ($(K^*\pi)_{D-wave}$ channels).

Chapter 4

Discriminating variables

4.1 Kinematical variables

The kinematics of $\Upsilon(4S) \to B\overline{B}$ decays is characterized by ΔE and $m_{\rm ES}$.These variables allow the separation between $B\overline{B}$ events and combinatorial background.

- $m_{\rm ES} = [(\frac{1}{2}s + \mathbf{p}_{\Upsilon(4S)} \cdot \mathbf{p}_B)^2/E^2_{\Upsilon(4S)} - \mathbf{p}^2_B]$ (*energy substituted mass*) corresponds to the mass of the B candidate calculated using the reconstructed momentum and the energy of the initial e^+e^- state, in the LAB frame.
- $\Delta E = E^*_B - \frac{1}{2}\sqrt{s}$ is defined as the difference between the energy of the B candidate and its expected value, calculated from the energy of the initial e^+e^- state, in the CM frame.

$m_{\rm ES}$ is related to the reconstructed momenta of the final state particles, while ΔE is related to the reconstructed energies. Because of this, ΔE depends on the mass hypothesis assigned to the final state particles, while $m_{\rm ES}$ does not.

The $m_{\rm ES}$ resolution is dominated by the beam energy fluctuations, while the ΔE resolution is dominated by the error on the measurement of the B energy. This is relevant to the choice of the control sample for the verification of the agreement between data and MC. In particular, the $m_{\rm ES}$ distribution of correctly reconstructed B decays is largely independent of the B decay mode, while for ΔE it is preferable to choose a control sample with a similar kinematics as the reconstructed signal B decay mode. The $B \to D\pi$ decay mode, with $D \to K\pi\pi$, therefore represents a good control sample; charmless decay modes to the same final state as the signal have similar ΔE and $m_{\rm ES}$ distributions, but are too rare to constitute a viable control sample.

4.2 Topological variables

Several topological variables can be defined, which are useful to distinguish between the jet-like structure of $e^+e^- \to q\overline{q}$ ($q = u, d, s, c$) events (the so-called continuum background), and the isotropic distribution of decay products in $B\overline{B}$ events (in the CM frame). These variables are here defined in terms of quantities (momenta and angles) measured in the CM frame. Two recurring concepts in their definitions are those of

- rest-of-event (ROE), i.e., the set of all detected tracks and photons in the event that have not been used to reconstruct the signal B candidate;

- the thrust (T) and thrust axis ($\vec{v}$) [95]: the thrust T is defined as

$$T = \max_{|\vec{n}|=1} \frac{\sum_i |\vec{n} \cdot \vec{p}_i|}{\sum_i |\vec{p}_i|}, \tag{4.1}$$

  where the sum runs over the detected particles. The thrust can be computed by summing over all tracks and photons in the event (T), or considering only objects belonging to the B decay tree (T_B) or to the ROE (T_{ROE}). The thrust axis $\vec{v}$ is given by the $\vec{n}$ vector for which the maximum of T is attained.

Here we list the topological variables that enter the analysis:

- $\cos\theta_{\mathrm{T}}$ is the cosine of the angle θ_T between the thrust axis of the B candidate and the thrust axis of the ROE, calculated in the CM frame. The $|\cos\theta_{\mathrm{T}}|$ variable has a nearly flat distribution for $B\overline{B}$ events while it is sharply peaked at +1 for continuum background events (Fig. 4.1).

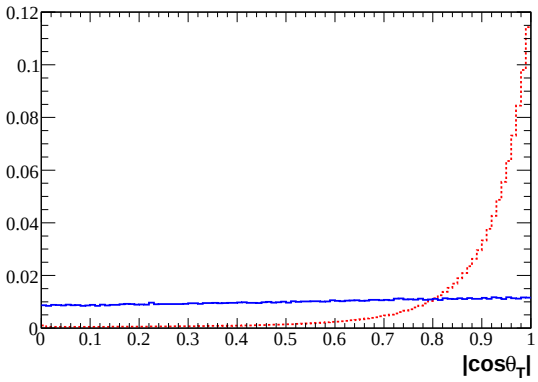

Figure 4.1: $|\cos\theta_T|$: comparison between Monte Carlo signal events (solid line) and off-peak data (dashed line).

- the Fisher discriminant $\mathcal{F} = \sum_i \alpha_i x_i$ is a statistical test, defined as a linear combination of several variables, where the α_i coefficients are chosen so that they maximize the separation between the $\mathcal{F}$ distributions in the signal and background hypotheses. The Fisher discriminant used in this analysis has the following form:

$$\mathcal{F} = 0.367 \cdot (1.60287 \cdot |\cos\theta_C| + 1.89495 \cdot |\cos\theta_B| - 0.66531 \cdot L_0 + 2.6685 \cdot L_2) - 1.3, \tag{4.2}$$

  where the coefficients are optimized on samples of MC signal events and off-peak data. The following variables enter the definition of $\mathcal{F}$: the absolute value of the cosine of the angle between the direction of the reconstructed B candidate and the beam axis ($|\cos\theta_B|$), the absolute value of the cosine of the angle between the thrust axis of the reconstructed B candidate and the beam axis ($|\cos\theta_C|$), and the two monomials L_0 and L_2, with

$$L_n = \sum_{i=ROE} p_i \times |\cos(\theta_i)|^n, \tag{4.3}$$

  where the sum runs over the reconstructed tracks and neutrals in the ROE, p_i is the momentum of particle i, and θ_i is the angle between the flight direction of particle i and the thrust axis of the B candidate. These variables are shown in Figure 4.2.

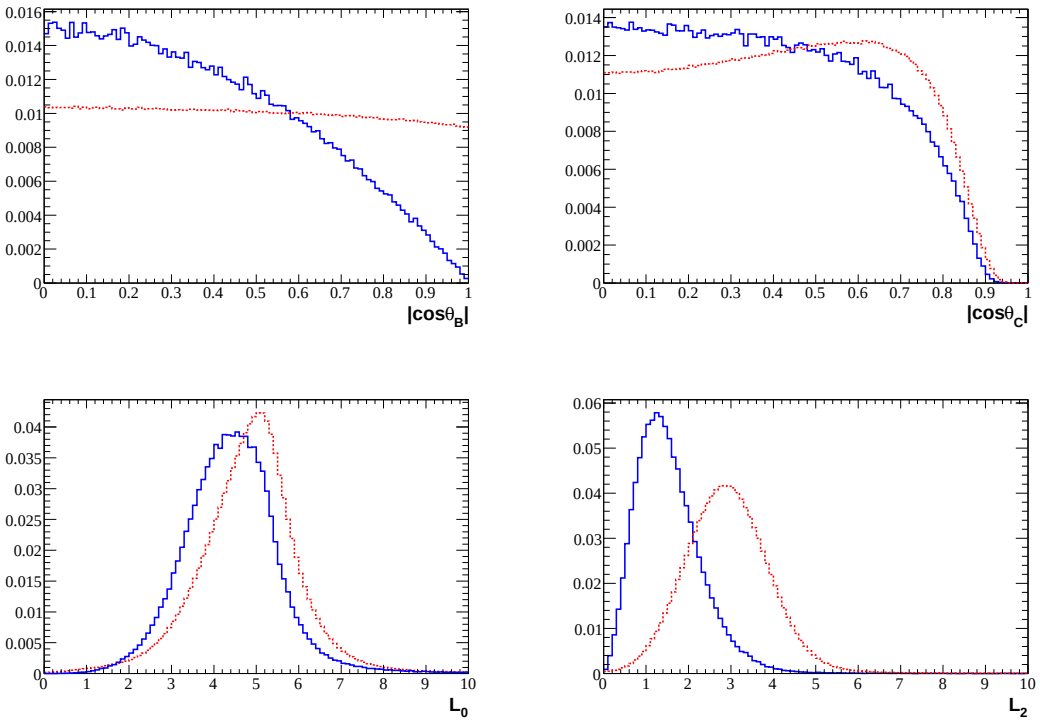

Figure 4.2: Variables used in the $\mathcal{F}$ calculated for $B\overline{B}$ MC signal events (solid line) and off-peak data (dashed line): $|\cos\theta_B|$, top left; $|\cos\theta_C|$, top right; L_0, bottom left; L_2, bottom left.

4.3 Characterization of the $K\pi\pi$ resonant structure

The invariant mass $m_{K\pi\pi}$ of the $K\pi\pi$ system and an angular variable $\mathcal{H}$ are used to characterize the resonant structure in the decay of the B candidate and distinguish the K_1 resonances from other $K\pi\pi$ resonances in the selected mass region. The $m_{K\pi\pi}$ variable, in particular, can also provide information on the parameters describing K_1 production.

The angular variable $\mathcal{H}$ is defined as the cosine of the angle α between the flight direction of the primary pion and the normal to the plane defined by the momenta of the K_1 candidate's daughters, evaluated in the rest frame of the K_1 candidate. This variable is particularly suited for the characterization of $B \to K_1\pi$, $K_1 \to K\pi\pi$ transitions, since it does not depend on the details of the $K_1 \to K\pi\pi$ decays.

The angular distributions for $B \to K_X\pi$ decays are calculated in the helicity formalism. In this way it is possible to check for possible inaccuracies in the simulation of the angular distributions in Monte Carlo samples. Tables 4.1 – 4.2 summarize the behavior of the angular distributions for $B \to K_X\pi$, $K_X \to K\pi\pi$ decays, which are assumed to proceed through a chain of quasi-two-body processes $B \to Ph_1$, $P \to Dh_2$, $D \to h_3h_4$, where h_1, h_2, h_3, h_4 are pseudo-scalar particles and several combinations of the D and P spin-parities are considered.

The calculation is performed for two sets of coordinates:

- the first choice of coordinates is $(\cos\Theta, \Psi)$, where Θ is the polar angle of the flight direction of h_1 from the flight direction of h_2, Ψ is the azimuthal angle of the flight direction of h_1 in the plane orthogonal to the flight direction of h_2, and both angles are evaluated in P rest frame;

$J^P(M)$	$J^P(D)$		$d\Gamma/(d\cos\Theta\ d\Psi\ d\cos\beta) \propto$
1^+	1^-	pure S-wave	$(\cos\Theta\cos\beta + \sin\Theta\cos\Psi\sin\beta)^2$
1^+	1^-	pure D-wave	$(-2\cos\Theta\cos\beta + \sin\Theta\cos\Psi\sin\beta)^2$
1^+	0^+		$\cos^2\Theta$
1^-	1^-		$\sin^2\Theta\sin^2\Psi\sin^2\beta$
2^+	1^-		$\cos^2\Theta\sin^2\Theta\sin^2\Psi\sin^2\beta$

Table 4.1: Angular distributions for $K_X(K\pi\pi)\pi$ decays (in terms of Θ, Ψ, β).

$J^P(M)$	$J^P(D)$		$d\Gamma/(d\cos\alpha\ d\gamma\ d\cos\beta) \propto$
1^+	1^-	pure S-wave	$\sin^2\alpha\ (-\cos\gamma\cos\beta - \sin\gamma\sin\beta)^2$
1^+	1^-	pure D-wave	$\sin^2\alpha\ (2\cos\gamma\cos\beta - \sin\gamma\sin\beta)^2$
1^+	0^+		$\sin^2\alpha\cos^2\gamma$
1^-	1^-		$\cos^2\alpha\sin^2\beta$
2^+	1^-		$\sin^2\alpha\cos^2\alpha\cos^2\gamma\sin^2\beta$

Table 4.2: Angular distributions for $K_X(K\pi\pi)\pi$ decays (in terms of α, γ, β).

- the second choice of coordinates is $(\cos\alpha, \gamma)$, where α is the polar angle of the flight direction of h_1 from the normal to the plane of M decay, γ is the azimuthal angle of the flight direction of h_1 in the plane of P decay, and both angles are evaluated in P rest frame.

In both sets, β is the angle between the flight direction of h_3 and the flight direction of particle h_2, calculated in D rest frame. The Jacobian for the change of variables from the first set of coordinates to the second one is $|J| = 1$.

The amplitudes for the $B \to K_1(K\pi\pi)\pi$ decays listed in Table 4.2, where K_1 is an axial vector meson, factorize in $\mathcal{M} \sim \sin\alpha\ f(\gamma, \mathbf{x}_D)$, where $\mathbf{x}_D$ indicates two variables which completely describe the $K\pi\pi$ Dalitz plot, given the $K\pi\pi$ invariant mass. Stated otherwise, the distribution of $\mathcal{H} \equiv \cos\alpha$ doesn't depend on the orbital angular momentum of the products of K_1 decays. Because of this, we assume that interference effects between the nearby K_1 resonances do not appreciably affect the signal distribution in this observable. A comparison between the $\mathcal{H}$ distributions for $J^P(M) = 1^+$ and $J^P(M) = 2^+$ Monte Carlo events is shown in Figure 4.3.

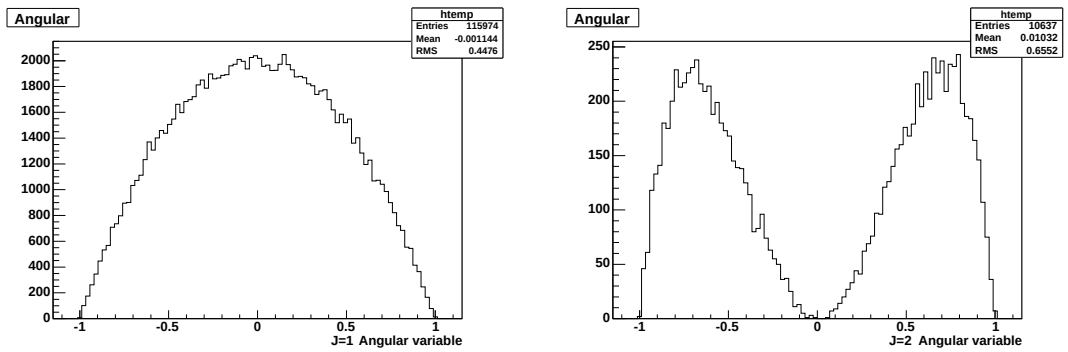

Figure 4.3: Angular variable shapes for $J^P(M) = 1^+$ (left) and $J^P(M) = 2^+$ (right) without the effects of detector acceptance and resolution.

Chapter 5

Analysis of B decays to $K_1(1270)\pi$ and $K_1(1400)\pi$

5.1 Data and Monte Carlo samples

The analysis presented in this thesis is based on the data sample recorded by *BABAR* in the period 1999-2006, corresponding to $(454.3 \pm 5.0) \times 10^6$ $B\overline{B}$ pairs and an integrated luminosity of 413 fb^{-1}. The uncertainty associated to the B counting, i.e., the measurement of the number of produced $\Upsilon(4S)$ mesons, is 1%.

In addition to the data collected at the $\Upsilon(4S)$ peak (on-resonance data, $\sqrt{s} = 10.58$ GeV), a reduced data sample of 41.2 fb^{-1} is collected about 40 MeV below the $\Upsilon(4S)$ peak (off-resonance data, $\sqrt{s} = 10.54$ GeV), and is used to study the $e^+e^- \to q\overline{q}$ background events.

The properties of background and signal events are studied on large samples of simulated Monte Carlo events before looking at the data, thus preventing the analyst from introducing artificial biases in the measurement. For the simulation of the production and decay of the $B\overline{B}$ pairs, the `EvtGen` package [94] is used. A GEANT4-based Monte Carlo simulation is used to model the response of the detector [74], taking into account the varying accelerator and detector conditions.

The production of inclusive $B\overline{B}$ Monte Carlo samples is centralized and consists of 702.8×10^6 $B^0\overline{B}^0$ events and 702.6×10^6 B^+B^- events, equivalent to about 3.1 times the on-resonance integrated luminosity. The branching fractions used in the simulation are taken from the experimental measurements (where available), or from theoretical estimates. Quark fragmentation is in general simulated with the JETSET generator [96].

In addition to generic $B\overline{B}$ samples, selected $B\overline{B}$ Monte Carlo samples are generated according to exclusive decay modes for both signal and background. The signal exclusive Monte Carlo samples are listed in Table 5.1, while the background samples will be studied in Sec. 5.3

In order to treat long decay chains efficiently, `EvtGen` allows the amplitude for each node in the decay chain to be written independently of the other nodes in the tree, while the framework handles the bookkeeping of amplitudes and spin density matrices [94]. As each node is simulated individually, this procedure cannot account for interference effects between two decay chains.

To simulate the effects of interference, we generate samples of about 900 000 events each for the decay sequences $B^0 \to K_1(1400)^+\pi^-$, $K_1(1400)^+ \to K^+\pi^+\pi^-$, and $B^+ \to K_1(1400)^0\pi^+$, $K_1(1400)^0 \to K^0_S\pi^+\pi^-$, with $K^0_S \to \pi^+\pi^-$. The kinematics of the whole

decay chain is generated, and each generated event is reweighted according to the total decay amplitude as described in Sec. 3.7.

Decay chain	Events
$\overline{B}^0 \to X$, $B^0 \to K_1(1400)^+\pi^-$, $K_1(1400)^+ \to K^{*0}\pi^+$, $K^{*0} \to K^+\pi^-$	350 000
$\overline{B}^0 \to X$, $B^0 \to K_1(1270)^+\pi^-$, $K_1(1400)^+ \to K^+\rho^0$, $\rho^0 \to \pi^+\pi^-$	175 000
$B^- \to X$, $B^+ \to K_1(1400)^0\pi^+$, $K_1(1400)^0 \to K^{*+}\pi^-$, $K^{*+} \to K^0_S\pi^+$, $K^0_S \to \pi^+\pi^-$	387 000
$B^- \to X$, $B^+ \to K_1(1270)^0\pi^+$, $K_1(1400)^0 \to K^0_S\rho^0$, $\rho^0 \to \pi^+\pi^-$, $K^0_S \to \pi^+\pi^-$	387 000

Table 5.1: Exclusive signal Monte Carlo samples used for the analysis.

5.2 Reconstruction of the decay chain

The $B^0 \to K_1^+\pi^-$, $K_1^+ \to K^+\pi^+\pi^-$ decay chain is reconstructed by means of a vertex fit of all combinations of four charged tracks having a zero net charge. Similarly we reconstruct the $B^+ \to K_1^0\pi^+$, $K_1^0 \to K_S^0\pi^+\pi^-$ chain by combining a K_S^0 candidate with three charged tracks.

5.2.1 Charged tracks reconstruction

Charged particle tracks are reconstructed from the spatial hits in the SVT and the DCH: an iterative fitting algorithm based on the Kalman filter technique performs pattern recognition and determines for each track the five parameters of the helix described by a charged particle in the magnetic field of *BABAR*'s solenoid. The full map of the magnetic field, the detailed distribution of the material in the detector and the expected energy loss of the particle as it traverses the detector are taken into account.

In order to improve the accuracy in the determination of the event shape variables, we require a minimum of 5 tracks in each event.

With the exception of the pions from K_S^0 decays, the charged pions and kaons produced in $B \to K_1\pi$ decays are expected to originate from the e^+e^- interaction region: we therefore require that the distance of the point of closest approach of the track to the interaction point be less than 1.5 cm in the XY plane (transverse to the magnetic field) and less than 2.5 cm along Z (parallel to the magnetic field). Each track used in the reconstruction of the $B \to K_1\pi$ decay chain is furthermore required to have a transverse momentum $p_t > 50$ MeV/c and a momentum $|\mathbf{p}| < 10$ GeV/c.

5.2.2 Charged tracks identification

The charged particles used for reconstructing the B candidate are identified as either pions or kaons, and must not be consistent with the electron, muon or proton hypotheses. The K_S^0 daughters are not subject to particle identification (PID) requirements.

The $\pi/K/p$ separation is achieved by likelihood-based classifiers calculated from the specific ionization loss dE/dx measured in the SVT and in the DCH, the Cerenkov angle θ_C, and the number N_γ of Cerenkov photons reconstructed in the DIRC. The particle ID information from each of the three subdetectors is used to calculate a likelihood, for a given particle hypothesis. A subsystem provides particle information for a charged track only if

a number of minimal requirements are satisfied. The global likelihood for a given particle hypothesis is thus given by the product of the likelihoods of the subsystems that pass the requirements for that track.

Muon candidates are primarily identified by: the measured number of hadronic interaction lengths traversed from the outside radius of the DCH through the IFR iron, and its difference with respect to the predicted penetration depth for a muon of the same momentum and angle; the average number and the variance of hits per IFR layer; the χ^2 for the geometric match between the track extrapolation into the IFR and the IFR hits, the χ^2 of a polynomial fit to the IFR hits; the continuity of the tracks in the IFR, and the energy release in the electromagnetic calorimeter. This information is passed as input to a neural network.

In *BABAR* several "PID selectors" for each particle specie are defined, that correspond to different sets of cuts on the likelihood ratios for the $\pi/K/p$ discrimination or on the output of the neural network for the muon identification, and result in different selection efficiencies and mis-identification rates. In order to retain a high selection efficiency, we identify charged pions by vetoing the alternative hypotheses, i.e., the kaon, electron, proton, and muon hypotheses. Similarly, we identify charged kaons by vetoing the pion, electron, proton, and muon hypotheses.

5.2.3 Composite candidates reconstruction

K_s^0 candidates

The K_S^0 candidates are reconstructed from pairs of oppositely-charged pions with an invariant mass in the range $[486, 510]$ MeV/c^2, whose decay vertex is required to be displaced from the K_1 vertex by at least 3 standard deviations. A χ^2 probability greater than 0.001 is required.

K_1 candidates

For the B^0 modes we reconstruct the K_1 candidate in the $K_1^+ \to K^+\pi^+\pi^-$ decay by combining three tracks, identified as two charged pions and one charged kaon. For the B^+ modes we reconstruct the K_1 candidate in the $K_1^0 \to K_S^0\pi^+\pi^-$ decay by combining two charged pions with a K_S^0 candidate. We require the reconstructed mass $m_{K\pi\pi}$ to lie in the range $[1.1, 1.8]$ GeV/c^2, and the K_1 momentum in the center of mass frame to be in the range $[2.30, 2.65]$ GeV/c. To reduce background from $B \to V\pi$ decay modes, where V is a vector meson decaying to $K\pi\pi$ such as $K^*(1410)$ or $K^*(1680)$, we require $|\mathcal{H}| < 0.95$.

B candidates

B mesons are reconstructed by combining a K_1 candidate with a charged pion ("primary" or "prompt") with a center of mass momentum $p_{CMS} \geq 1.35$ GeV/c. The prompt track and the K_1 candidate are constrained to originate from a common vertex.

We reduce fake B candidates from $q\overline{q}$ events by requiring $|\cos\theta_{\rm T}| < 0.8$. A loose selection is applied on the observables entering the fit: $5.25 < m_{\rm ES} < 5.29$ GeV/c^2, $|\Delta E| < 0.15$ GeV, and $-3 < \mathcal{F} < 3$. Background from B decays to final states containing charm or charmonium mesons is suppressed by means of vetoes.

5.2.4 Charm vetoes

A B-meson candidate is rejected if it shares at least one track with a background B candidate reconstructed in the $B^0 \to D^-\pi^+$, $B^0 \to D^{*-}\pi^+$, $B^+ \to \bar{D}^0\pi^+$, or $B^+ \to \bar{D}^{*0}\pi^+$ decay modes, and satisfying $5.27 < m_{\rm ES} < 5.29$ GeV/c^2 and $-0.15 < \Delta E < 0.15$ GeV. The D mesons are reconstructed in the $K\pi$, $K\pi\pi$, and $K\pi\pi\pi$ decays, with at most one neutral pion in the final state and an invariant mass $1.800 < m_D < 1.940$ GeV/c^2. The D^* meson is reconstructed by combining a D meson with a charged or neutral pion, or a photon. For each background decay mode and for each signal B candidate, we select, among the background B candidates that share at least one track with the signal B candidate, the candidate with the highest B-vertex fit probability.

To avoid excessively deteriorating the signal efficiency for the $B^+ \to K_1^0\pi^+$ mode, we apply the veto in this channel only if the reconstructed neutral (charged) D mesons further satisfy $1.836 < m_{D^0} < 1.892$ GeV/c^2 ($1.841 < m_{D^+} < 1.897$ GeV/c^2).

5.2.5 Charmonium vetoes

A signal candidate is also discarded if any $\pi^+\pi^-$ combination consisting of the "primary" pion from the B decay together with an oppositely charged pion from the K_1 decay has an invariant mass $m_{\pi\pi}$ consistent with the $c\overline{c}$ mesons $\chi_{c0}(1P)$ or $\chi_{c1}(1P)$ decaying to a pair of oppositely charged pions, or J/ψ and $\psi(2S)$ decaying to muons (where the muons are misidentified as pions). We reject the signal candidates for which $m_{\pi\pi}$ is in one of the following ranges:

- J/ψ: $3.040 < m_{\pi\pi} < 3.150$ GeV/c^2;
- $\psi(2S)$: $3.670 < m_{\pi\pi} < 3.695$ GeV/c^2;
- χ_{c0}: $3.375 < m_{\pi\pi} < 3.455$ GeV/c^2;
- χ_{c1}: $3.480 < m_{\pi\pi} < 3.540$ GeV/c^2.

5.2.6 Best-candidate selection

When reconstructing B candidates, it is possible that, in the same event, more than one combination of reconstructed particles satisfy the selection criteria. The average number of candidates in events containing at least one candidate is 1.2 for both the $B^0 \to K_1^+\pi^-$ and $B^+ \to K_1^0\pi^+$ modes, as evaluated in on-resonance data. In events with multiple candidates, we select the candidate with the highest χ^2 probability of the B vertex fit.

For Monte Carlo signal events, or simulated events with similar topologies, it is possible to classify the reconstructed B candidates in two classes:

- *Truth Matching (TM) candidates*: the reconstructed decay tree can be completely associated to the generated particle content and the simulated topology;
- *Self Cross Feed (SCF) candidates*: at least one of the final state particles from which the B candidate is reconstructed cannot be matched to any of the particles from the decay of the simulated B meson.

The rate at which the best-candidate selection algorithm selects a TM candidate, whenever present, over a SCF candidate characterizes its performances. Due to the specific kinematics of multicandidate events, this rate depends on the location of the event in the four-particle phase space. On average, this rate ranges between 85% and 90%, as evaluated on the Monte Carlo signal samples.

5.2.7 Classification of the events on the $K_1 \to K\pi\pi$ Dalitz plot

After the best-candidate selection, we classify the events in mutually exclusive categories according to the invariant masses of the $\pi\pi$ and $K\pi$ systems in the reconstructed decays of the K_1 mesons.

The events that satisfy the requirement $0.846 < m_{K\pi} < 0.946$ GeV/c^2 belong to class 1 ("K^* band": the range has been calculated from the full width of the K^* mesons, $\Gamma \sim 50$ MeV, and is centered on the mass of the K^{*0} meson); events not included in class 1 for which $0.500 < m_{\pi\pi} < 0.800$ GeV/c^2 belong to class 2 ("ρ band"); all other events are rejected.

This classification is based on the experimental prejudice, based on the literature, that the $K_1(1400)$ decays predominantly through the $K^*\pi$ channel, while the ρK channel is dominant in $K_1(1270)$ decays.

5.2.8 Efficiency

The signal reconstruction and selection efficiencies are obtained from the reweighted signal Monte Carlo samples described in Sec. 3.7.

A "raw efficiency" ϵ can be calculated as ratio of the number of TM candidates surviving all cuts, including the best-candidate selection, over the number of generated events. For a weighted Monte Carlo sample, the reconstruction and selection efficiency is calculated as $\epsilon = \sum_i w_i\chi_i / \sum_i w_i$, where the index i runs over the generated events, w_i is the weight associated to the i^{th} event, and χ is a characteristic function such that $\chi_i = 1$ if a TM candidate survives the selection for that event and $\chi_i = 0$ otherwise. Likewise, the error on ϵ is given by $\Delta\epsilon/\epsilon = \left(\sum_i w_i^2\chi_i\right)^{1/2} / \sum_i w_i\chi_i$. A procedure similar to the one described above can be applied to other counting problems with weighted Monte Carlo samples, by a suitable redefinition of the characteristic function χ.

The signal reconstruction and selection efficiencies depend on the assumed production parameters $\boldsymbol{\zeta}$. For B^0 modes these efficiencies range from 5 to 12% and from 3 to 8% for events in class 1 and class 2, respectively. For B^+ modes the corresponding values are 4-9% and 2-7%. The fractions of selected signal events in class 1 and class 2 range from 33% to 73% and from 16% to 49%, respectively, depending on the production parameters $\boldsymbol{\zeta}$. About 11% to 19% of the signal events are rejected at this stage. For combinatorial background, the fractions of selected events in class 1 and class 2 are 22% and 39%, respectively, while 39% of the events are rejected. In Fig. 5.1 we show the efficiency for TM events corrected for the branching fraction $\mathcal{B}(K_1^{(\prime)} \to K^+\pi^-\pi^+)$ as a function of ϑ and ϕ. The fraction of SCF candidates in the selected samples after the best-candidate selection depends only slightly on ϑ and ϕ and corresponds to 25% and 20% of TM events for B^0 and B^+ modes, respectively.

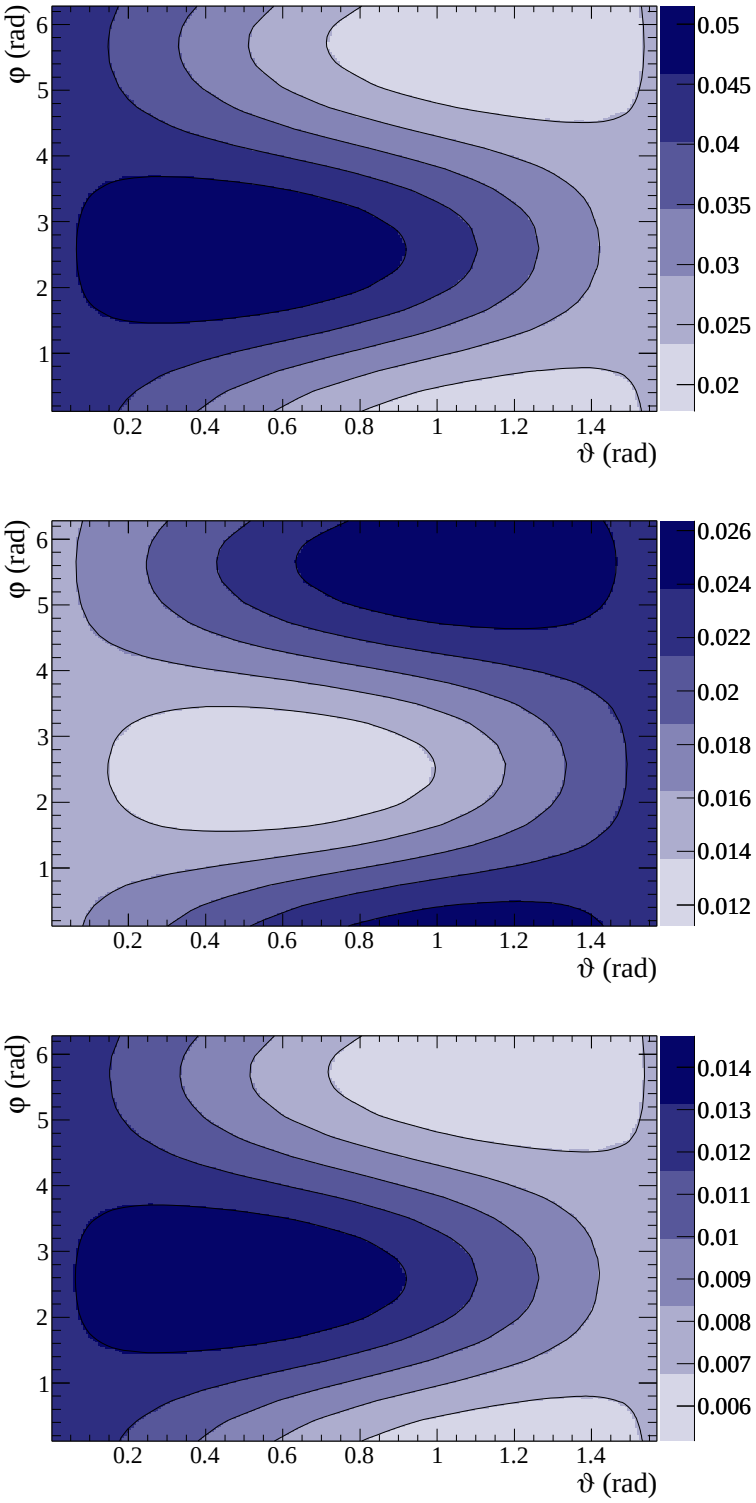

Figure 5.1: Efficiency for TM events, corrected for the $K_1 \to K\pi\pi$ branching fractions, as a function of the production parameters $\boldsymbol{\zeta}$. Top: B^0, "class 1" events; middle: B^0, "class 2" events; bottom: B^+, "class 1" events.

5.3 $B\overline{B}$ backgrounds

The $B\overline{B}$ background is first studied in inclusive generic $B^0\overline{B}^0$ and B^+B^- samples. The size of these samples is 3.1 times the on-resonance integrated luminosity. The available statistics is therefore not sufficient to perform detailed studies of the distributions in several observables, or to allow a sufficient number of independent toy samples to be be embedded into simulated experiments (Sec. 5.6). Moreover, the normalization of charmless background in generic $B\overline{B}$ Monte Carlo samples is not fully reliable: more precisely, the nonresonant multiparticle components generated with the JETSET fragmentation algorithm are generally overestimated, and double counting of some decays has been observed in the past.

Nevertheless, it is possible to use these samples to identify the background decay channels that are most likely to enter the selected sample. These are then studied in more detail using $B\overline{B}$ MC samples generated according to exclusive decay modes. In particular, we evaluate the reconstruction efficiency and the number of expected candidates in the on-resonance data sample.

Because of charge conservation, B^+B^- events, when reconstructed according to the B^0 decay tree, result in SCF candidates for a total of ~ 470 and ~ 1160 candidates in class 1 and class 2, respectively (normalized to the on-resonance integrated luminosity). Similarly, the $B^0\overline{B}^0$ events, when reconstructed as B^+B^- events, result in SCF candidates for a total of ~ 540 and ~ 980 candidates in class 1 and class 2, respectively. These SCF modes don't exhibit any peaking structure.

Background B decays to open charm final states are studied separately from charmless $B\overline{B}$ background channels, by reconstructing Monte Carlo cocktails consisting of several exclusive decay modes with a D or D^* meson in the final state. Since the $m_{K\pi\pi}$ selection window excludes the D region, most of the charm background is due to combinatorial background or to the lower tail of the D mass distribution. In the B^0 modes, the reconstruction efficiency for D mesons is further suppressed by the fact that the pions in the resonant $K\pi\pi$ system are opposite in charge when produced in K_1 decays, while they have the same charge if they come from the fragmentation of a D. Most reconstructed B decays to charm are therefore combinatorial and have a behavior similar to that of continuum.

Finally, several rare charmless B decays result in the same $K\pi\pi\pi$ final state as signal, or to a $\pi\pi\pi\pi$ final state in which a kaon is misidentified as a kaon. Among the charmless B decays to $K\pi\pi\pi$, the non-resonant decay modes are considered collectively as one single component, while each peaking background is taken into account separately.

Tables 5.2 and 5.3 report the results of the $B\overline{B}$ studies for the B^0 and B^+ modes, respectively. The tables report only the most relevant cross feed modes, which are expected to result in a nonnegligible background, grouped according to similarities in the distributions in ΔE, m_{ES}, $m_{K\pi\pi}$. The branching fractions of the studied background $B\overline{B}$ modes are taken from HFAG [8] and PDG tables [5]. When no BF measurement is available we assume a reasonable BF. For the $B \to K^*(1410)\pi$ modes we assume half the value of the ULs quoted in [8] for the $B \to K^*(1680)\pi$ decays.

Cross Feed Channel	MC ϵ (%)	$\mathcal{B}$ (10^{-6})	$\prod \mathcal{B}_i$	# evts
Class 1 candidates				
$B^0 \to a_1^{\pm} K^{\mp}$, $a_1^+ \to \rho^0\pi^+$	0.138	16.3 ± 3.7	0.5	5.1 ± 1.2
$B^0 \to D^-\pi^+$, $D^- \to K^-\pi^+\pi^-$	0.017	2680 ± 130	0.09	18.6 ± 0.9
$B^0 \to a_1^{\pm}\pi^{\mp}$, $a_1^+ \to \rho^0\pi^+$	0.612	31.7 ± 3.7	0.49	43.2 ± 5.0
$B^0 \to a_2^{\pm}\pi^{\mp}$, $a_2^+ \to \rho^0\pi^+$	0.730	$3 \pm 3*$	0.35	3.5 ± 3.5
$B^0 \to \pi^+\pi^+\pi^-\pi^-$	0.041	$10 \pm 10*$	1	1.9 ± 1.9
$B^0 \to K^{*0}\pi^+\pi^-$, $K^{*0} \to K^+\pi^-$	1.286	$5 \pm 5*$	0.67	19.5 ± 19.5
$B^0 \to \rho^0 K^+\pi^-$, $\rho^0 \to \pi^+\pi^-$	0.240	$10 \pm 10*$	1	10.8 ± 10.8
$B^0 \to \rho^0 K^{*0}$, $K^{*0} \to K^+\pi^-$, ln	2.577	2.8 ± 0.8	0.67	22.0 ± 6.3
$B^0 \to f_0 K^{*0}$, $K^{*0} \to K^+\pi^-$, $f_0 \to \pi^+\pi^-$	1.202	$2.1 \pm 2.1*$	0.44	5.0 ± 5.0
$B^0 \to K^+\pi^+\pi^-\pi^-$	0.108	$10 \pm 10*$	1	4.9 ± 4.9
$B^0 \to K^{*\pm}(1410)\pi^{\mp}$, $K^{*+}(1410) \to K^{*0}\pi^+$ (TM)	11.4	$5 \pm 5*$	0.39	100.9 ± 100.9
$B^0 \to K_2^{*\pm}(1430)\pi^{\mp}$, $K_2^{*+}(1430) \to K^{*0}\pi^+$ (TM)	14.0	$3.2 \pm 3.2*$	0.11	22.4 ± 22.4
$B^0 \to K_2^{*\pm}(1430)\pi^{\mp}$, $K_2^{*+}(1430) \to \rho^0 K^+$ (TM)	4.6	$3.2 \pm 3.2*$	0.03	1.9 ± 1.9
$B^0 \to K^{*\pm}(1680)\pi^{\mp}$, $K^{*+}(1680) \to K^{*0}\pi^+$ (TM)	5.7	$5.0 \pm 5.0*$	0.14	18.1 ± 18.1
$B^0 \to K^{*\pm}(1680)\pi^{\mp}$, $K^{*+}(1680) \to \rho^0 K^+$ (TM)	1.3	$5.0 \pm 5.0*$	0.10	3.0 ± 3.0
$B^0 \to K_1^{\pm}(1270)\pi^{\mp}$, $K_1^+(1270) \to \omega K^+$ (TM)	0.01	$28 \pm 28*$	0.11	0.1 ± 0.1
Class 2 candidates				
$B^0 \to a_1^{\pm} K^{\mp}$, $a_1^+ \to \rho^0\pi^+$	0.223	16.3 ± 3.7	0.5	8.3 ± 1.9
$B^0 \to D^-\pi^+$, $D^- \to K^-\pi^+\pi^-$	0.035	2680 ± 130	0.09	38.2 ± 1.8
$B^0 \to a_1^{\pm}\pi^{\mp}$, $a_1^+ \to \rho^0\pi^+$	1.039	31.7 ± 3.7	0.49	73.4 ± 8.5
$B^0 \to a_2^{\pm}\pi^{\mp}$, $a_2^+ \to \rho^0\pi^+$	1.362	$3 \pm 3*$	0.35	6.5 ± 6.5
$B^0 \to \pi^+\pi^+\pi^-\pi^-$	0.104	$10 \pm 10*$	1	4.7 ± 4.7
$B^0 \to \rho^0 K^+\pi^-$, $\rho^0 \to \pi^+\pi^-$	0.771	$10 \pm 10*$	1	34.9 ± 34.9
$B^0 \to K^{*0}\pi^+\pi^-$, $K^{*0} \to K^+\pi^-$	0.323	$5 \pm 5*$		4.9 ± 4.9
$B^0 \to \rho^0 K^{*0}$, $K^{*0} \to K^+\pi^-$, ln	0.405	2.8 ± 0.8	0.67	2.8 ± 0.8
$B^0 \to f_0 K^{*0}$, $K^{*0} \to K^+\pi^-$, $f_0 \to \pi^+\pi^-$	0.204	$2.1 \pm 2.1*$	0.44	0.9 ± 0.9
$B^0 \to K^+\pi^+\pi^-\pi^-$	0.257	$10 \pm 10*$	1	11.7 ± 11.7
$B^0 \to K^{*\pm}(1410)\pi^{\mp}$, $K^{*+}(1410) \to K^{*0}\pi^+$ (TM)	2.4 (3.3)	$5 \pm 5*$	0.39	21.3 ± 21.3
$B^0 \to K_2^{*\pm}(1430)\pi^{\mp}$, $K_2^{*+}(1430) \to K^{*0}\pi^+$ (TM)	2.8 (3.8)	$3.2 \pm 3.2*$	0.11	4.4 ± 4.4
$B^0 \to K_2^{*\pm}(1430)\pi^{\mp}$, $K_2^{*+}(1430) \to \rho^0 K^+$ (TM)	12.0 (13.6)	$3.2 \pm 3.2*$	0.03	5.1 ± 5.1
$B^0 \to K^{*\pm}(1680)\pi^{\mp}$, $K^{*+}(1680) \to K^{*0}\pi^+$ (TM)	1.0(1.5)	$5.0 \pm 5.0*$	0.14	3.1 ± 3.1
$B^0 \to K^{*\pm}(1680)\pi^{\mp}$, $K^{*+}(1680) \to \rho^0 K^+$ (TM)	3.9(4.6)	$5.0 \pm 5.0*$	0.10	8.8 ± 8.8
$B^0 \to K_1^{\pm}(1270)\pi^{\mp}$, $K_1^+(1270) \to \omega K^+$ (TM)	0.03 (0.35)	$28 \pm 28*$	0.11	0.3 ± 0.3

Table 5.2: Potential $B\overline{B}$ background to $B^0 \to K_1^+\pi^-$ modes for events in class 1 (top) and class 2 (bottom). For each decay mode we give the mode number, MC reconstruction efficiency ϵ, branching fraction ($\mathcal{B}$) [5,8,98], daughter branching fraction product, estimated background in ML input. The branching fractions marked with a $*$ are assumptions. PDFs will be modeled upon a MC sample of the first decay mode listed for each category.

Cross Feed Channel	MC ϵ (%)	$\mathcal{B}$ (10^{-6})	$\prod \mathcal{B}_i$	# evts
Class 1 candidates				
$B^+ \to \rho^0 K^{*+}$, $K^{*+} \to K^0_S \pi^+$	2.795	3.6 ± 1.9	0.23	10.5 ± 5.6
$B^+ \to K^{*+}\pi^-\pi^+$, $K^{*+} \to K^0_S \pi^+$ (TM)	0.934	$10 \pm 10*$	0.23	9.8 ± 9.8
$B^+ \to \rho^0 K^0_S \pi^+$ (TM)	0.149	$10 \pm 10*$	0.346	2.3 ± 2.3
$B^+ \to K^{*+} f^0$, $K^{*+} \to K^0_S \pi^+$, $f^0 \to \pi^+\pi^-$	1.315	5.2 ± 1.3	0.23	7.2 ± 1.8
$\overline{B^0} \to a_1^+ \pi^-$	0.0428	33 ± 5	1	6.41 ± 0.97
$B^+ \to a_1^0 \pi^+$, $a_1^0 \to \rho^\pm \pi^\mp$	0.020	20.4 ± 5.8	1	1.8 ± 0.5
$B^+ \to a_1^\pm K^0_S$, $a_1^\pm \to \rho^0 \pi^+$	0.346	34.9 ± 6.7	0.346	3.0 ± 0.6
$B^+ \to K_0^{*0} \pi^+$, $K_0^{*0} \to K^+ \pi^-$	0.003	45.2 ± 6.3	0.62	0.4 ± 0.1
$\overline{B^0} \to D^{(*)0} \pi^+$ cocktail	0.010	2490 ± 150	1.000	113.0 ± 6.8
$\overline{B^0} \to D^{(*)+} X$ cocktail	0.0033	4500 ± 500	1.000	67.4 ± 7.5
$B^+ \to K^{*0}(1410)\pi^+$, $K^{*0}(1410) \to K^{*+}\pi^-$ (TM)	9.467	$5 \pm 5*$	0.133	28.6 ± 28.6
$B^+ \to K^{*0}(1410)\pi^+$, $K^{*0}(1410) \to \rho^0 K^0_S$ (TM)	3.280	$5 \pm 5*$	0.008	0.6 ± 0.6
$B^+ \to K_2^{*0}(1430)\pi^+$, $K_2^{*0}(1430) \to K^{*+}\pi^-$ (TM)	11.578	5.6 ± 2.2	0.038	11.2 ± 4.4
$B^+ \to K_2^{*0}(1430)\pi^+$, $K_2^{*0}(1430) \to \rho^0 K^0_S$ (TM)	3.665	5.6 ± 2.2	0.010	0.9 ± 0.4
$B^0 \to K^{*0}(1680)\pi^+$, $K^{*0}(1680) \to K^{*+}\pi^-$ (TM)	5.432	$6.0 \pm 6.0*$	0.046	6.8 ± 6.8
$B^0 \to K^{*0}(1680)\pi^+$, $K^{*0}(1680) \to \rho^0 K^0_S$ (TM)	1.105	$6.0 \pm 6.0*$	0.036	1.1 ± 1.1
Class 2 candidates				
$B^+ \to \rho^0 K^{*+}$, $K^{*+} \to K^0_S \pi^+$	0.896	3.6 ± 1.9	0.23	3.4 ± 1.8
$B^+ \to \rho^0 K^0_S \pi^+$ (TM)	0.562	$10 \pm 10*$	0.345	8.8 ± 8.8
$B^+ \to K^{*+}\pi^-\pi^+$, $K^{*+} \to K^0_S \pi^+$ (TM)	0.143	$10 \pm 10*$	0.23	1.5 ± 1.5
$B^+ \to K^{*+} f^0$, $K^{*+} \to K^0_S \pi^+$, $f^0 \to \pi^+\pi^-$	0.411	5.2 ± 1.3	0.23	2.2 ± 0.6
$B^+ \to a_1^0 \pi^+$, $a_1^0 \to \rho^\pm \pi^\mp$	0.054	20.4 ± 5.8	1	5.0 ± 1.4
$B^+ \to a_1^\pm K^0_S$, $a_1^\pm \to \rho^0 \pi^+$	0.065	34.9 ± 6.7	0.346	3.6 ± 0.7
$B^+ \to K_0^{*0} \pi^+$, $K_0^{*0} \to K^+ \pi^-$	0.017	45.2 ± 6.3	0.62	2.1 ± 0.3
$\overline{B^0} \to D^{(*)0} \pi^+$, cocktail	0.019	2490 ± 150	1.000	214.8 ± 12.9
$\overline{B^0} \to D^{(*)+} X$, cocktail	0.010	4500 ± 500	1.000	204.3 ± 22.7
$B^+ \to K^{*0}(1410)\pi^+$, $K^{*0}(1410) \to K^{*+}\pi^-$ (TM)	1.95	$5 \pm 5*$	0.133	5.9 ± 5.9
$B^+ \to K^{*0}(1410)\pi^+$, $K^{*0}(1410) \to \rho^0 K^0_S$ (TM)	6.76	$5 \pm 5*$	0.008	1.2 ± 1.2
$B^+ \to K_2^{*0}(1430)\pi^+$, $K_2^{*0}(1430) \to K^{*+}\pi^-$ (TM)	2.24	5.6 ± 2.2	0.038	2.2 ± 0.9
$B^+ \to K_2^{*0}(1430)\pi^+$, $K_2^{*0}(1430) \to \rho^0 K^0_S$ (TM)	9.79	5.6 ± 2.2	0.010	2.5 ± 1.0
$B^0 \to K^{*0}(1680)\pi^+$, $K^{*0}(1680) \to K^{*+}\pi^-$ (TM)	0.85	$6.0 \pm 6.0*$	0.046	1.1 ± 1.1
$B^0 \to K^{*0}(1680)\pi^+$, $K^{*0}(1680) \to \rho^0 K^0_S$ (TM)	4.10	$6.0 \pm 6.0*$	0.036	4.1 ± 4.1

Table 5.3: Potential $B\overline{B}$ background to $B^+ \to K_1^0 \pi^+$ modes for events in class 1 (top) and class 2 (bottom). For each decay mode we give the mode number, MC reconstruction efficiency ϵ, branching fraction ($\mathcal{B}$) [5,8,98], daughter branching fraction product, estimated background in ML input. The branching fractions marked with a $*$ are assumptions. PDFs will be modeled upon a MC sample of the first decay mode listed for each category.

5.4 Fit description

We use an unbinned, extended maximum-likelihood (ML) fit to extract the signal branching fraction and production parameters. The general form of the likelihood $\mathcal{L}_{e,r}$ for a candidate e to belong to class r can be written as

$$\mathcal{L}_{e,r} = \sum_s n_{s,r}\, \mathcal{P}_{s,r}(\mathbf{x}_e;\ \boldsymbol{\zeta},\ \boldsymbol{\xi}), \tag{5.1}$$

where the probability distribution functions (PDFs) $\mathcal{P}_{s,r}$ are formed using the set of observables $\mathbf{x}_e = \{\Delta E,\ m_{\rm ES},\ \mathcal{F},\ m_{K\pi\pi},\ |\mathcal{H}|\}$, and $n_{s,r}$ are the event yields. The subscript $r = \{1, 2\}$ corresponds to one of the resonance band classes defined in Sec. 5.2.7, and the index s represents the event categories used in the fit model. The dependence on the production parameters $\boldsymbol{\zeta}$ is relevant only for the signal PDF, while $\boldsymbol{\xi}$ represents all other PDF parameters.

5.4.1 Sample composition

Several event categories are included in the fit model. The signal component accounts for the combined contribution of the $K_1(1270)$ and $K_1(1400)$ resonances to the resonant $K\pi\pi$ system in the final state, including interference effects. Background events arise primarily from random combinations of particles in continuum $e^+e^- \to q\overline{q}$ events ($q = u, d, s, c$) (combinatorial background). The combinatorial background PDF is found to describe well also the background from random combinations of B tracks, including SCF candidates from misreconstructed signal-like event topologies. Another important source of background is represented by B decays that proceed through a decay pattern similar to signal, e.g., B decays to $K^*(1410)\pi$, $K^*(1680)\pi$, $K_2^*(1430)\pi$, and the decays to the nonresonant final states $K^*\pi\pi$ and $\rho K\pi$: we refer to these background sources collectively as "peaking background", as they exhibit signal-like distributions in the $m_{\rm ES}$, ΔE, and $\mathcal{F}$ observables.

As a mean to improve the stability of the fit, the signal and peaking background categories are defined to consist of TM candidates only, while SCF candidates are allowed to be incorporated in the combinatorial background component.

For the analysis of the reconstructed B^0 modes, the fit model includes

1. signal,
2. combinatorial background,
3. $B^0 \to K^*(1410)^+\pi^-$,
4. $B^0 \to K^*(892)^0\pi^+\pi^- + \rho^0 K^+\pi^-$,
5. $B^0 \to a_1(1260)^\pm\pi^\mp$, and
6. $B^0 \to D^-_{K\pi\pi}\pi^+$.

For the reconstructed B^+ modes, the model consists of

1. signal,

2. combinatorial background,
3. $B^+ \to K^*(1410)^0\pi^+$,
4. $B^+ \to K^*(892)^+\pi^+\pi^- + \rho^0 K^0_S\pi^+$, and
5. $B^+ \to K^*(892)^+\rho^0$.

The contribution from $K^*_1(1680)\pi$ and $K^*_2(1430)\pi$ TM candidates is expected to be quantitatively small, according to the existing experimental limits on these transitions [5]. Therefore, these components are not included in the models for the B^0 or B^+ channels.

5.4.2 Free parameters

The signal branching fractions for the B meson decays to the combined $K_1(1270)\pi$ and $K_1(1400)\pi$ final state are free parameters in the fit. In the definition of $\mathcal{L}_{e,r}$ the yields of the signal category for the two classes are expressed as a function of the signal branching fraction $\mathcal{B}$ as $n_{1,1} = \mathcal{B} \times N_{B\overline{B}} \times \epsilon_1(\boldsymbol{\zeta})$ and $n_{1,2} = \mathcal{B} \times N_{B\overline{B}} \times \epsilon_2(\boldsymbol{\zeta})$, where the total selection efficiency $\epsilon_r(\boldsymbol{\zeta})$ includes the daughter branching fractions and the reconstruction efficiency obtained from MC samples as a function of the production parameters.

The yields for the event categories $s = 5, 6$ (B^0 modes) and $s = 5$ (B^+ modes) are fixed to the values estimated from MC simulated data and based on their previously measured branching fractions [5,8]. The yields for the other background components are determined from the fit. We don't impose any relation between the background yields for region 1 and the yields for the corresponding components in region 2.

The PDF parameters for the combinatorial background are left free to vary in the fit, while those for the other event categories are fixed to the values extracted from MC samples.

5.4.3 Strategy for the extraction of the production parameters

For the B^0 modes we perform a negative log-likelihood scan with respect to ϑ and ϕ. Although the events in class $r = 2$ are characterized by a smaller signal-to-background ratio with respect to the events in class $r = 1$, including these events in the fit for the B^0 modes helps to resolve ambiguities in the determination of ϕ in cases where a signal is observed. At each point of the scan, a simultaneous fit to the event classes $r = 1, 2$ is performed. For the B^+ modes, due to a less favorable signal-to-background ratio and increased background from B decays, we are not sensitive to ϕ over a wide range of possible values of the signal BF. We therefore assume $\phi = \pi$ and restrict the scan to ϑ. At each point of the scan, we perform a fit to the events in class $r = 1$ only. The fitted samples consist of 23167 events (B^0 modes, class 1), 38005 events (B^0 modes, class 2), and 9630 events (B^+ modes, class 1).

The choice $\phi = \pi$ in reconstructed B^+ decays minimizes the variations in the fit results associated with the differences between the $m_{K\pi\pi}$ PDFs for different values of ϕ. This source of systematic uncertainty is accounted for as described in Sec. 5.8. The variations in the efficiency ϵ_1 as a function of ϕ for a given ϑ can be as large as 30 %, and are taken into account in deriving the branching fraction results as discussed in Sec. 5.7.

In order to simplify the fit procedure and reduce its computational cost, the PDF parameters of the combinatorial background are extracted from a separate fit to the data, prior

to the scan. In order not to bias the results on the signal branching fractions and production parameters, this preliminary fit relies on only three observables ($\mathbf{x} = \{m_{\rm ES}, \Delta E, \mathcal{F}\}$) that are largely independent of the detailed kinematics of the $B \to K\pi\pi\pi$ decays. The number of event categories is consequently reduced in the preliminary fit. For the B^0 modes, four components are included in the model: combinatorial background, a peaking $B\overline{B}$ component, $B \to a_1\pi$, and $B \to D\pi$ decays. For the B^+ modes, only two components are included in the model: the combinatorial background, and a peaking $B\overline{B}$ component. For the peaking $B\overline{B}$ component, the $m_{\rm ES}$,ΔE and $\mathcal{F}$ signal PDFs are used. In subsequent stages, the PDF parameters for the combinatorial category are fixed to the values extracted from the preliminary fit.

5.5 Probability distribution functions

The signal and background PDFs are constructed as products of the PDFs describing the distribution of each observable. The factorizability of the PDFs rests on the assumption of negligible correlations between the corresponding observables.

5.5.1 Correlations

The assumption of negligible correlations among the discriminating variables in the selected data samples has been tested with Monte Carlo samples and in on-resonance data.

In on-resonance data, the largest linear correlation coefficient is obtained between the $\mathcal{H}$ and $m_{K\pi\pi}$ observables, and amounts to 13%. The effect of this correlation has been studied by parameterizing the PDF for $\mathcal{H}$ and $m_{K\pi\pi}$ with a two-dimensional nonparametric model, modeled on on-resonance data, and repeating the fits. No significant difference was observed with respect to the fit with the factorized form. The other linear correlation coefficients are below the 10% level.

The linear correlation between two variables x, y in the reweighted samples can be evaluated as

$$\sigma_{xy} \equiv \frac{\sum_i w_i (x_i - \bar{x})(y_i - \bar{y})}{\sqrt{\sum_i w_i (x_i - \bar{x})^2}\sqrt{\sum_i w_i (y_i - \bar{y})^2}}, \tag{5.2}$$

where $\bar{x} \equiv \frac{\sum_i w_i x_i}{\sum_i w_i}$, and the index i runs over the selected events. For the Monte Carlo signal events linear correlations are below the 10% level, with the largest values corresponding to the ΔE-$m_{K\pi\pi}$ (9% in B^0 decay modes) and $m_{\rm ES}$-$m_{K\pi\pi}$ (-10% in B^+ decay modes) correlation coefficients. These values do not depend sensibly on the production parameters used in reweighting the sample. The effect of correlations in signal-like components is taken into account in systematic uncertainties.

5.5.2 PDF parameterization

The ΔE and $m_{\rm ES}$ PDFs of the categories 1, 3, 4, and 5 are each parameterized as a sum of a Gaussian function to describe the core of each distribution, plus an empirical function determined from MC simulated data to account for the tails of the distribution.

For the combinatorial background we use a first degree Chebyshev polynomial for ΔE and an empirical phase-space function [97] for $m_{\rm ES}$:

$$f(x) \propto x\sqrt{1-x^2}\exp\left[-\xi_1(1-x^2)\right], \tag{5.3}$$

where $x \equiv 2m_{\rm ES}/\sqrt{s}$ and ξ_1 is a parameter that is determined from the fit.

For all categories the $\mathcal{F}$ distribution is well described by a Gaussian function with different widths to the left and right of the mean. A second Gaussian function with a larger width accounts for a small tail in the distribution and prevents the background probability from becoming too small in the signal $\mathcal{F}$ region. The $m_{\rm ES}$, ΔE, and $\mathcal{F}$ PDFs for the signal and continuum background components are shown in Fig. 5.2.

The production of $K_1^*(1410)$ and $a_1(1260)$ resonances, occurring in B background, is taken into account in the corresponding $m_{K\pi\pi}$ (Fig. 5.3) and $|\mathcal{H}|$ PDFs. For all components, the PDF for $|\mathcal{H}|$ is parameterized with polynomials (Fig. 5.4). The $m_{K\pi\pi}$ distribution for the signal depends on $\boldsymbol{\zeta}$. To each point of the $\boldsymbol{\zeta}$ scan we therefore associate a different

nonparametric template (Fig. 5.5), modeled upon signal MC samples reweighted according to the corresponding values of the production parameters ϑ and ϕ, as described in Sec. 5.5.3.

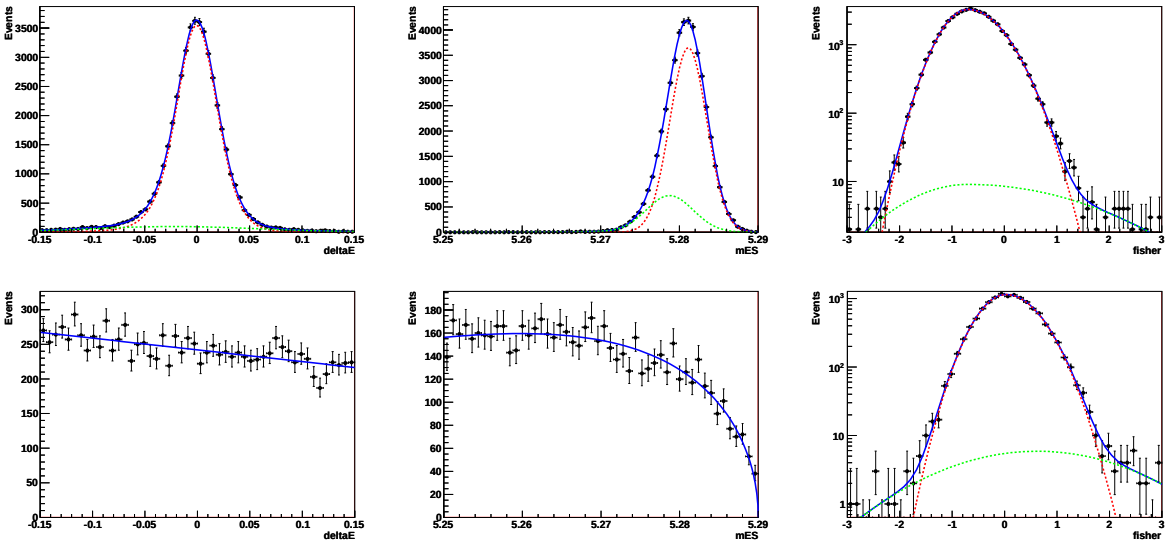

Figure 5.2: PDF for signal (top) and continuum background (bottom, modeled on off-resonance data) "class 1" events reconstructed in the $B^0 \to K_1^+\pi^-$ mode. From left to right: ΔE, $m_{\rm ES}$, $\mathcal{F}$.

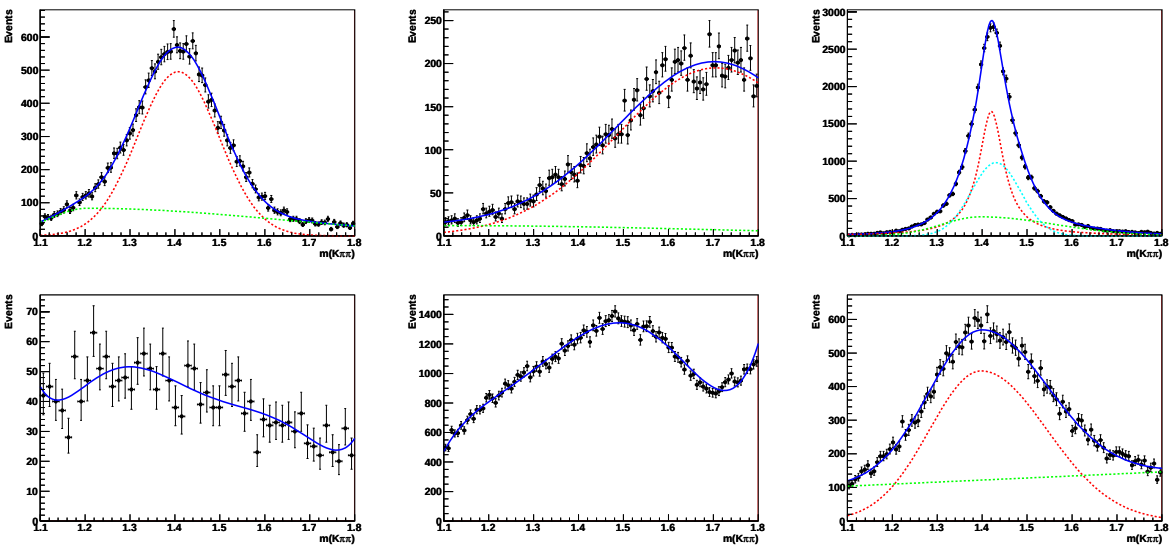

Figure 5.3: PDF for $m_{K\pi\pi}$ in "class 1" background events reconstructed as $B^0 \to K_1^+\pi^-$. Top, from left to right: $B^0 \to K_1^*(1410)^+\pi^-$, $B^0 \to K_1^*(1680)^+\pi^-$, and $B^0 \to K_2^*(1430)^+\pi^-$ components. Bottom, from left to right: continuum background (modeled on off-resonance data), $B^0 \to K^*(892)^0\pi^+\pi^-$, and $B^0 \to a_1(1260)^\pm\pi^\mp$ components.

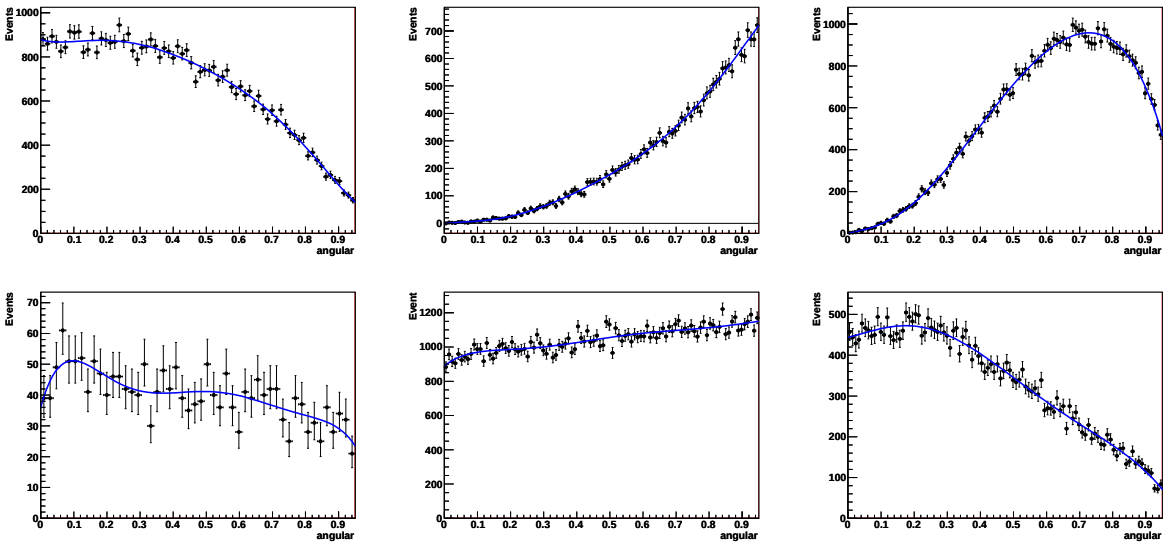

Figure 5.4: PDF for $\mathcal{H}$ in "class 1" signal and background events reconstructed as $B^0 \to K_1^+\pi^-$. Top, from left to right: signal, $B^0 \to K_1^*(1410)^+\pi^-$, and $B^0 \to K_2^*(1430)^+\pi^-$ events. Bottom, from left to right: continuum background (modeled on off-resonance data), $B^0 \to K^*(892)^0\pi^+\pi^-$, and $B^0 \to a_1(1260)^\pm\pi^\mp$ events.

5.5.3 Parameterization of the $m_{K\pi\pi}$ signal PDF

The $m_{K\pi\pi}$ distribution in signal is described with a nonparametric PDF modeled upon reweighted signal Monte Carlo events. A one-dimensional kernel estimation PDF (KEYS; for a brief introduction to applications of kernel estimation in High Energy Physics, see Ref. [99]) is implemented in the `ROOT` framework as the `RooKeysPdf` class. We have modified this class in order to handle weighted datasets.

The level of "smoothing" achieved by the KEYS PDF is governed by a scale factor parameter, that is optimized separately for the B^0 class 1, B^0 class 2, and B^+ class 1 events. The chosen scale parameter is used for all ϑ and ϕ values.

A KEYS PDF is evaluated for each of the points of the scan on the two-dimensional space spanned by the production parameters $\boldsymbol{\zeta}$ (Fig. 5.6 – 5.8). Since the runtime computation of the function at different $m_{K\pi\pi}$ values is computing costly, we have implemented a lookup table method. We have extended the lookup table to parameterize the dependence of the PDF shape on the production parameters $\boldsymbol{\zeta}$. This allows to retrieve the PDF values from precalculated values in memory, using interpolation for values that fall between two precomputed values.

A common issue when dealing with KEYS PDFs with a gaussian kernel (as in the `RooKeysPdf` class) is the parameterization of the distribution near the definition boundaries for the observable, determined by the selection cuts. The `RooKeysPdf` class implements a mirroring technique by which the $m_{K\pi\pi}$ distribution is "reflected" across each boundary. We found, however, that the resulting distribution does not satisfactorily model the region at the boundary. A better technique consists in temporarily extending the selection limits on $m_{K\pi\pi}$ so that the range in which we are interested is well within the new $m_{K\pi\pi}$ definition boundaries. After modeling the PDF and filling the lookup tables, the $m_{K\pi\pi}$ range can be brought back to the original range.

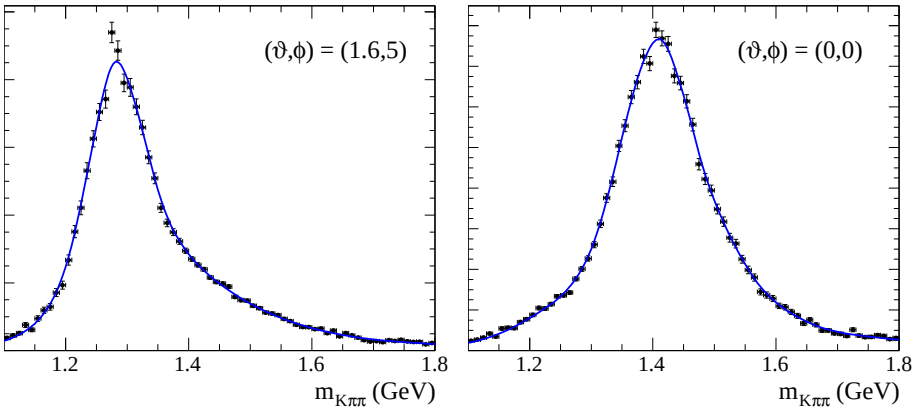

Figure 5.5: PDF for $m_{K\pi\pi}$ in "class 1" $K_1(1270)\pi$ ($\vartheta = \pi/2$, left) and $K_1(1400)\pi$ ($\vartheta = 0$, right) signal events reconstructed in the $B^0 \to K_1^+\pi^-$ mode.

5.5.4 Data/MC corrections

We use large control samples to verify the m_{ES}, ΔE, and $\mathcal{F}$ PDF shapes that are determined from Monte Carlo samples. We use the $B^0 \to D^-\pi^+$ decay with $D^- \to K^+\pi^-\pi^-$, and the $B^+ \to \bar{D}^0\pi^-$ decay with $D^0 \to K^0_S\pi^+\pi^-$, which have similar topology to the signal B^0 and B^+ modes, respectively. We select these samples by applying loose requirements on m_{ES} and ΔE, and requiring for the D candidate mass $1848 < m_{D^-} < 1890$ MeV and $1843 < m_{D^0} < 1885$ MeV. The selection requirements on the B and D daughters are similar to those for the $B \to K_1\pi$ modes. These selection criteria are applied both to the data and to the MC events.

There is good agreement between data and MC samples: the deviations in the means of the distributions are about 0.5 MeV for m_{ES}, 3 MeV for ΔE, and negligible for $\mathcal{F}$. We apply shifts and scale factors, listed in Tables 5.4 and 5.5, to the parameters of core Gaussians for $m_{\rm ES}$, ΔE, and $\mathcal{F}$.

PDF	μ shift	$\sigma_{(L)}$ scale	σ_R scale
ΔE	-0.00327 ± 0.00033	1.071 ± 0.015	
$m_{\rm ES}$	-0.00050 ± 0.00004	1.068 ± 0.014	
$\mathcal{F}$	0.038 ± 0.018	1.042 ± 0.026	0.918 ± 0.024

Table 5.4: Data/MC corrections for the B^0 modes, evaluated from studies of the $B^0 \to D^-\pi^+$, $D^- \to K^+\pi^-\pi^-$ control sample.

PDF	μ shift	$\sigma_{(L)}$ scale	σ_R scale
ΔE	-0.00381 ± 0.00052	0.994 ± 0.022	
$m_{\rm ES}$	-0.00059 ± 0.00007	1.051 ± 0.024	
$\mathcal{F}$	0.018 ± 0.033	1.067 ± 0.049	0.942 ± 0.041

Table 5.5: Data/MC corrections for the B^+ modes, evaluated from studies of the $B^+ \to D^0\pi^+$, $D^0 \to K^0_S\pi^+\pi^-$ control sample.

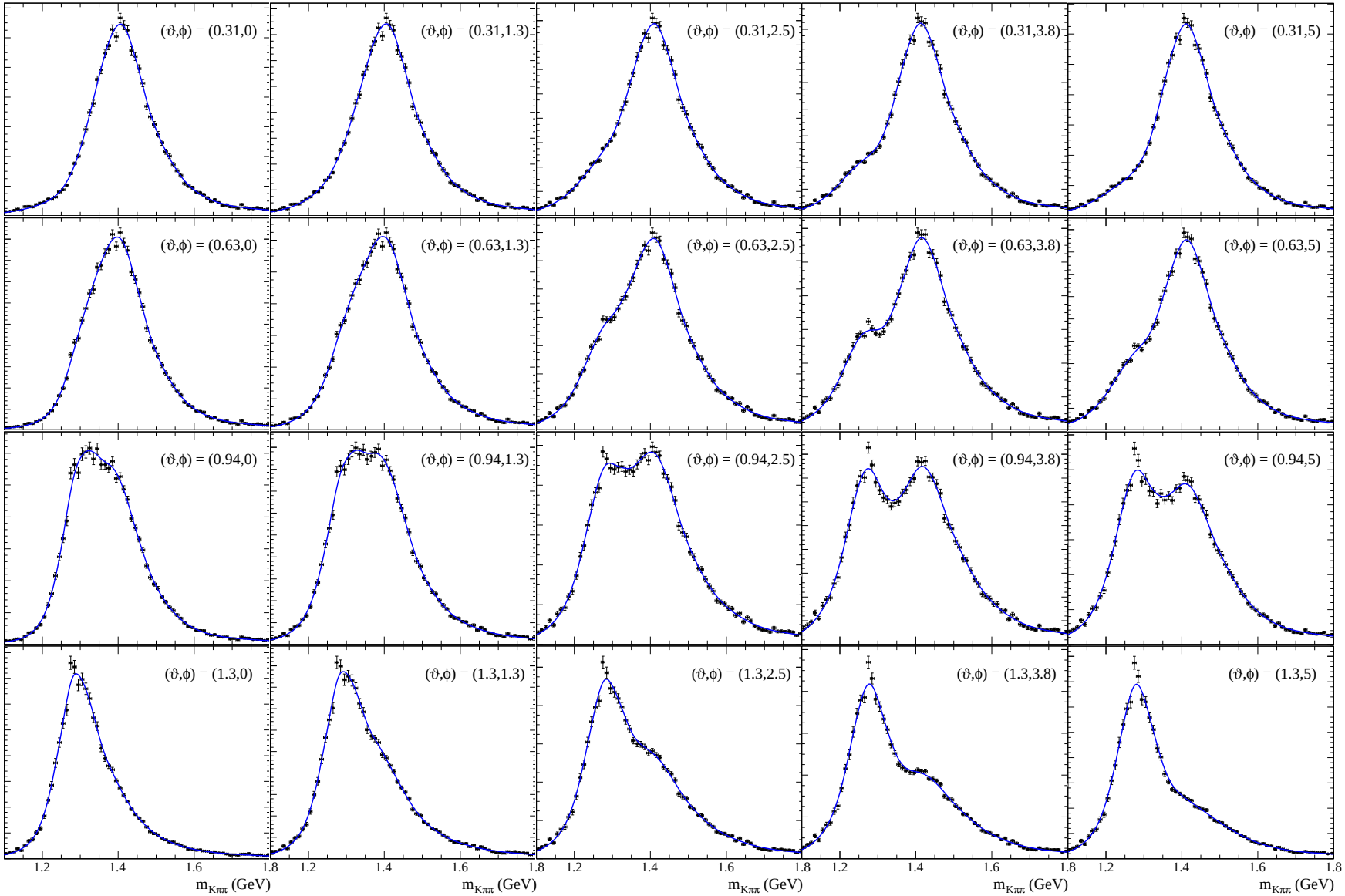

Figure 5.6: $m_{K\pi\pi}$ PDF templates for $B^0 \to K_1^+\pi^-$ "class 1" events, evaluated at regular intervals in the two-dimensional space spanned by the production parameters $\boldsymbol{\zeta}$.

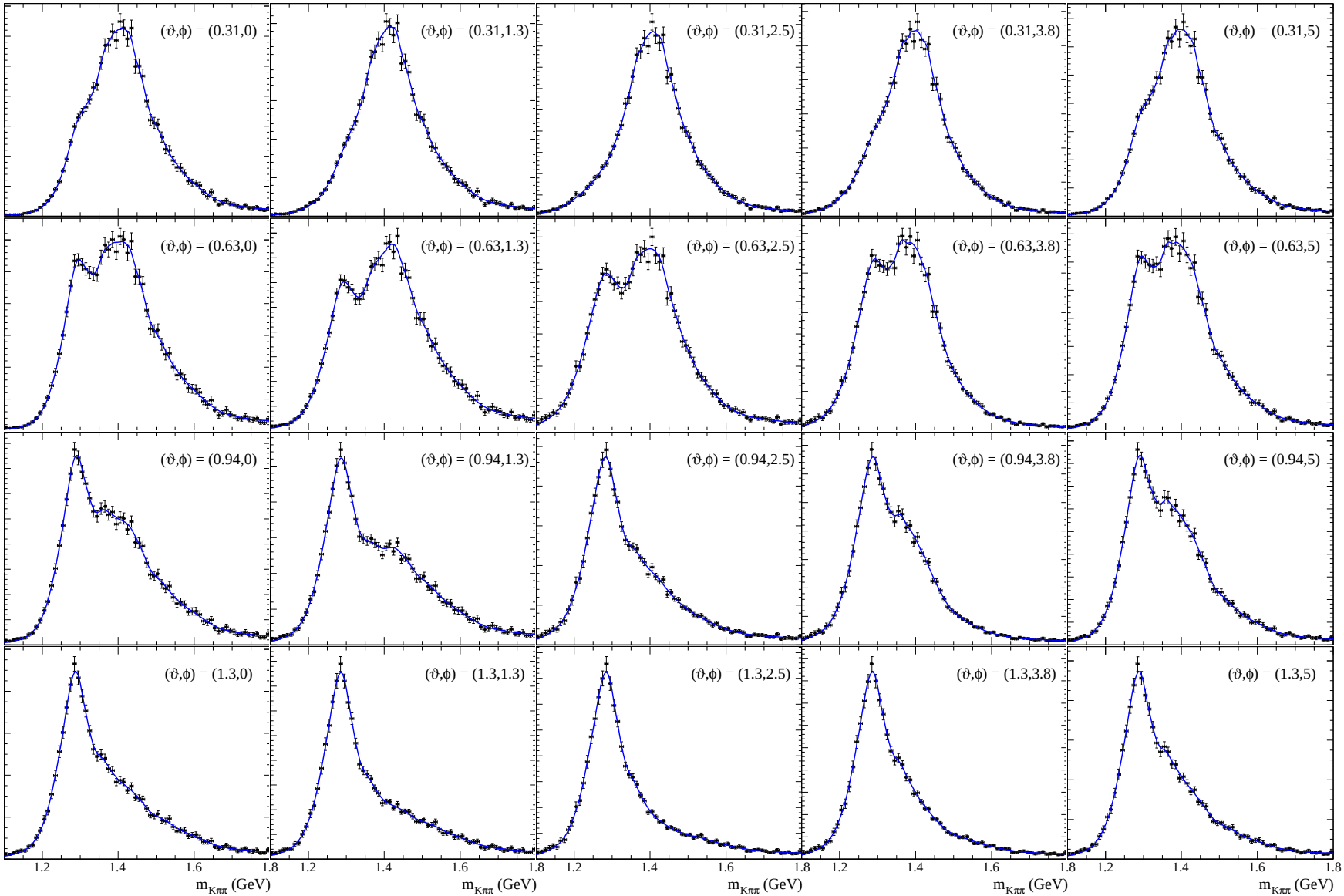

Figure 5.7: $m_{K\pi\pi}$ PDF templates for $B^0 \to K_1^+\pi^-$ "class 2" events, evaluated at regular intervals in the two-dimensional space spanned by the production parameters $\boldsymbol{\zeta}$.

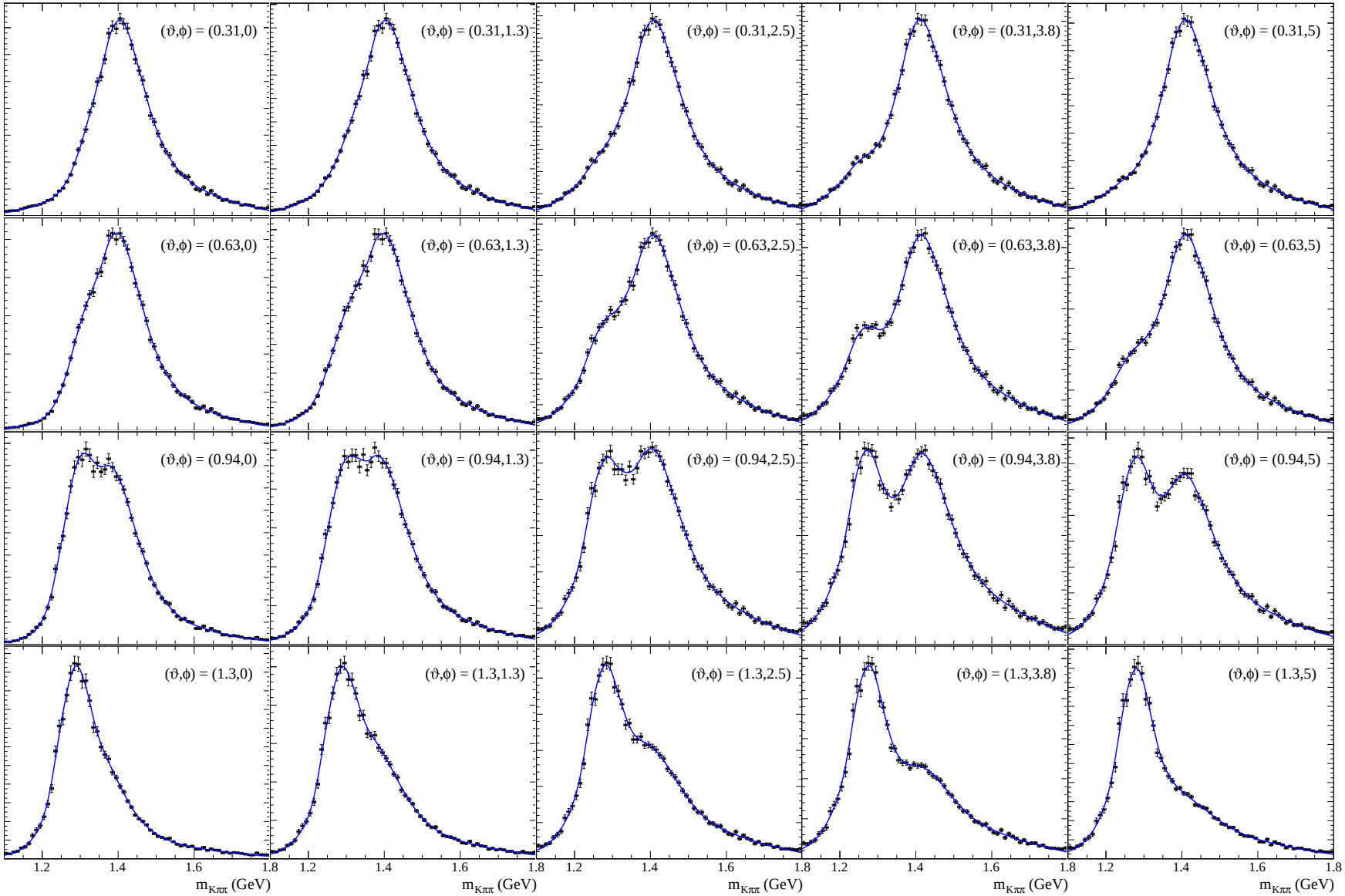

Figure 5.8: $m_{K\pi\pi}$ PDF templates for $B^+ \to K_1^0\pi^+$ "class 1" events, evaluated at regular intervals in the two-dimensional space spanned by the production parameters $\boldsymbol{\zeta}$.

5.6 Validation of the fit procedure

In order to study possible biases introduced by the fit we have applied the fit procedure to several Monte Carlo samples and studied the distribution of the fit results. Two variants of these tests are performed: "pure" toys, in which the full sample is generated from the fit model, and "embedded" toys, in which events from fully simulated MC samples are included in the sample (continuum background and generic $B\overline{B}$ events are generated from the PDFs, since the available MC samples are not sufficient to perform a significant number of tests).

Pure toys assess the overall feasibility of the optimization procedure, the stability, and the expected sensitivity of the fit for any free parameter in the model (in particular $\mathcal{B}$, ϑ, ϕ). Embedded toys are more suited to estimate the effect of the simplifications introduced in the model of the signal and $B\overline{B}$ background contributions. Such model inaccuracies include: neglected correlations between discriminating variables; inappropriate choices of PDF parameterizations (e.g., due to the lack of MC statistics or to the computational cost associated to other parameterizations); the presence of event species for which no explicit component has been introduced (e.g. SCF events).

In order to reduce the time needed to perform these tests we do not perform the likelihood scan over the range for ϑ. Instead, at each step of the likelihood scan over the range for ϕ, we minimize the negative log-likelihood with respect to the yields and also ϑ.

The size of each simulated sample is tuned to reproduce the size of the on-resonance selected data sample. The sample composition reflects the expected number of events in each component of the model. In embedded toys, SCF candidates originating in signal and peaking background events are also included in the expected proportion.

The signal branching fraction in B^0 modes is assumed to be $\mathcal{B} = 28 \times 10^{-6}$, which is an educated guess based on the results of the preliminary analysis in Ref. [100]. For B^+ modes, we have repeated the validation procedure for 0, 80, and 170 signal events. The values of the production parameters ϑ and ϕ for each sample are generated randomly according to a uniform distribution over the physical range. The signal TM and SCF events are then embedded using an accept and reject method, in which the weights are calculated as described in Sec. 3.7.

An auxiliary set of toys has shown that for the B^+ modes the extraction of ϕ is not reliable; the results shown in the following are therefore obtained with the revised strategy, described in Sec. 5.4.3, in which ϕ is fixed in the analysis of the B^+ modes. The results of the pure toys are shown in Fig. 5.9 and Fig. 5.10 for the B^0 and B^+ modes, respectively, while the results of the embedded toys are shown in Fig. 5.11 and Fig. 5.12. The distributions of the fitted signal yield or branching fraction and of its error are reported: the bias is under control both for B^0 and B^+ modes. The nonresonant $K^*\pi\pi + \rho K\pi$ and continuum background components serve as "garbage collectors" for SCF events, whose presence does not impact the signal extraction. Finally, the extracted production parameters are compared to the generated values and demonstrate the linearity of the fit response.

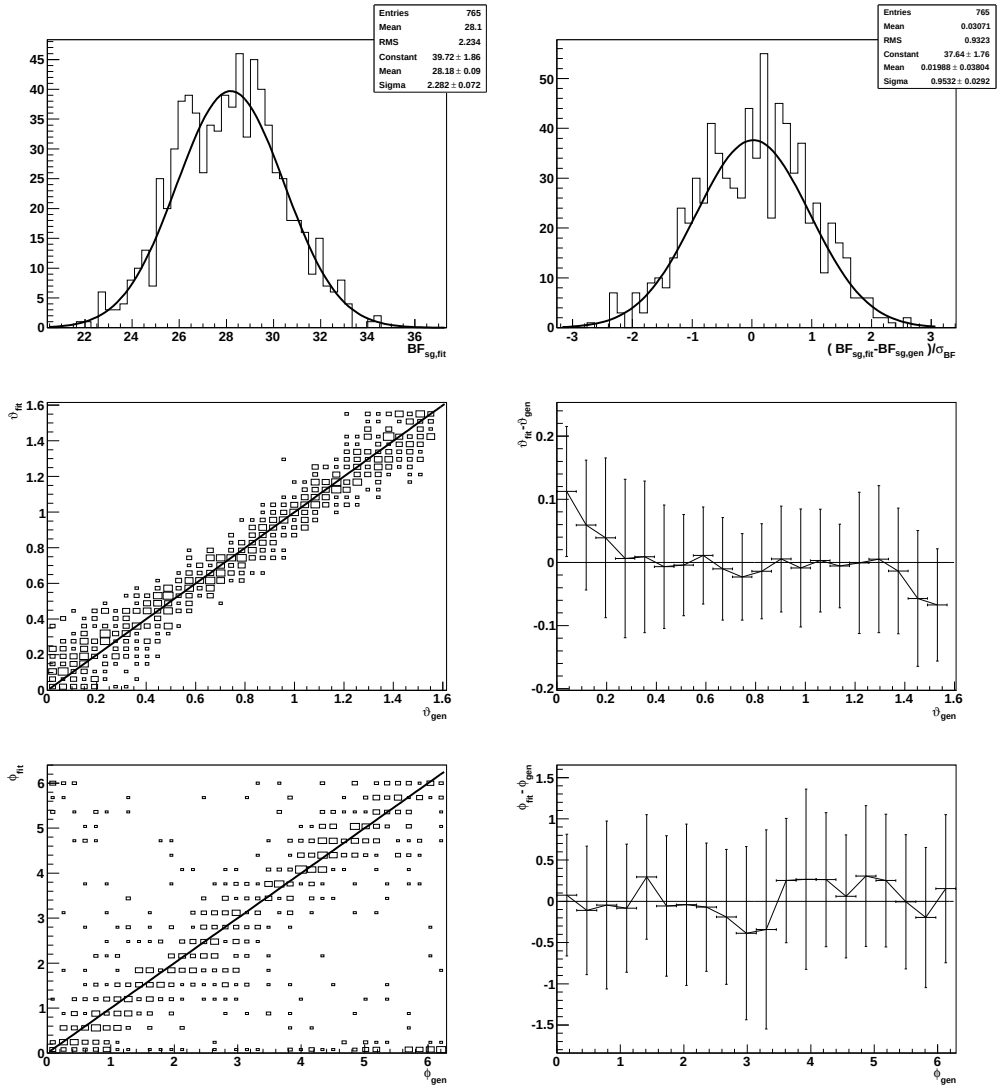

Figure 5.9: Results of the pure toys for the B^0 modes. Top: distributions of the fitted values (left) and normalized residuals (right) for the signal branching fraction. Middle, bottom: distributions of the fitted values (left) and residuals (right) for the production parameters ϑ (middle) and ϕ (bottom).

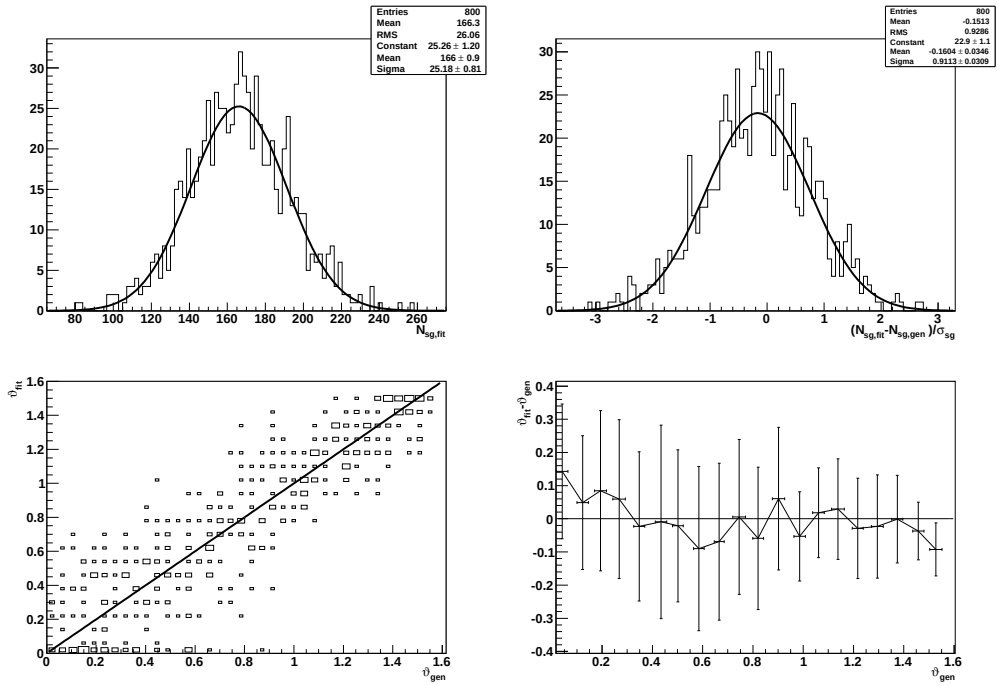

Figure 5.10: Results of the pure toys for the B^+ modes. Top: distributions of the fitted values (left) and normalized residuals (right) for the signal yield. Bottom: distributions of the fitted values (left) and residuals (right) for the production parameter ϑ.

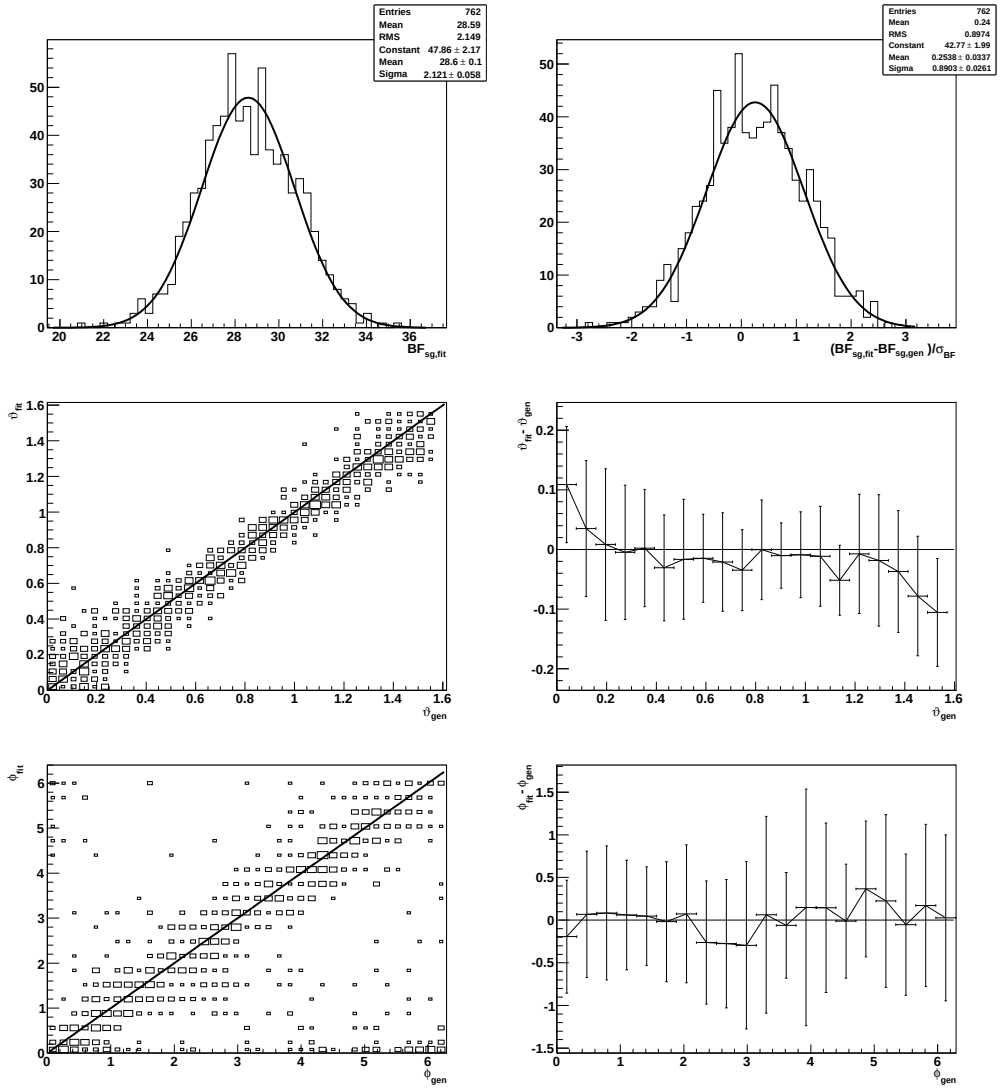

Figure 5.11: Results of the embedded toys for the B^0 modes. Top: distributions of the fitted values (left) and normalized residuals (right) for the signal branching fraction. Middle, bottom: distributions of the fitted values (left) and residuals (right) for the production parameters ϑ (middle) and ϕ (bottom).

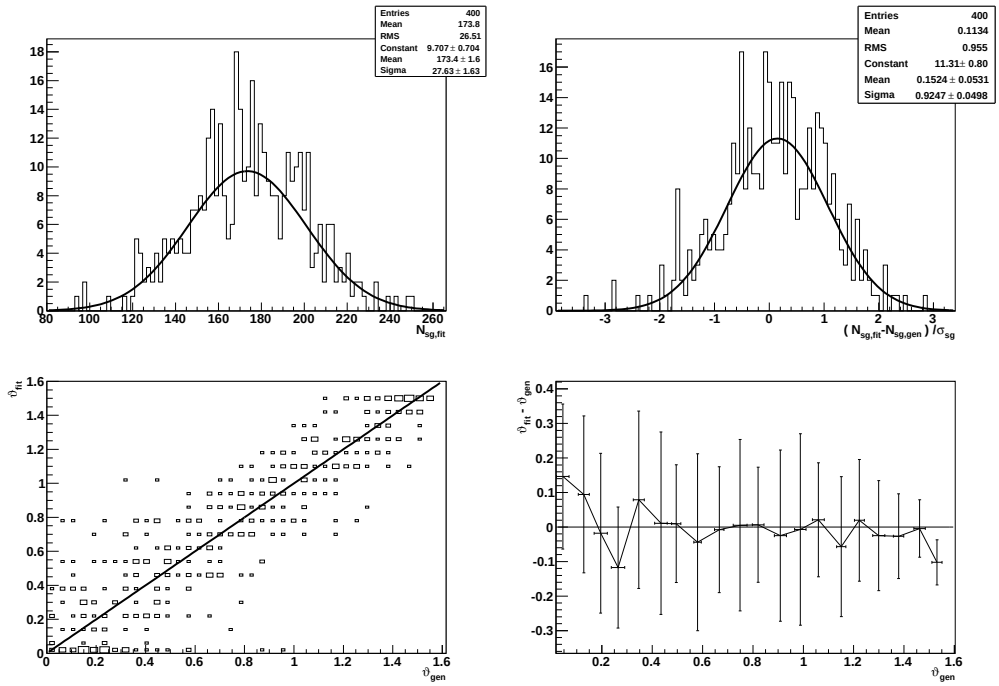

Figure 5.12: Results of the embedded toys for the B^+ modes. Top: distributions of the fitted values (left) and normalized residuals (right) for the signal yield. Bottom: distributions of the fitted values (left) and residuals (right) for the production parameter ϑ.

5.7 Results

The results of the likelihood scans are shown in Table 5.6 and Fig. 5.13. At each point of the $\boldsymbol{\zeta}$ scan the $-2\ln\mathcal{L}(\mathcal{B};\boldsymbol{\zeta})$ function is minimized with respect to the signal branching fraction $\mathcal{B}$. Contours for the value $\mathcal{B}_{\rm max}(\boldsymbol{\zeta})$ that maximizes $\mathcal{L}(\mathcal{B};\boldsymbol{\zeta})$ are shown in Fig. 5.13c and Fig. 5.13d as a function of the production parameters $\boldsymbol{\zeta}$, for B^0 and B^+ modes, respectively. The associated statistical error $\sigma_{\mathcal{B}}(\boldsymbol{\zeta})$ at each point $\boldsymbol{\zeta}$, given by the change in $\mathcal{B}$ when the quantity $-2\ln\mathcal{L}(\mathcal{B};\boldsymbol{\zeta})$ increases by one unit, is displayed in Fig. 5.13e and Fig. 5.13f.

Systematics are included by convolving the experimental two-dimensional likelihood for ϑ and ϕ, $\mathcal{L}\equiv\mathcal{L}(\mathcal{B}_{\rm max}(\boldsymbol{\zeta});\boldsymbol{\zeta})$, with a two-dimensional Gaussian that accounts for the systematic uncertainties. In Fig. 5.14a and Fig. 5.14b we show the resulting distributions in ϑ and ϕ. The 68% and 90% probability regions are shown in dark and light shading, respectively, and are defined as the regions consisting of all the points that satisfy the condition $\mathcal{L}(r)>x$, where the value x is such that $\int_{\mathcal{L}(r)>x}\mathcal{L}(\vartheta,\phi)\mathrm{d}\vartheta\mathrm{d}\phi = 68\%\ \ (90\%)$.

Table 5.6: Results of the ML fit at the absolute minimum of the $-\ln\mathcal{L}$ scan. The first two rows report the values of the production parameters (ϑ,ϕ) that maximize the likelihood. The third and fourth rows are the reconstruction efficiencies, including the daughter branching fractions, for class 1 and class 2 events. The fifth row is the correction for the fit bias to the signal branching fraction. The sixth row reports the results for the $B\to K_1(1270)\pi + K_1(1400)\pi$ branching fraction and its error (statistical only).

	$B^0\to K_1^+\pi^-$	$B^+\to K_1^0\pi^+$
ϑ	0.86	0.71
ϕ	1.26	3.14 (fixed)
ϵ_1 (%)	3.74	1.36
ϵ_2 (%)	1.68	–
Fit bias correction ($\times10^{-6}$)	+0.0	+0.7
$\mathcal{B}$ ($\times10^{-6}$)	32.1 ± 2.4	22.8 ± 5.1

5.7.1 Statistical significance

The significance is calculated from a likelihood ratio test $\Delta(-2\ln\mathcal{L})$, where $\Delta(-2\ln\mathcal{L})$ is the difference between the value of $-2\ln\mathcal{L}$ (convolved with systematic uncertainties) for zero signal and the value at its minimum for given values of $\boldsymbol{\zeta}$.

In order to include the contribution of systematic uncertainties, we convolute the likelihood with a gaussian function with mean $\mu = 0$, and width σ given by the sum in quadrature of the additive systematic effects, excluding interference. Interference effects are not included in this calculation since the significance is related to the probability to observe an upward fluctuation - mimicking signal - under the no-signal hypothesis: if no signal is present, the interference of any other component with the signal itself vanishes, and so does the associated systematic uncertainty.

A χ^2 distribution for $\Delta(-2\ln\mathcal{L})$ is assumed. For the charged modes we have verified (by means of toy experiments) that floating the parameter ϑ results in one more degree of freedom in addition to the branching fraction. A similar test for the neutral modes

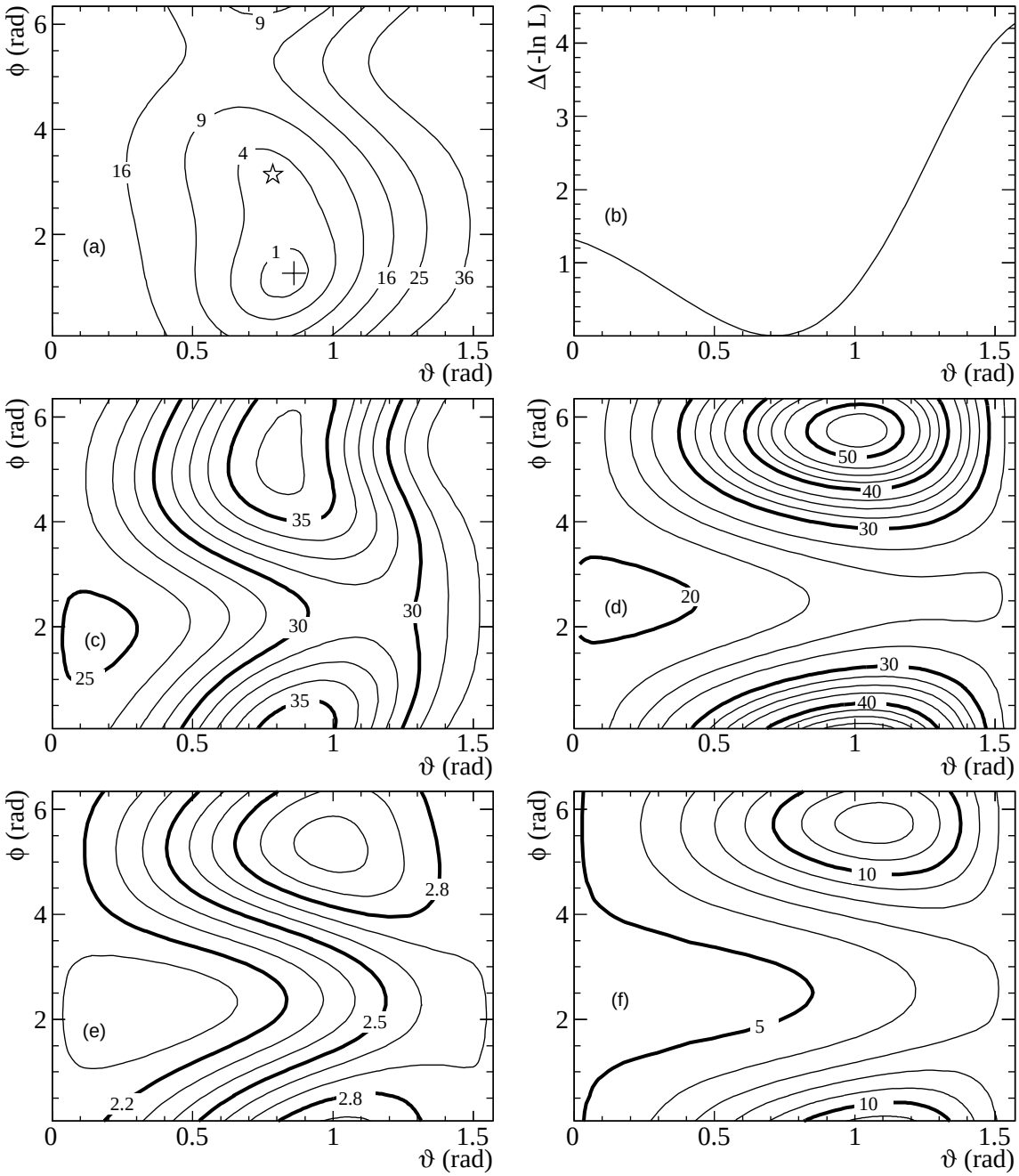

Figure 5.13: (a, b) $-\ln\mathcal{L}$ scan (systematics not included) in the production parameters ϑ and ϕ for the (a) B^0 and (b) B^+ modes. The cross in (a) indicates the position of the absolute minimum in the $-\ln\mathcal{L}$ scan. A second, local minimum is indicated by a star and corresponds to an increase in $\Delta(-\ln\mathcal{L})$ of 2.7 with respect to the absolute minimum. (c, d) Contours for the $B \to K_1(1270)\pi + K_1(1400)\pi$ branching fraction (in units of 10^{-6}) extracted from the ML fit for the (c) B^0 and (d) B^+ modes. (e, f) Contours for the statistical error (in units of 10^{-6}) on the $B \to K_1(1270)\pi + K_1(1400)\pi$ branching fraction for the (e) B^0 and (f) B^+ modes.

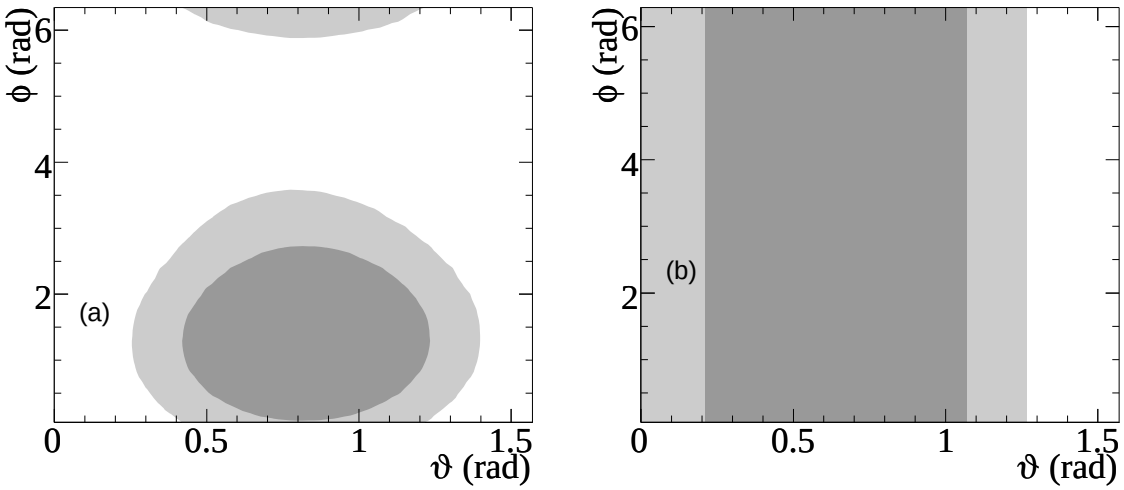

Figure 5.14: (a, b) 68% (dark shaded zone) and 90% (light shaded zone) probability regions for ϑ and ϕ for the (a) B^0 and (b) B^+ modes.

is not feasible, but we assume that the behaviour of ϑ is the same. In order to take into account the fact that for the neutral modes also ϕ is left float in the fit, we average the likelihood over ϕ keeping ϑ fixed to the value which minimizes the NLL, $\vartheta = \vartheta_{min}$. We observe nonzero $B^0 \to K_1^+\pi^-$ and $B^+ \to K_1^0\pi^+$ branching fractions with 7.5σ and 3.2σ significance, respectively, calculated assuming a χ^2 distribution for $\Delta(-2\ln\mathcal{L})$ with 2 degrees of freedom.

5.7.2 sPlot projections

The event-weighting technique ${}_s\mathcal{P}$lot [101] allows to unfold the contributions of the individual N_s components to the distribution observed in data for a given control variable.

A set of discriminating variables is used to analyze the data sample, i.e., to determine the event yields $\hat{\mathbf{N}}$ and parameters $\hat{\theta}$ that are free parameters in the fit model. From this information, a weight ${}_s\mathcal{P}_n(\mathbf{y}_e)$ for each event e is determined, which represents the probability for that event to belong to the specie n:

$$ {}_s\mathcal{P}_n(\mathbf{y}_e) = \frac{\sum_{j=1}^{N_s} \mathbf{V}_{nj} f_j(\mathbf{y}_e)}{\sum_{k=1}^{N_s} N_k f_k(\mathbf{y}_e)}, \tag{5.4} $$

with the matrix $\mathbf{V}$ defined according to

$$ \mathbf{V}^{-1}_{nj} = \sum_{e=1}^{N} \frac{f_n(\mathbf{y}_e) f_j(\mathbf{y}_e)}{(\sum_{k=1}^{N_s} N_k f_k(\mathbf{y}_e))^2}, \tag{5.5} $$

where f_i is the (known, e.g., from MC studies) PDF of the i-th component for the discriminating variables $\mathbf{y}_e$. This background subtraction method relies on the prior knowledge of the distributions of a subset $\mathbf{y}$ of the discriminating variables to calculate the ${}_s\mathcal{P}$lot histogram (i.e., the histogram obtained by weighting each event with ${}_s\mathcal{P}_n(\mathbf{y}_e)$), defined as

$$ N_n \; {}_s\tilde{M}_n(\bar{x}) \; \mathcal{V}_x \equiv \sum_{x_e \subset \delta_x} {}_s\mathcal{P}_n(\mathbf{y}_e). \tag{5.6} $$

The ${}_s\mathcal{P}$lot histogram reproduces on average the distribution $\mathbf{M}_n$ and the normalization N_n of the event specie n in the set of control variables x, under the assumption that all the observables in the chosen subset of the discriminating variables are uncorrelated with the control variables:

$$\langle N_n \; {}_s\tilde{M}_n(\bar{x})\mathcal{V}_x\rangle = N_n\mathbf{M}_n(x). \tag{5.7}$$

In the above equations, $\bar{x}$ is the middle point of the bin δ_x and $\mathcal{V}_x$ is the volume of the bin. The projection variable x has therefore to be excluded from the set $\mathbf{y}$ when calculating the corresponding ${}_s\mathcal{P}$lot histogram. In the calculation of the weights for all histograms we have used for the yields $\hat{\mathbf{N}}$ and the parameters $\hat{\theta}$ the values extracted from the nominal fit (i.e., the one including $m_{\rm ES}$, ΔE, $\mathcal{F}$, $\mathcal{H}$, $m_{K\pi\pi}$).

In the original ${}_s\mathcal{P}$lot implementation, the matrix $\mathbf{V}^{-1}$ was obtained from the covariance matrix resulting from the fit

$$\mathbf{V}^{-1}_{nj} = \frac{\partial^2(-\mathcal{L})}{\partial N_n \partial N_j} = \sum_{e=1}^{N} \frac{f_n(\mathbf{y}_e)f_j(\mathbf{y}_e)}{(\sum_{k=1}^{N_s} N_k f_k(\mathbf{y}_e))^2}, \tag{5.8}$$

where $\mathbf{y}_e$ represents the reduced set of discriminating variables for the event e. We have verified that this option is numerically less accurate than the direct computation, and does not easily generalize to models with fixed components in the fit.

Figures 5.15 and 5.16 show the distributions of ΔE, $m_{\rm ES}$ and $m_{K\pi\pi}$ for the signal and combinatorial background events. Since $m_{K\pi\pi}$ is the main observable for the discrimination between signal and peaking background, in calculating the $m_{K\pi\pi}$ ${}_s\mathcal{P}$lot we only attempt to subtract the continuum background from the combined contribution of signal and peaking background components.

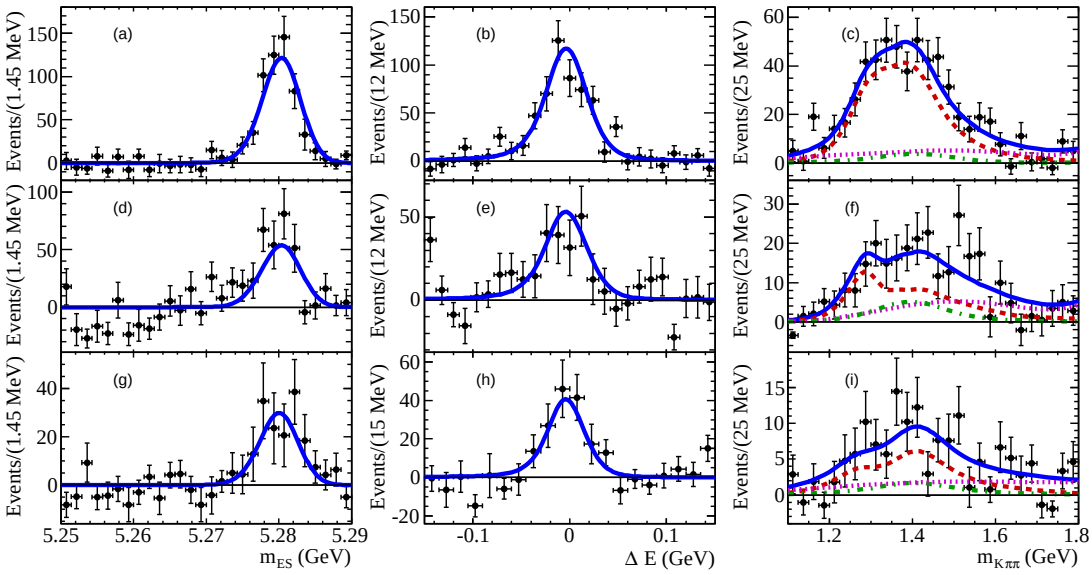

Figure 5.15: sPlot projections of signal onto $m_{\rm ES}$ (left), ΔE (center), and $m_{K\pi\pi}$ (right) for B^0 class 1 (top), B^0 class 2 (middle), and B^+ class 1 (bottom) events: the points show the sums of the signal weights obtained from on-resonance data. For $m_{\rm ES}$ and ΔE the solid line is the signal fit function. For $m_{K\pi\pi}$ the solid line is the sum of the fit functions of the decay modes $K_1(1270)\pi + K_1(1400)\pi$ (dashed), $K^*(1410)\pi$ (dash-dotted), and $K^*(892)\pi\pi$ (dotted), and the points are obtained without using information about resonances in the fit, *i.e.*, we use only the $m_{\rm ES}$, ΔE, and $\mathcal{F}$ variables.

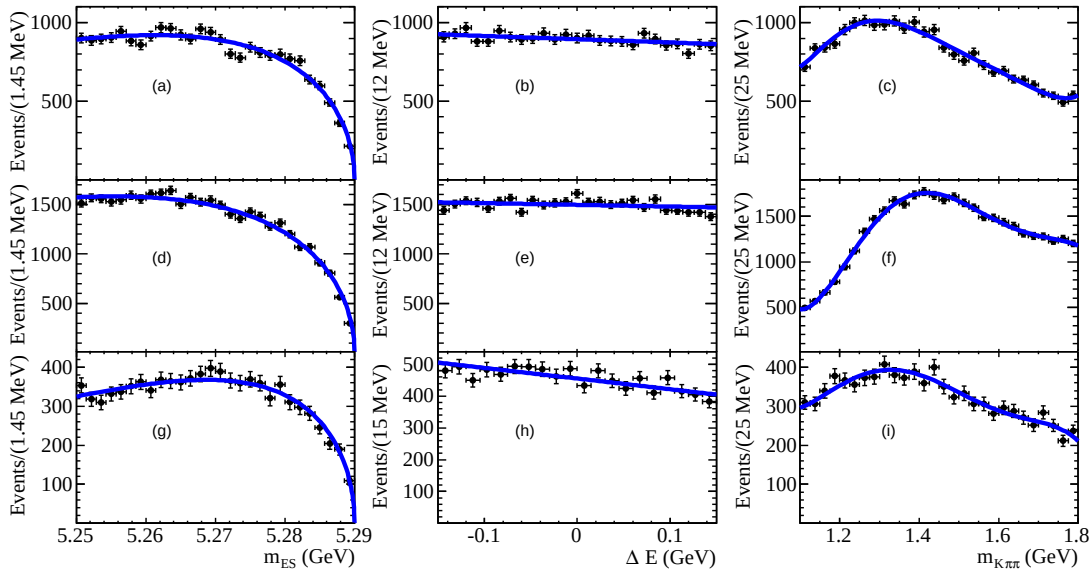

Figure 5.16: sPlot projections of combinatorial background onto $m_{\rm ES}$ (left), ΔE (center), and $m_{K\pi\pi}$ (right) for B^0 class 1 (top), B^0 class 2 (middle), and B^+ class 1 (bottom) events: the points show the sums of the combinatorial background weights obtained from on-resonance data. The solid line is the combinatorial background fit function. For $m_{K\pi\pi}$ the points are obtained without using information about resonances in the fit, *i.e.*, we use only the $m_{\rm ES}$, ΔE, and $\mathcal{F}$ variables.

5.8 Systematic errors

The main sources of systematic uncertainties are listed below and summarized in Table 5.7. For the branching fractions, the errors that affect the results only through efficiencies are called "multiplicative" and given in percentage. All other errors are labeled "additive" and expressed in units of 10^{-6}.

5.8.1 Additive uncertainties

- PDF parameters: we repeat the fit by varying, within their uncertainties, the PDF parameters $\boldsymbol{\xi}$ that are not left floating in the fit.
- MC/data corrections: we take into account data/MC discrepancies in the parameters of the core Gaussians for signal $m_{\rm ES}$, ΔE, and $\mathcal{F}$ PDFs, and we repeat the fit by varying the corrections within their uncertainties (Sec. 5.5.4).
- ML fit bias: the signal PDF model excludes fake combinations originating from misreconstructed signal events. Potential biases due to the presence of fake combinations, or other imperfections in the signal PDF model (e.g., neglected correlations), are estimated with MC simulated events, i.e., we repeat the validation exercise feeding the MC simulation with the parameters extracted from the unblind nominal fit to the on-resonance data.
- Fixed phase ϕ: for B^+ modes, we introduce an additional additive systematic uncertainty to account for the variations of the ϕ parameter. We repeat the fit several times, generating ϕ at random at each iteration. The additive systematics uncertainties on $\mathcal{B}$ and ϑ are evaluated by comparing the mean and RMS of the distribution of the refitted values with the results of the nominal fit ($\phi = \pi$).
- Scan: we account for the possible bias introduced by the finite resolution of the (ϑ, ϕ) likelihood scan.
- K_1 K-matrix parameters: a systematic error is associated to variations in the $K_1(1270)$ and $K_1(1400)$ mass poles and $K-$matrix parameters in the signal model. Since the parameters of the $K-$matrix are correlated with the mass poles, we only vary the K_1 mass poles. We evaluate this systematic effect by means of MC simulated experiments. In the signal model used for the simulation, the positions of the K_{1a} and K_{1b} mass poles are varied by ± 0.02 GeV, while the fit is performed with the nominal model.
- K_1 offset phases: we evaluate this systematic effect by means of MC simulated experiments. Signal events are generated from a model in which we set $\delta_i = 0$. A fit is performed with the nominal model and the observed bias is assumed as a systematic uncertainty.
- K_1 intermediate resonances: we evaluate a systematic uncertainty related to the parameterization of the intermediate resonances in K_1 decay. This is done by means of MC simulated experiments. Signal events are generated from a model in which we replace the $K^*(1430)$ Breit-Wigner lineshape with a $K\pi$ S-wave LASS parameterization [102], while the fit is performed with the nominal model.

- K^*/ρ bands: we test the stability of the fit results against variations in the selection of the "K^*" and "ρ bands," and evaluate a corresponding systematic error.

- Peaking $B\overline{B}$ background: an additional systematic uncertainty originates from potential peaking $B\overline{B}$ background, including $B \to K_2^*(1430)\pi$ and $B \to K^*(1680)\pi$, and is evaluated by introducing the corresponding components in the definition of the likelihood and repeating the fit with their yields fixed to values estimated from the available experimental information (Sec. 5.3).

- Fixed background yields: we vary the yields of the $B^0 \to a_1(1260)^{\pm}\pi^{\mp}$ and $B^0 \to D^-_{K^+\pi^-\pi^-}\pi^+$ (for the B^0 modes) and $B^+ \to K^{*+}\rho^0$ (for the B^+ modes) event categories by their uncertainties and take the resulting change in results as a systematic error.

The above systematic uncertainties do not scale with the event yield and are included in the calculation of the significance of the result.

5.8.2 Systematic uncertainty due to interference

In this section we outline the procedure to estimate the systematic uncertainty due to the interference between the $B \to K_1\pi$ and the charmless nonresonant component.

We perform simulated fits to Monte Carlo samples generated according to the results of the likelihood scans. The relative fractions of the squared amplitudes for B meson decays into signal and $B \to K^*\pi\pi + \rho K\pi$ final states are fixed to the values extracted from the nominal fit. The overall phases and relative contribution for the $K^*\pi\pi$ and $\rho K\pi$ interfering states are assumed to be constant across phase space and are generated between zero and a maximum value using uniform prior distributions. Since we are assuming that all the fitted non-resonant contribution interferes, and that the $K^*\pi\pi$ and $\rho K\pi$ phases are constant across the phase space, we expect the estimated systematic uncertainty to be conservative.

We calculate the systematic uncertainty from the RMS variation of the average signal branching fraction and production parameters. This uncertainty is assumed to scale as the square root of the signal branching fraction and does not affect the significance.

5.8.3 Multiplicative uncertainties

The systematic uncertainties in efficiencies include those associated with track finding, particle identification and, for the B^+ modes, K^0_S reconstruction. Other systematic effects arise from event selection criteria, such as track multiplicity and thrust angle, and the number of B mesons.

- MC statistics: this systematic error is the statistical error on the efficiency due to the finite size of the Monte Carlo samples used for its evaluation, and amounts to 1%.

- PID: we have evaluated the systematic error due to PID vetoes. For the B^0 modes we assign an uncertainty of 2.9%, based on $B^0 \to D^-(K^+\pi^-\pi^-)\pi^+$ control sample studies, while for the B^+ modes we evaluate an uncertainty of 3.1%, based on $B^+ \to D^0(K^0_S\pi^+\pi^-)\pi^+$ control sample studies.

- Track finding efficiency: we assign a 0.236% systematic uncertainty per track, resulting in a total error of 1% for the neutral modes and 0.8% for the charged modes: this evaluation is based on efficiency studies, performed by the *BABAR* Collaboration, in $\tau^+\tau^-$ events with 3-prong - 1-prong topology.

- K_S reconstruction: this systematic error is calculated according to efficiency tables provided by the *BABAR* Collaboration for the most common K^0_S selection cuts and based on studies of the $B \to c\bar{c}K^0_S$ decays. These tables parameterize efficiency corrections to the Monte Carlo as a function of the transverse flight length, the polar angle in the laboratory, and the transverse momentum of a K^0_S particle.

- $\cos\theta_{\rm T}$: a systematic uncertainty of 1% is assigned looking at the variation of the shape of signal MC events before and after the $\cos\theta_{\rm T}$ cut.

- Track multiplicity: we have requested the reconstruction of at least 5 charged tracks in the event. Signal MC inefficiency for this cut is about 2%. We assign an uncertainty of 1%.

- Number of $B\overline{B}$ pairs: the B counting group recommends a systematic uncertainty of 1.1%.

Table 5.7: Estimates of systematic errors, evaluated at the absolute minimum of each $-\ln\mathcal{L}$ scan. For the branching fraction, the errors labeled (A), for additive, are given in units of 10^{-6}, while those labeled (M), for multiplicative, are given in percentage.

	$B^0 \to K_1^+\pi^-$			$B^+ \to K_1^0\pi^+$	
Quantity	$\mathcal{B}$	ϑ	ϕ	$\mathcal{B}$	ϑ
PDF parameters (A)	0.8	0.01	0.15	1.4	0.07
MC/data correction (A)	0.8	0.00	0.01	1.0	0.02
ML fit bias (A)	0.6	0.03	0.02	2.0	0.08
Fixed phase (A)	–	–	–	0.6	0.06
Scan (A)	0.9	0.04	0.16	0.0	0.04
K_1 $K-$matrix parameters (A)	2.2	0.01	0.36	0.5	0.05
K_1 offset phases (A)	0.2	0.01	0.02	0.0	0.00
K_1 intermediate resonances (A)	0.5	0.00	0.06	0.2	0.02
K^*/ρ bands (A)	0.2	0.05	0.00	1.2	0.05
Peaking $B\overline{B}$ bkg (A)	0.8	0.01	0.13	1.0	0.01
Fixed background yields (A)	0.0	0.00	0.00	0.4	0.02
Interference (A)	6.0	0.25	0.52	10.6	0.43
MC statistics (M)	1.0	–	–	1.0	–
Particle identification (M)	2.9	–	–	3.1	–
Track finding (M)	1.0	–	–	0.8	–
K^0_S reconstruction (M)	–	–	–	1.6	–
$\cos\theta_{\rm T}$(M)	1.0	–	–	1.0	–
Track multiplicity (M)	1.0	–	–	1.0	–
Number $B\overline{B}$ pairs (M)	1.1	–	–	1.1	–

5.9 Branching fraction results

We derive the probability distributions for the $B \to K_1(1270)\pi + K_1(1400)\pi$, $B \to K_1(1270)\pi$, $B \to K_1(1400)\pi$, and $B \to K_{1A}\pi$ branching fractions by means of an averaging procedure, that takes into account the dependence of the results of the fit on ϑ and ϕ. For the B^+ modes, since the ϕ parameter is not a free parameter in the fit, the probability distribution in ϕ is assumed to be flat, i.e., we set $P(\vartheta, \phi) = P(\vartheta, \pi)$; in addition, we set $\mathcal{L}(\mathcal{B}'; \vartheta, \phi) = \mathcal{L}(\mathcal{B}; \vartheta, \pi)$, where $\mathcal{B}' = \mathcal{B} \times \epsilon_1(\vartheta, \pi)/\epsilon_1(\vartheta, \phi)$.

At each point in the $\boldsymbol{\zeta}$ plane we calculate the distributions for the branching fractions, given by $f(\mathcal{B}; \boldsymbol{\zeta}) = c\mathcal{L}(\mathcal{B}; \boldsymbol{\zeta})$, where c is a normalization constant. Systematics are included by convolving the experimental one-dimensional likelihood $\mathcal{L}(\mathcal{B}; \boldsymbol{\zeta})$ with a Gaussian function that represents systematic uncertainties. The width $\sigma_{\rm sys}$ of the Gaussian function depends on the branching fraction according to the relation

$$\sigma^2_{\rm sys}(x) = \sigma^2_A + \sigma^2_I x + \sigma^2_M x^2, \tag{5.9}$$

where $x = \mathcal{B}/\mathcal{B}_{\rm max}$, and $\mathcal{B}_{\rm max}$ is the branching fraction value that maximizes $\mathcal{L}$. In the above expression, σ_A represents the additive systematic uncertainties, except the contribution due to interference (σ_I), while σ_M represents the multiplicative uncertainties; σ_A, σ_M, and σ_I are evaluated for $\mathcal{B} = \mathcal{B}_{\rm max}$, as described in Sec. 5.8.

The branching fraction results are obtained by means of a weighted average of the branching fraction distributions defined above, with weights calculated from the experimental two-dimensional likelihood for ϑ and ϕ (Fig. 5.14).

For each point of the $\boldsymbol{\zeta}$ scan, the $B \to K_1(1270)\pi$, $B \to K_1(1400)\pi$, and $B \to K_{1A}\pi$ branching fractions are obtained by applying $\boldsymbol{\zeta}$-dependent correction factors (Sec. 5.9.1) to the combined $B \to K_1(1270)\pi + K_1(1400)\pi$ branching fraction associated with that $\boldsymbol{\zeta}$ point.

From the resulting distributions $f(\mathcal{B})$ we calculate the corresponding two-sided intervals at 68% probability, which consist of all the points $\mathcal{B} > 0$ that satisfy the condition $f(\mathcal{B}) > x$, where x is such that $\int_{f(\mathcal{B})>x,\ \mathcal{B}>0} f(\mathcal{B})\mathrm{d}\mathcal{B} = 68\%$. The upper limits (UL) at 90% probability are calculated as $\int_{0<\mathcal{B}<UL} f(\mathcal{B})\mathrm{d}\mathcal{B} = 90\%$. The results are summarized in Table 5.8 (statistical only) and Table 5.9 (including systematics).

We measure $\mathcal{B}(B^0 \to K_1(1270)^+\pi^- + K_1(1400)^+\pi^-) = 3.1^{+0.8}_{-0.7} \times 10^{-5}$ and $\mathcal{B}(B^+ \to K_1(1270)^0\pi^+ + K_1(1400)^0\pi^+) = 2.9^{+2.9}_{-1.7} \times 10^{-5}$ ($< 8.2 \times 10^{-5}$), where the two-sided ranges and upper limits are evaluated at 68% and 90% probability, respectively, and include systematic uncertainties.

5.9.1 Calculation of the correction factors

When dealing with interfering resonances, it is difficult to disentangle the individual contributions to the branching fraction. It is possible to gain some insight in this problem by considering a K-matrix model comprised of two resonances and a single decay channel (e.g., $i = 1$). If the mass poles are far apart relative to the widths, then the matrix K is dominated either by the first or the second resonance, and the total amplitude can be expressed as a sum of Breit-Wigner amplitudes:

$$F \approx \frac{f_{pa} f_{a1}}{(M_a - M) - i\rho_1 f^2_{a1}} + \frac{f_{pb} f_{b1}}{(M_b - M) - i\rho_1 f^2_{b1}}. \tag{5.10}$$

Table 5.8: Branching fraction results for $B \to K_1\pi$ decays, in units of 10^{-5}, and corresponding confidence levels (C.L., statistical uncertainties only). For each branching fraction we provide the mean of the probability distribution, the most probable value (MPV), the two-sided interval at 68% probability, and the upper limit at 90% probability.

Channel	Mean	MPV	68% C.L. interval	90% C.L. UL
$B^0 \to K_1(1270)^+\pi^- + K_1(1400)^+\pi^-$	3.2	3.1	$(2.9, 3.4)$	3.5
$B^0 \to K_1(1270)^+\pi^-$	1.7	1.6	$(1.3, 2.0)$	2.1
$B^0 \to K_1(1400)^+\pi^-$	1.6	1.6	$(1.3, 1.9)$	2.0
$B^0 \to K_{1A}^+\pi^-$	1.5	1.4	$(1.0, 1.9)$	2.2
$B^+ \to K_1(1270)^0\pi^+ + K_1(1400)^0\pi^+$	2.9	2.3	$(1.6, 3.5)$	4.5
$B^+ \to K_1(1270)^0\pi^+$	1.1	0.3	$(0.0, 1.4)$	2.5
$B^+ \to K_1(1400)^0\pi^+$	1.8	1.7	$(1.0, 2.5)$	2.0
$B^+ \to K_{1A}^0\pi^+$	1.1	0.2	$(0.0, 1.5)$	2.3

Table 5.9: Branching fraction results for $B \to K_1\pi$ decays, in units of 10^{-5}, and corresponding confidence levels (C.L., systematic uncertainties included). For each branching fraction we provide the mean of the probability distribution, the most probable value (MPV), the two-sided interval at 68% probability, and the upper limit at 90% probability.

Channel	Mean	MPV	68% C.L. interval	90% C.L. UL
$B^0 \to K_1(1270)^+\pi^- + K_1(1400)^+\pi^-$	3.3	3.1	$(2.4, 3.9)$	4.3
$B^0 \to K_1(1270)^+\pi^-$	1.7	1.7	$(0.6, 2.5)$	3.0
$B^0 \to K_1(1400)^+\pi^-$	1.6	1.7	$(0.8, 2.4)$	2.7
$B^0 \to K_{1A}^+\pi^-$	1.6	1.4	$(0.4, 2.3)$	2.9
$B^+ \to K_1(1270)^0\pi^+ + K_1(1400)^0\pi^+$	4.6	2.9	$(1.2, 5.8)$	8.2
$B^+ \to K_1(1270)^0\pi^+$	1.7	0.0	$(0.0, 2.1)$	4.0
$B^+ \to K_1(1400)^0\pi^+$	2.0	1.6	$(0.0, 2.5)$	3.9
$B^+ \to K_{1A}^0\pi^+$	1.6	0.2	$(0.0, 2.1)$	3.6

The problem becomes more complicated if the resonances lie nearby, when the above expression is not strictly valid. In this case, the total amplitude is again a sum of Breit-Wigner amplitudes:

$$F = \frac{f_{pa}f_{a1}}{(M_a - M) - i\rho_1\left[f_{a1}^2 + f_{b1}^2\left(\frac{M_a - M}{M_b - M}\right)\right]} + \frac{f_{pb}f_{b1}}{(M_b - M) - i\rho_1\left[f_{b1}^2 + f_{a1}^2\left(\frac{M_b - M}{M_a - M}\right)\right]}, \quad (5.11)$$

where the widths have been modified by the unitarity constraint: $\Gamma_a \mapsto \Gamma_a + \Gamma_b\left(\frac{M_a - M}{M_b - M}\right)$.

We work out our approach from the analogy of Eq. 5.11 with Eq. 5.10, based on the linearity of the amplitude F in the P-vector elements

$$P_i = \frac{f_{pa}f_{ai}}{M_a - M} + \frac{f_{pb}f_{bi}}{M_b - M}. \quad (5.12)$$

The correction factors for the production of the $K_1(1270)$ ($K_1(1400)$) resonance only is therefore obtained by subtracting the M_a (M_b) pole from the P-vector.

Similarly, we define the production amplitudes for the K_{1A} (f_{pA}) and K_{1B} (f_{pB}) as [86]:

$$\begin{aligned} f_{pA} &= f_{pa}\cos\theta_K - f_{pb}\sin\theta_K, \\ f_{pB} &= f_{pa}\sin\theta_K + f_{pb}\cos\theta_K. \end{aligned} \tag{5.13}$$

or, equivalently,

$$\begin{aligned} f_{pa} &= f_{pA}\cos\theta_K + f_{pB}\sin\theta_K, \\ f_{pb} &= -f_{pA}\sin\theta_K + f_{pB}\cos\theta_K. \end{aligned} \tag{5.14}$$

The correction factor for the production of K_{1A} or K_{1B} only is thus calculated by subtracting a suitable linear combination of the M_a and M_b poles from the P-vector. No other elements of the amplitude is modified in this calculation.

To summarize, these are the replacements that we introduce in the K-matrix model to describe the production of only one of the following resonances:

- $K_1(1270)$: $P_i \mapsto P'_i = P_i - \dfrac{f_{pa}f_{ai}}{M_a - M}$.
- $K_1(1400)$: $P_i \mapsto P'_i = P_i - \dfrac{f_{pb}f_{bi}}{M_b - M}$.
- K_{1A}: $P_i \mapsto P'_i = P_i - \left[\sin\theta_K \dfrac{f_{pB}f_{ai}}{M_a - M} + \cos\theta_K \dfrac{f_{pB}f_{bi}}{M_b - M}\right]$.
- K_{1B}: $P_i \mapsto P'_i = P_i - \left[\cos\theta_K \dfrac{f_{pA}f_{ai}}{M_a - M} - \sin\theta_K \dfrac{f_{pA}f_{bi}}{M_b - M}\right]$.

Equivalently, we can express the above replacement in terms of a redefinition of the production parameters $(f_{pa}, f_{pb}) \mapsto (f'_{pa}, f'_{pb})$, i.e., $P' = \frac{f'_{pa}f'_{ai}}{M_a - M} - \frac{f'_{pb}f'_{bi}}{M_b - M}$:

- $K_1(1270)$: $(f_{pa}, f_{pb}) \mapsto (0, e^{i\phi}\sin\vartheta)$.
- $K_1(1400)$: $(f_{pa}, f_{pb}) \mapsto (\cos\vartheta, 0)$.
- K_{1A}: $(f_{pa}, f_{pb}) \mapsto (|f_{pA}|\cos\theta_K, -|f_{pA}|\sin\theta_K)$.
- K_{1B}: $(f_{pa}, f_{pb}) \mapsto (|f_{pB}|\sin\theta_K, |f_{pB}|\cos\theta_K)$.

Each individual branching fraction $\mathcal{B}'$ is then calculated, at each point in the scan over $\boldsymbol{\zeta}$, as

$$\mathcal{B}'(\boldsymbol{\zeta}) \equiv \mathcal{B}(\boldsymbol{\zeta}) \frac{\sum_i \int |A'_i(\boldsymbol{\zeta})|^2 d\Phi_i}{\sum_i \int |A_i(\boldsymbol{\zeta})|^2 d\Phi_i}, \tag{5.15}$$

where $\mathcal{B}$ is the combined branching fraction, the index i runs over all isospin configurations of the final state particles, and the integration over the four-particle phase space can be performed by reweighting the signal MC samples. Here we have indicated with A_i the total $B \to K_1\pi$ amplitude calculated with the nominal form $\mathbf{P}$ of the P-vector (Sec. 3.5), and with A'_i the amplitude obtained by replacing $\mathbf{P}$ with $\mathbf{P}'$. The two-dimensional distributions of the $B \to K_{1A}\pi$ and $B \to K_{1B}\pi$ branching fractions over the space spanned by $\boldsymbol{\zeta}$ are shown in Fig. 5.17 and Fig. 5.18, respectively.

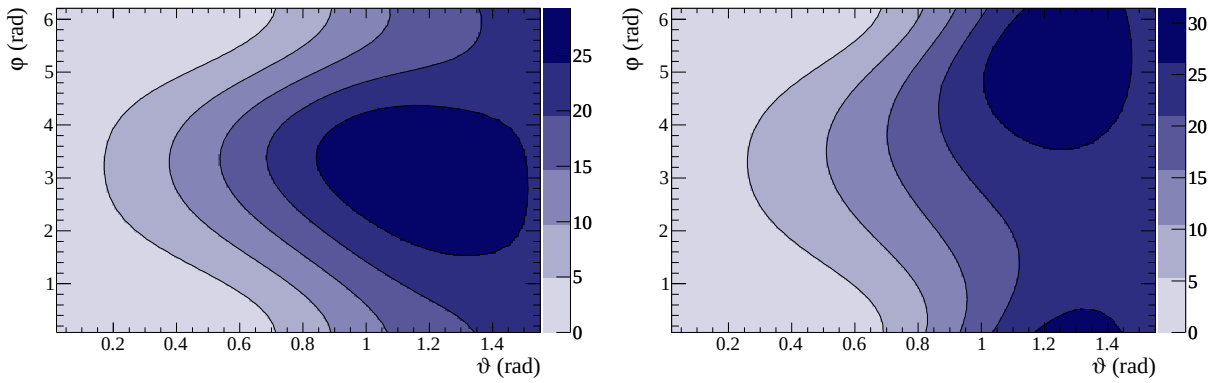

Figure 5.17: $B^0 \to K^+_{1A}\pi^-$ (left) and $B^+ \to K^0_{1A}\pi^+$ (right) branching fractions as a function of ϑ and ϕ.

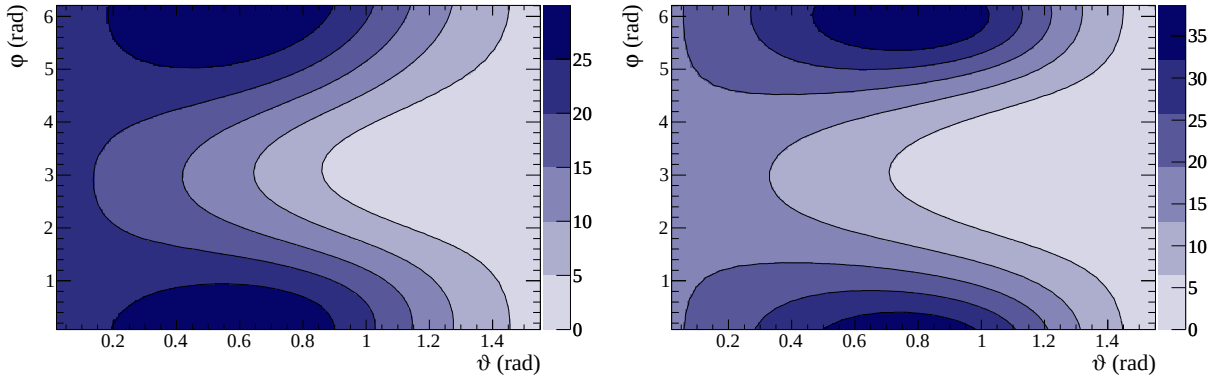

Figure 5.18: $B^0 \to K^+_{1B}\pi^-$ (left) and $B^+ \to K^0_{1B}\pi^+$ (right) branching fractions as a function of ϑ and ϕ.

As done for the combined branching fraction, the final results for the individual branching fractions are obtained by means of a weighted average over $\boldsymbol{\zeta}$, with weights calculated from the experimental two-dimensional likelihood for ϑ and ϕ.

Including systematic uncertainties we obtain the two-sided intervals (in units of 10^{-5}): $\mathcal{B}(B^0 \to K_1(1270)^+\pi^-) \in [0.6, 2.5]$, $\mathcal{B}(B^0 \to K_1(1400)^+\pi^-) \in [0.8, 2.4]$, $\mathcal{B}(B^0 \to K^+_{1A}\pi^-) \in [0.4, 2.3]$, $\mathcal{B}(B^+ \to K_1(1270)^0\pi^+) \in [0.0, 2.1]$ (< 4.0), $\mathcal{B}(B^+ \to K_1(1400)^0\pi^+) \in [0.0, 2.5)$ (< 3.9), $\mathcal{B}(B^+ \to K^0_{1A}\pi^+) \in [0.0, 2.1]$ (< 3.6), where the two-sided ranges and the upper limits are evaluated at 68% and 90% probability, respectively.

5.9.2 Effect of ambiguities on the branching fraction results

We have shown in Sec. 3.4.3 that several degenerate solutions exist for the fit of the K-matrix model to the ACCMOR data. Here we show that the branching fraction results don't depend on these ambiguities, by investigating each of them separately.

Ambiguity 1: $\boldsymbol{\theta_K \mapsto \theta_K + \pi}$, $\boldsymbol{\gamma_\pm \mapsto -\gamma_\pm}$ or $\boldsymbol{\gamma_\pm}$ unchanged

This ambiguity doesn't modify the parameters f_{ai}, f_{bi} (apart from a global change of signs), thus leaving the K-matrix unaltered. Under these transformations, the P-vector may undergo a change of sign, which is irrelevant since we are interested in the squared amplitudes. Therefore, this ambiguity doesn't affect the MC simulation nor does it alter the ratios of integrals that enter the calculation of the branching fractions $\mathcal{B}(B \to K_1(1270)\pi)$, $\mathcal{B}(B \to K_1(1400)\pi)$, $\mathcal{B}(B \to K_{1A}\pi)$, and $\mathcal{B}(B \to K_{1B}\pi)$.

Ambiguity 2: $\boldsymbol{\theta_K \mapsto -\theta_K + \pi}$, $\boldsymbol{\gamma_- \to -\gamma_-}$, $\boldsymbol{f_{pb} \to -f_{pb}}$, $\boldsymbol{\gamma_+}$ unchanged

This transformation reverts the sign of the decay couplings of the $K_1(1270)$ resonance (f_{bi}), while leaving those of the $K_1(1400)$ (f_{ai}) unchanged. This change in the f_{bi} couplings can be compensated by a change in the sign of the f_{pb} production parameter: the amplitude calculated with $\gamma_- = |\gamma_-|$ and $f_{pb} = |f_{pb}|e^{i\phi}$ is identical to the amplitude calculated with $\gamma_- = -|\gamma_-|$, $f_{pb} = |f_{pb}|e^{i(\phi+\pi)}$. The other production parameter (f_{pa}) is unaltered. This is equivalent to a change in sign in f_{pA}, while f_{pB} doesn't change.

The results of the analysis of the B decay data are not affected by any model ambiguity as long as we specify the couplings in the text (i.e., the results on $\boldsymbol{\zeta}$ in this work are obtained with $\gamma_- = |\gamma_-|$). Using the other solution for the decay couplings (i.e., $\gamma_- = -|\gamma_-|$), the extracted values of ϕ would be shifted by π: $\phi \mapsto \phi + \pi$. This leaves the K-matrix and the P-vector unchanged, also when one resonance is "turned off":

- $\dfrac{f_{pa}f_{ai}}{M_a - M} \mapsto \dfrac{f_{pa}f_{ai}}{M_a - M}$.
- $\dfrac{f_{pb}f_{bi}}{M_b - M} \mapsto \dfrac{(-f_{pb})(-f_{bi})}{M_b - M}$.
- $P_i - \left[\sin\theta_K \dfrac{f_{pB}f_{ai}}{M_a - M} + \cos\theta_K \dfrac{f_{pB}f_{bi}}{M_b - M}\right] \mapsto$
$$P_i - \left[\sin(\pi - \theta_K)\dfrac{f_{pB}f_{ai}}{M_a - M} + \cos(\pi - \theta_K)\dfrac{f_{pB}(-f_{bi})}{M_b - M}\right].$$
- $P_i - \left[\cos\theta_K \dfrac{f_{pA}f_{ai}}{M_a - M} - \sin\theta_K \dfrac{f_{pA}f_{bi}}{M_b - M}\right] \mapsto$
$$P_i - \left[\cos(\pi - \theta_K)\dfrac{(-f_{pA})f_{ai}}{M_a - M} - \sin(\pi - \theta_K)\dfrac{(-f_{pA})(-f_{bi})}{M_b - M}\right].$$

This completes the demonstration that the branching fraction results do not depend on which one of the degenerate solutions is chosen for the K-matrix fit.

Chapter 6

Bounds on penguin induced $|\Delta\alpha|$ in $B^0 \to a_1^{\pm}(1260)\pi^{\mp}$

6.1 Experimental input

We use the measurements presented in this work to derive bounds on the model uncertainty $|\Delta\alpha|$ on the weak phase α extracted in $B^0 \to a_1(1260)^{\pm}\pi^{\mp}$ decays. We use the previously measured branching fractions of $B^0 \to a_1(1260)^{\pm}\pi^{\mp}$, $B^0 \to a_1(1260)^{-}K^{+}$ and $B^{+} \to a_1(1260)^{+}K^{0}$ decays [34,35] and the $CP-$violation asymmetries [33] as input to the method of Ref. [36]. The values used are summarized in Tables 6.1 and 6.2.

Table 6.1: Summary of the branching fractions used as input to the calculation of the bounds on $|\Delta\alpha|$ [34, 35].

Decay mode	Branching fraction (in units of 10^{-6})
$B^0 \to a_1(1260)^{\pm}\pi^{\mp}$	$33.2 \pm 3.8 \pm 3.0$
$B^0 \to a_1(1260)^{-}K^{+}$	$16.3 \pm 2.9 \pm 2.3$
$B^{+} \to a_1(1260)^{+}K^{0}$	$34.8 \pm 5.0 \pm 4.4$

Table 6.2: Summary of the values of the $CP-$violation parameters used as input to the calculation of the bounds on $|\Delta\alpha|$ [33].

Quantity	Value
$\mathcal{A}_{CP}^{a_1\pi}$	$-0.07 \pm 0.07 \pm 0.02$
S	$0.37 \pm 0.21 \pm 0.07$
ΔS	$-0.14 \pm 0.21 \pm 0.06$
C	$-0.10 \pm 0.15 \pm 0.09$
ΔC	$0.26 \pm 0.15 \pm 0.07$

The bounds are calculated as the average of $|\Delta\alpha^{+}| = |\alpha_{\rm eff}^{+} - \alpha|$ and $|\Delta\alpha^{-}| = |\alpha_{\rm eff}^{-} - \alpha|$,

Table 6.3: Correlation matrix (stat.) from the *BABAR* TD fit [98].

	$\mathcal{A}_{CP}^{a_1\pi}$	S	ΔS	C	ΔC
$\mathcal{A}_{CP}^{a_1\pi}$	1.00	0.00	0.00	0.00	0.00
S	0.00	1.00	−0.01	−0.03	0.00
ΔS	0.00	−0.01	1.00	0.01	−0.02
C	0.00	−0.03	0.01	1.00	−0.11
ΔC	0.00	0.00	−0.02	−0.11	1.00

which are obtained from the inversion of the relations [36], rederived in Sec. 1.6:

$$\cos 2(\alpha_{\rm eff}^{\pm} - \alpha) \geq \frac{1 - 2R_{\pm}^0}{\sqrt{1 - \mathcal{A}_{CP}^{\pm\,2}}}, \quad \cos 2(\alpha_{\rm eff}^{\pm} - \alpha) \geq \frac{1 - 2R_{\pm}^+}{\sqrt{1 - \mathcal{A}_{CP}^{\pm\,2}}}. \tag{6.1}$$

$$R_+^0 \equiv \frac{\bar\lambda^2 f_{a_1}^2 \bar{\mathcal{B}}(K_{1A}^+\pi^-)}{f_{K_{1A}}^2 \bar{\mathcal{B}}(a_1^+\pi^-)}, \qquad R_-^0 \equiv \frac{\bar\lambda^2 f_\pi^2 \bar{\mathcal{B}}(a_1^- K^+)}{f_K^2 \bar{\mathcal{B}}(a_1^-\pi^+)},$$
$$R_+^+ \equiv \frac{\bar\lambda^2 f_{a_1}^2 \bar{\mathcal{B}}(K_{1A}^0\pi^+)}{f_{K_{1A}}^2 \bar{\mathcal{B}}(a_1^+\pi^-)}, \qquad R_-^+ \equiv \frac{\bar\lambda^2 f_\pi^2 \bar{\mathcal{B}}(a_1^+ K^0)}{f_K^2 \bar{\mathcal{B}}(a_1^-\pi^+)},$$

For the constant $\bar\lambda = |V_{us}|/|V_{ud}| = |V_{cd}|/|V_{cs}|$ we take the value 0.23 [5]. The decay constants $f_K = 155.5 \pm 0.9$ MeV and $f_\pi = 130.4 \pm 0.2$ MeV [5] are experimentally known with small uncertainties.

For the decay constants of the a_1 and K_{1A} mesons the values $f_{a_1} = 203 \pm 18$ MeV [103] and $f_{K_{1A}} = 207$ MeV [72] are used. Because of the large width of the $a_1(1260)$ resonance, it is difficult to represent its coupling to the weak currents in terms of a single decay constant. As a cross check, the value $f_{a_1} = 203 \pm 18$ MeV, obtained from the analysis of the a_1 meson production in τ decays [103], is therefore compared to the values calculated using different methods, such as QCD sum rules ($f_{a_1} = 238 \pm 10$ MeV) [104] and $SU(3)$ relations using $f_{K_1(1270)}$ as an input ($f_{a_1} = 215 - 223$ MeV) [105]. These values are in good agreement.

From the rates of $\tau \to K\pi\pi\nu$ decays [47] it is possible to derive the value of the decay constant of the $K_1(1270)$ meson, $|f_{K_1(1270)}| = 175 \pm 19$ MeV [106]. The value of $f_{K_{1A}}$ is calculated from the quark model, using $|f_{K_1(1270)}|$ and $f_{a_1} = 203 \pm 18$ MeV as input [61]. This value depends on the mixing angle assumed, and reference values are given in Ref. [72] for two positive θ_K values, $\theta_K = 58^\circ$ ($f_{K_{1A}} = 207$ MeV) and $\theta_K = 37^\circ$ ($f_{K_{1A}} = 293$ MeV), where the authors of Ref. [72] use the measurement of the branching fractions of B decays to $K_1(1270)\gamma$ to determine the sign of θ_K ($\theta_K > 0$). Since $f_{K_{1A}}$ is not available for $\theta_K = 72^\circ$ (the value used in the rest of the analysis, see Table 3.3), in the following we use the value of $f_{K_{1A}}$ corresponding to a mixing angle $\theta_K = 58^\circ$ [72], and we assume an uncertainty of 20 MeV on $f_{K_{1A}}$. Incidentally, assuming $\theta_K = 58^\circ$ instead of $\theta_K = 37^\circ$ is a conservative choice for the determination of the bounds on $\Delta\alpha$, since $f_{K_{1A}}(-58^\circ) \ll f_{K_{1A}}(-37^\circ)$ and a lower $f_{K_{1A}}$ results in higher bounds on $\Delta\alpha$. Under a change of sign in θ_K, the main effect on the form factors is a change in sign of $f_{K_1(1270)}$, while the sign of $f_{K_1(1400)}$ is unchanged. Since $f_{K_{1B}} \ll f_{K_{1A}}$, $m_{K_1(1270)} f_{K_1(1270)} \approx m_{K_{1A}} f_{K_{1A}} \sin\theta_K$ within O(10%) effects. Using naïve arguments based on SU(3) relations and the mixing formulae, in Sec. 6.1.1 we verify that the dependence of $f_{K_{1A}}$ on the mixing angle is rather mild in the θ_K range $[58, 72]^\circ$.

6.1.1 Variation of the decay constant with the mixing angle

We check, using symmetry arguments, that the dependence of f_{K1A} on the mixing angle is mild in the θ_K range $[58, 72]^\circ$ and that assuming an uncertainty of 20 MeV is reasonable.

We use the following relations, based on the Gell-Mann-Okubo mass formula and on the mixing relations (3.1):

$$m_A = \sqrt{m^2_{K_1(1400)} \cos^2\theta_K + m^2_{K_1(1270)} \sin^2\theta_K}, \tag{6.2}$$

$$m_B = \sqrt{m^2_{K_1(1400)} \sin^2\theta_K + m^2_{K_1(1270)} \cos^2\theta_K}, \tag{6.3}$$

with $m_{K_1(1400)} = 1.400$ GeV and $m_{K_1(1270)} = 1.270$ GeV.

The transformation properties of the strange weak axial-vector current under charge conjugation in the SU(3) limit [59] imply $f_{K_{1B}} = 0$, and result in:

$$\frac{f_{K_1(1400)} m_{K_1(1400)}}{f_{K_1(1270)} m_{K_1(1270)}} = -\frac{\cos\theta_K}{\sin\theta_K}. \tag{6.4}$$

SU(3) breaking can flip the SU(3) charge conjugation property of the strange weak current, and the effect on the above expression can be parameterized by the introduction of a parameter δ [106]:

$$f_{K_1(1400)} = f_{K_1(1270)} \frac{m_{K_1(1270)}}{m_{K_1(1400)}} \left(-\frac{\cos\theta_K - \delta \sin\theta_K}{\sin\theta_K + \delta \cos\theta_K} \right), \tag{6.5}$$

with $|\delta| = \dfrac{m_s - m_u}{\sqrt{2}(m_s + m_u)} = 0.18$. For $\theta_K = 72^\circ$, τ-decay data favors $\delta = -0.18$ [106] (Fig. 6.1).

Finally, from the mixing relations, one obtains [72]

$$f_{K_{1A}} = -\frac{1}{m_A}(f_{K_1(1270)} m_{K_1(1270)} \sin\theta_K + f_{K_1(1400)} m_{K_1(1400)} \cos\theta_K). \tag{6.6}$$

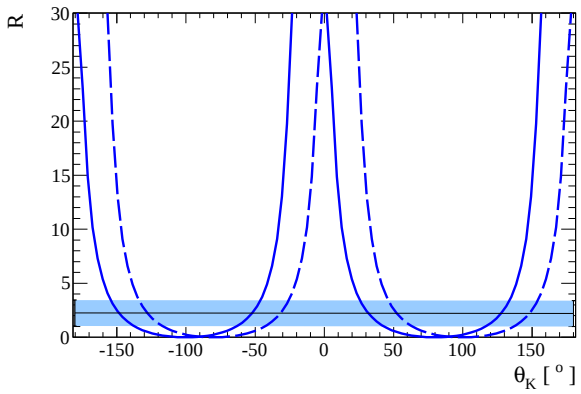

Figure 6.1: Ratio of decay rates of the K1 resonances $R \equiv \frac{\mathcal{B}(\tau \to K_1(1270)\nu)}{\mathcal{B}(\tau \to K_1(1400)\nu)} = 2.2 \pm 1.2$ (light shaded band). Curves report the broken SU(3) model prediction $R = \left| \frac{\sin\theta_K + \delta\cos\theta_K}{\cos\theta_K - \delta\sin\theta_K} \right|^2 \times \Phi$ for $\delta = -18$ (dashed) and $\delta = 18$ (solid). The factor $\Phi = 1.8$ [59] accounts for phase space and other kinematical corrections.

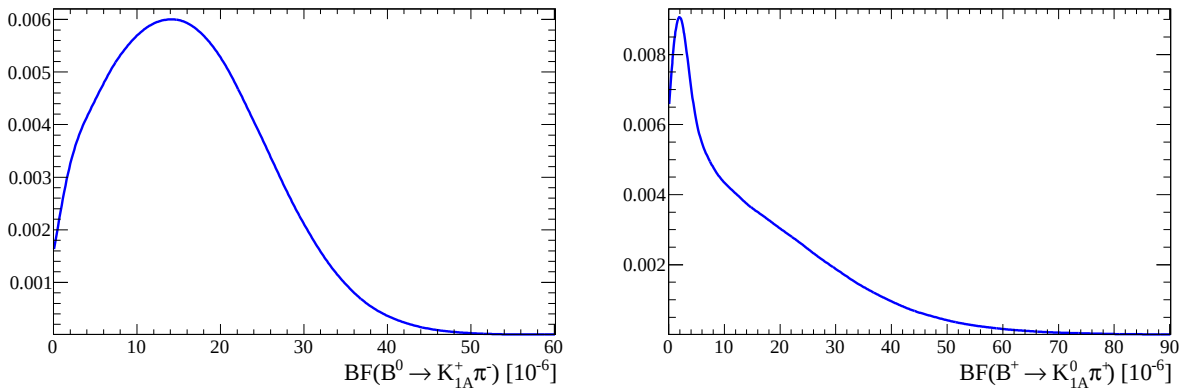

Figure 6.2: Probability distributions for $B^0 \to K_{1A}^+\pi^-$ (left) and $B^+ \to K_{1A}^0\pi^+$ (right) branching fractions, extracted from the results of the analysis reported in this work.

Using $f_{K_1(1270)} = -175$ MeV as an input, we calculate the values of $f_{K_1(1400)}$ and $f_{K_{1A}}$ for $\theta_K = 58°$ and $\theta_K = 72°$. The above formulas do not reproduce the value $f_{K_{1A}} = 207$ MeV at $\theta_K = 58°$, but provide an estimate of the dependence of $f_{K_{1A}}$ on θ_K. We obtain $f_{K_1(1400)} = 85$ MeV, $f_{K_{1A}} = 193$ MeV at $\theta_K = 72°$, and $f_{K_1(1400)} = 144$ MeV, $f_{K_{1A}} = 226$ MeV at $\theta_K = 58°$.

6.2 Extraction of the bounds

We use a Monte Carlo technique to estimate a probability region for the bound on $|\alpha_{\rm eff} - \alpha|$. All the CP-averaged rates and CP-violation parameters participating in the estimation of the bound are generated according to the experimental distributions, taking into account the statistical correlations among $\mathcal{A}_{CP}^{a_1\pi}$, C, and ΔC [8].

We generate several sets of the experimental parameters according to the following distributions:

- $\bar{B}(a_1^{\pm}\pi^{\mp})$ gaussian;
- $\mathcal{A}_{CP}^{a_1\pi}$: gaussian;
- $S, \Delta S, C, \Delta C$: four dimensional gaussian, taking into account correlations;
- $\bar{B}(a_1^- K^+)$: gaussian;
- $\bar{B}(a_1^+ K^0)$: gaussian;
- $\bar{B}(K_{1A}^+\pi^-)$: non parametric distribution, shown in Fig. 6.2 (left);
- $\bar{B}(K_{1A}^0\pi^+)$: non parametric distribution, shown in Fig. 6.2 (right).

For each set of generated values we solve the system of inequalities in Eq. (6.1), which involve $|\alpha_{\rm eff}^+ - \alpha|$ and $|\alpha_{\rm eff}^- - \alpha|$, and we calculate a bound on $|\alpha_{\rm eff} - \alpha|$ from

$$|\alpha_{\rm eff} - \alpha| \leq (|\alpha_{\rm eff}^+ - \alpha| + |\alpha_{\rm eff}^- - \alpha|)/2. \tag{6.7}$$

The probability regions are obtained by a counting method: we estimate the fraction of experiments for which the extracted bound on $|\alpha_{\rm eff} - \alpha|$ is greater than a given value. The distributions for the upper bounds on $|\alpha^+_{\rm eff} - \alpha|$ and $|\alpha^-_{\rm eff} - \alpha|$ are shown in Fig 6.3, and correspond to

$$|\alpha^+_{\rm eff} - \alpha| < 10^\circ \text{ at } 68\% \text{ CL}, \qquad |\alpha^+_{\rm eff} - \alpha| < 13^\circ \text{ at } 90\% \text{ CL, and} \tag{6.8}$$

$$|\alpha^-_{\rm eff} - \alpha| < 13^\circ \text{ at } 68\% \text{ CL}, \qquad |\alpha^-_{\rm eff} - \alpha| < 15^\circ \text{ at } 90\% \text{ CL}. \tag{6.9}$$

For the overall bound we obtain (Fig. 6.4)

$$|\alpha_{\rm eff} - \alpha| < 11^\circ \text{ at } 68\% \text{ CL}, \qquad |\alpha_{\rm eff} - \alpha| < 13^\circ \text{ at } 90\% \text{ CL}. \tag{6.10}$$

In a similar way we derive limits on the penguin-to-tree ratios $r_\pm$, by solving the relevant system of inequalities for each set of generated values. We obtain

$$0.15 < r_+ < 0.28 \text{ at } 68\% \text{ CL}, \qquad 0.11 < r_+ < 0.37 \text{ at } 90\% \text{ CL}, \tag{6.11}$$

$$0.23 < r_- < 0.39 \text{ at } 68\% \text{ CL}, \qquad 0.21 < r_- < 0.47 \text{ at } 90\% \text{ CL}. \tag{6.12}$$

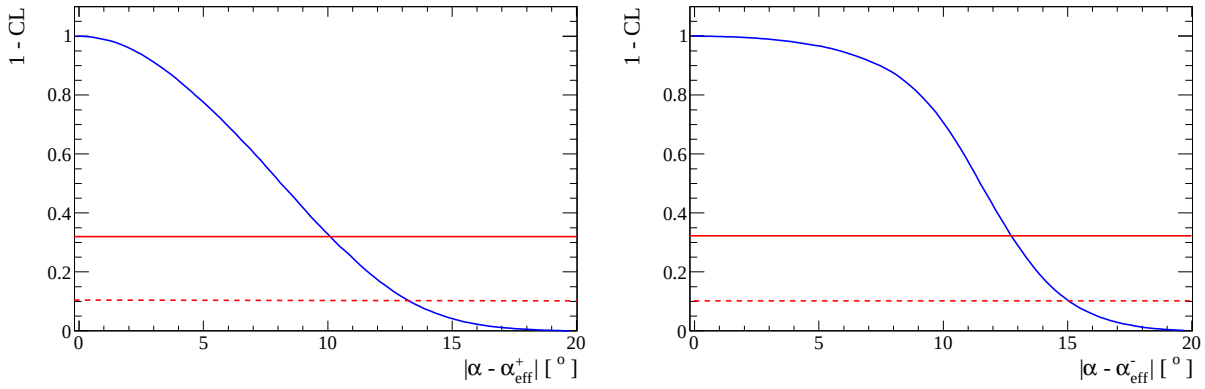

Figure 6.3: $1 - CL$ distribution of the upper bound on $|\Delta\alpha^+|$ (left) and $|\Delta\alpha^-|$ (right).

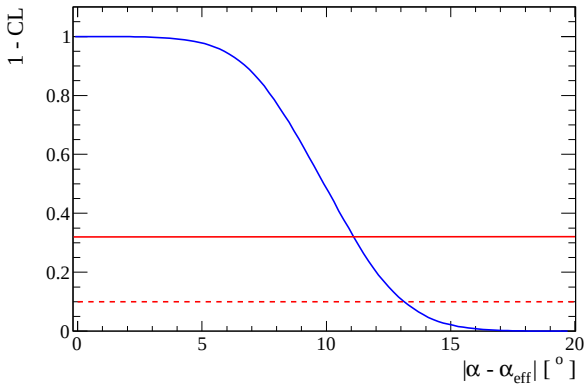

Figure 6.4: $1 - CL$ distribution of the upper bound on $|\Delta\alpha|$.

6.2.1 Effect of additional sources of SU(3) breaking

We study the effect of additional nonfactorizable sources of SU(3) breaking, by introducing positive parameters $0.7 \le c_\pm \le 1.3$, and writing $p'_\pm = -c_\pm \overline{\lambda}^{-1} p_\pm$, where p' is the penguin amplitude in $\Delta S = 1$ transitions [30].

$$r_\pm = \frac{\sqrt{(R^0_\pm + c^2_\pm \overline{\lambda}^2_\pm)^2 z^2_\pm + (c^2_\pm - R^0_\pm)(R^0_\pm - \overline{\lambda}^4_\pm)} - (R^0_\pm + c^2_\pm \overline{\lambda}^2_\pm) z_\pm}{c^2_\pm - R^0_\pm}, \tag{6.13}$$

$$= \frac{\sqrt{{R^+_\pm}^2 z^2_\pm + (c^2_\pm - R^+_\pm) R^+_\pm} - R^+_\pm z_\pm}{c^2_\pm - R^+_\pm}. \tag{6.14}$$

Substituting $R^+_\pm$ in (1.64) it is possible to derive the following inequalities involving $\Delta\alpha^\pm$:

$$\cos 2\Delta\alpha^\pm = \frac{1 - 2c_\pm^{-2} R^+_\pm \sin^2\gamma}{\sqrt{1 - (\mathcal{A}^\pm_{CP})^2}} \ge \frac{1 - 2c_\pm^{-2} R^+_\pm}{\sqrt{1 - (\mathcal{A}^\pm_{CP})^2}}. \tag{6.15}$$

Similar inequalities involving $R^0_\pm$ are derived by noting that

$$\frac{\bar\lambda^2 f^2_{a_1} \bar{\mathcal{B}}(K^+_{1A}\pi^-)}{f^2_{K_{1A}} |p_\pm|^2} = c^2_\pm \left(1 + 2c_\pm^{-1} r_\pm^{-1} \overline{\lambda}^2 z_\pm + c_\pm^{-2} r_\pm^{-2} \overline{\lambda}^4\right) \tag{6.16}$$

and

$$c^2_\pm \left[1 - \cos^2\delta_\pm \cos^2\gamma + (\cos^2\delta_\pm \cos^2\gamma - 2x\cos\delta_\pm \cos\gamma + x^2)\right] \ge c^2_\pm \sin^2\gamma, \tag{6.17}$$

where $x = c_\pm^{-1} r_\pm^{-1} \overline{\lambda}^2$, so that

$$\cos 2\Delta\alpha^\pm \ge \frac{1 - 2c_\pm^{-2} R^0_\pm}{\sqrt{1 - (\mathcal{A}^\pm_{CP})^2}}. \tag{6.18}$$

The results obtained in Sec. 6.2 correspond to the choice $c_\pm = 1$. Assuming that the neglected sources of SU(3) breaking manifest as a 10% or 30% shift (at amplitude level) of the penguin contributions, we repeat the procedure and obtain the distributions in Fig. 6.5 for the bounds on $|\alpha^+_{\rm eff} - \alpha|$ and $|\alpha^-_{\rm eff} - \alpha|$. For $c_\pm = \{0.7, 1.3\}$, the observed shifts in the bounds are of order 3°, which is an $O(r^2_\pm)$ effect.

6.3 Results on the CKM angle α

As seen in Sec. 1.6, the determination of $\alpha_{\rm eff}$ [33] presents an eightfold ambiguity in the range $[0°, 180°]$. The eight solutions are $\alpha_{\rm eff} = (11 \pm 7)°$, $\alpha_{\rm eff} = (41 \pm 7)°$, $\alpha_{\rm eff} = (49 \pm 7)°$, $\alpha_{\rm eff} = (79 \pm 7)°$, $\alpha_{\rm eff} = (101 \pm 7)°$, $\alpha_{\rm eff} = (131 \pm 7)°$, $\alpha_{\rm eff} = (139 \pm 7)°$, $\alpha_{\rm eff} = (169 \pm 7)°$ [33]. Under the assumption that the relative strong phase between the t_- and t_+ tree amplitudes is much less than 90° (valid to leading order in $1/m_b$ [36], and verified in the similar $\rho^\pm\pi^\mp$ channel [30]), it is possible to reduce this ambiguity to a twofold ambiguity in the range $[0°, 180°]$: $\alpha_{\rm eff} = (11 \pm 7)°$, $\alpha_{\rm eff} = (79 \pm 7)°$. We combine the solution near 90°, $\alpha_{\rm eff} = (79 \pm 7)°$ [33], with the bounds on $|\alpha_{\rm eff} - \alpha|$ and estimate the weak phase

$$\alpha = (79 \pm 7 \pm 11)°. \tag{6.19}$$

This solution is consistent with the current average value of α, based on the analysis of $B \to \pi\pi$, $B \to \rho\rho$, and $B \to \rho\pi$ decays [5, 20] (Fig. 6.6).

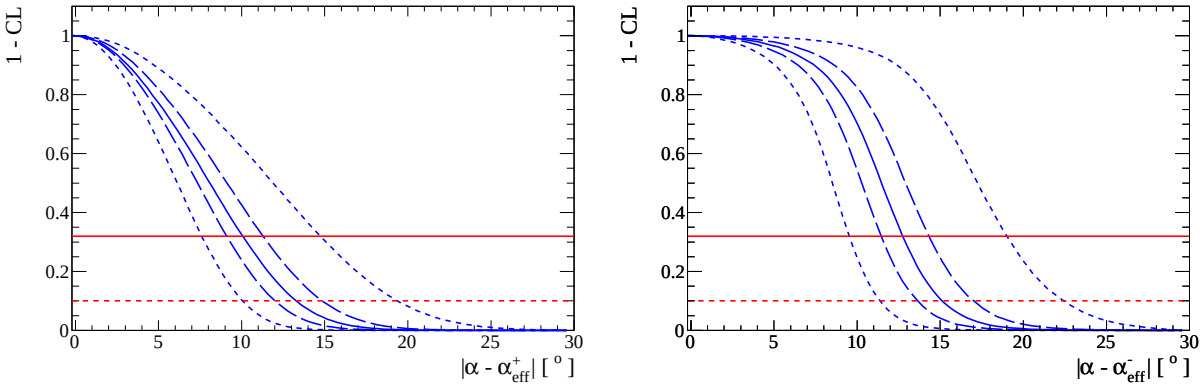

Figure 6.5: $1 - CL$ distribution of the upper bound on $|\Delta\alpha^+|$ (left) and $|\Delta\alpha^-|$ (right), assuming additional sources of SU(3) breaking. Short-dashed: $c_\pm = 0.9$ (right), $c_\pm = 1.1$ (left); long-dashed: $c_\pm = 0.7$ (right), $c_\pm = 1.3$ (left).

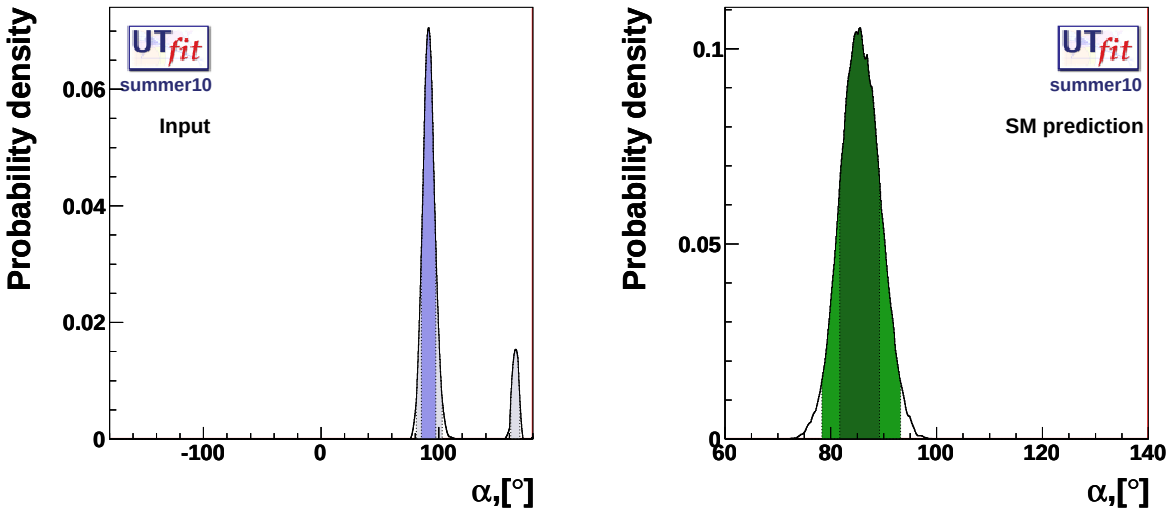

Figure 6.6: Left: input to the SM UT fit for α, from the $\pi\pi$, $\rho\rho$, and $\rho\pi$ channels [20]. Right: prediction for α from the SM UT fit (excluding the input for α) [20].

Conclusions

In this thesis we have presented the branching fraction measurements of charged and neutral B meson decays to $K_1(1270)\pi$ and $K_1(1400)\pi$, obtained from a data sample of 454 million $\Upsilon(4S) \to B\bar{B}$ events. This analysis is particularly challenging from the experimental side since the branching fractions involved are very low, at the level of $10^{-6} - 10^{-7}$, and the signal is characterized by the simultaneous presence of two overlapping resonances, which exhibit sizeable interference effects. The combined $K_1(1270)\pi$ and $K_1(1400)\pi$ signal is therefore modeled with a K-matrix formalism, which accounts for the effects of interference between the $K_1(1270)$ and $K_1(1400)$ mesons by introducing two effective parameters. The model is derived from the analysis, performed by the ACCMOR Collaboration, of the diffractive production of strange mesons.

Including systematic and model uncertainties, we have measured

$$\mathcal{B}(B^0 \to K_1(1270)^+\pi^- + K_1(1400)^+\pi^-) = 3.1^{+0.8}_{-0.7} \times 10^{-5}, \text{ and}$$
$$\mathcal{B}(B^+ \to K_1(1270)^0\pi^+ + K_1(1400)^0\pi^+) = 2.9^{+2.9}_{-1.7} \times 10^{-5} \ (< 8.2 \times 10^{-5}),$$

where the upper limit is calculated at 90% probability. A combined signal for the decays $B^0 \to K_1(1270)^+\pi^-$ and $B^0 \to K_1(1400)^+\pi^-$ is observed for the first time, with a significance of 7.5σ.

By exploiting the physical interpretation of the model in terms of two resonances, that are nearly equal mixtures of SU(3) eigenstates, we distinguish the individual contributions of the $K_1(1270)$ and $K_1(1400)$ resonances to the combined signal, and the following branching fractions are derived for the neutral B meson decays:

$$\begin{aligned} \mathcal{B}(B^0 \to K_1(1270)^+\pi^-) &\in [0.6, 2.5] \times 10^{-5}, \text{ and} \\ \mathcal{B}(B^0 \to K_1(1400)^+\pi^-) &\in [0.8, 2.4] \times 10^{-5}, \end{aligned}$$

where the two-sided intervals are evaluated at 68% probability.

A significance of 3.2σ is obtained for $B^+ \to K_1(1270)^0\pi^+ + K_1(1400)^0\pi^+$, and we derive the following two-sided intervals at 68% probability and upper limits at 90% probability:

$$\begin{aligned} \mathcal{B}(B^+ \to K_1(1270)^0\pi^+) &\in [0.0, 2.1] \times 10^{-5} \ (< 4.0 \times 10^{-5}), \text{ and} \\ \mathcal{B}(B^+ \to K_1(1400)^0\pi^+) &\in [0.0, 2.5] \times 10^{-5} \ (< 3.9 \times 10^{-5}). \end{aligned}$$

In the near future, the availability of updated experimental data on K_1 mesons produced in diffractive processes (e.g., data collected with the COMPASS spectrometer at CERN), or in τ and B decays (most notably, $B \to J/\psi K_1$ decays), could lead to a significant reduction of the systematic errors associated to uncertainties in the parameters of the K-matrix. In particular, $\tau \to K_1\nu$ and $B \to J/\psi K_1$ decays would provide clean samples of K_1 mesons, without the additional complication of background from near-threshold enhancements of diffractive origin.

The analysis effort toward the extraction of the CKM angle α from the $B^0 \to a_1(1260)^{\pm}\pi^{\mp}$ channel started in 2006 with the measurement of the $B^0 \to a_1(1260)^{\pm}\pi^{\mp}$ decay channel, that was observed with a sufficiently high branching fraction to allow the study of the time distribution of the decays. The first step consisted in determining the effective value of α from the time-dependent analysis of *CP*-violating asymmetries in $B^0 \to a_1(1260)^{\pm}\pi^{\mp}$ decays. In this work, we have combined the results of the branching fraction measurements presented in this dissertation with the measurements - performed by *BABAR* - of the $B^0 \to a_1^{\pm}\pi^{\mp}$, $B^0 \to a_1^{-}K^{+}$, and $B^+ \to a_1^0\pi^+$ branching fractions to derive bounds on the penguin-induced shifts of the effective value of the CKM angle α, thus yielding an independent estimate for the CKM angle α

$$\alpha = (79 \pm 7 \pm 11)^{\circ}. \tag{6.20}$$

Finally, we have concluded the dissertation by assessing the impact on the precision of α of additional sources of SU(3) breaking, other than the ones considered in the Gronau and Zupan model, which is found to be of order 3°.

An interesting feature of the measurement of α from these channels is the fact that a sufficient number of observables can be extracted from the analysis of B decays to final states consisting of charged tracks only (i.e., $\pi^+\pi^-\pi^+\pi^-$ and $K^+\pi^-\pi^+\pi^-$), so that measurement at hadron collider experiments (e.g., LHCb) is not a priori precluded.

This work has been published in Phys. Rev. D81, 052009 (2010).

Acknowledgements

My gratitude must begin with my advisor, Professor Fernando Palombo. He has been incredibly supportive of my scientific pursuits, and I am very grateful for the many opportunities he has offered me during my graduate work, particularly in the areas of data analysis and presentation of scientific results.

I am cheerfully thankful to the junior members of the *BABAR* group at University of Milan, Alfio "Free Bird" Lazzaro and Vincenzo "De Chirico" Lombardo, and to the former and present fellow graduate students: Pietro "MB" Biassoni, Alessandro "Yogi" Berra, Paolo "QuadCuore" Gandini, Gio "Banana" Cerizza, Ricky "Kolf" Pellegrini, and - dulcis in fundo - Alessandra "Brenda" Colnago. Their friendship and help made life and work considerably easier, more fun, and more funny.

I extend my appreciation to Giovanni Calderini, Riccardo Cenci, Marco Bomben, Silvano Tosi, Emmanuele Salvati, Antonio Ceseracciu, and Tina Cartaro, who made me feel welcome during my first days at SLAC as a summer student working on *BABAR*. I feel a similar sentiment for my fellow summer students, in particular for Vito Lombardo and Alessandro Buzzatti, without whom the (two) San Diego days wouldn't have been that fun; and for Paolo Franchini and Nicola Gagliardi, who introduced me to the joys of properly served fast food.

I wish to thank all of the members of the *BABAR* Quasi-Two-Body, Quarkonium and $\Upsilon(3S)$ Working Groups, and the conveners Adrian Bevan, Bryan Fulsom, Alessandro Gaz, Claudia Patrignani, Steve Sekula, Jim Smith, and Veronique Ziegler. I would also like to extend my thanks to the members of the *BABAR* review committees that oversaw my works: Denis Bernard, William Ford, Bill Gary, Matt Graham, Walt Innes, and Antimo Palano. Their insight and help have been very important to me in my explorations of B meson and heavy quarkonium physics. I am especially indebted to Ian Aitchison, who patiently shared his knowledge and expertise.

Finally, I would like to thank my thesis referee Daniele Pedrini for his time and useful suggestions.

I could not have achieved this milestone without the support and companionship of my friends and loved ones outside the field. Thank you for your kind fellowship.

Bibliography

[1] S. L. Glashow, Nucl. Phys. **B22** 579 (1961); S. Weinberg, Phys. Rev. Lett. **19**, 1264 (1967); A. Salam, in *Elementary Particle Theory*, ed. N. Svartholm, (Almqvist and Wiksell, Stockholm, 1968) p. 367.

[2] N. Cabibbo, Phys. Rev. Lett. **10**, 531 (1963).

[3] M. Kobayashi and T. Maskawa, Prog. Theor. Phys. **49**, 652 (1973).

[4] L. L. Chau and W. Y. Keung, Phys. Rev. Lett. **53**, 1802 (1984).

[5] C. Amsler *et al.* [Particle Data Group], Phys. Lett. **667B**, 1 (2008).

[6] L. Wolfenstein, Phys. Rev. Lett. **51**, 1945 (1983).

[7] I. I. Bigi *et al.*, in *CP Violation*, ed. C. Jarlskog, (World Scientific, Singapore, 1992).

[8] E. Barberio *et al.* [Heavy Flavor Averaging Group], *Averages of b-hadron and c-hadron Properties at the End of 2007* [arXiv:0808.1297] and online update at `http://www.slac.stanford.edu/xorg/hfag`.

[9] R. Fleischer, Z. Phys. C **62**, 81 (1994); N. G. Deshpande and X.-G. He, Phys. Lett. **336B**, 471 (1994).

[10] B. Aubert *et al.* [*BABAR* Collaboration], Phys. Rev. D **79**, 072009 (2009).

[11] K.-F. Chen *et al.* [Belle Collaboration], Phys. Rev. Lett. **98**, 031802 (2007).

[12] H. Sahoo *et al.* [Belle Collaboration], Phys. Rev. D **77**, 091103 (2008).

[13] B. Aubert *et al.* [*BABAR* Collaboration], Phys. Rev. D **71**, 023005 (2005).

[14] Y. Grossman and M. P. Worah, Phys. Lett. **395B**, 241 (1997); D. London and A. Soni, Phys. Lett. **407B**, 61 (1997); M. Ciuchini *et al.*, Phys. Rev. D **79**, 978 (1997).

[15] Andreas Höcker and Zoltan Ligeti, Ann. Rev. Nucl. Part. Sci. **56**, 501 (2006).

[16] B. Aubert *et al.* [*BABAR* Collaboration], Phys. Rev. D **79**, 052003 (2009).

[17] M. Gronau and D. London, Phys. Lett. **253B**, 483 (1991); M. Gronau and D. Wyler, Phys. Lett. **265B**, 172 (1991).

[18] D. Atwood, I. Dunietz, and A. Soni, Phys. Rev. D **63**, 036005 (2001).

[19] A. Giri, Y. Grossman, A. Soffer and J. Zupan, Phys. Rev. D **68**, 054018 (2003).

[20] A. Bevan *et al.* [UTfit Collaboration], online update at `http://www.utfit.org`.

[21] B. Aubert *et al.* [*BABAR* Collaboration], arXiv:0807.4226 [hep-ex] (2008).

[22] S. Ishino *et al.*, arXiv:hepex/0703039 (2007).

[23] M. Gronau and D. London, Phys. Rev. Lett. **65**, 3381 (1990).

[24] A. L. Kagan, Phys. Lett. **601B**, 151 (2004).

[25] A. F. Falk, Z. Ligeti, Y. Nir, and H. Quinn, Phys. Rev. D **69**, 011502 (2004).

[26] B. Aubert *et al.* [*BABAR* Collaboration], Phys. Rev. D **76**, 052007 (2007).

[27] B. Aubert *et al.* [*BABAR* Collaboration], Phys. Rev. D **78**, 071104 (2008).

[28] B. Aubert *et al.* [*BABAR* Collaboration], Phys. Rev. Lett. **102**, 141802 (2009).

[29] B. Aubert *et al.* [*BABAR* Collaboration], Phys. Rev. Lett. **97**, 261801 (2006).

[30] M. Gronau and J. Zupan, Phys. Rev. D **70**, 074031 (2004).

[31] A. E. Snyder and H. R. Quinn, Phys. Rev. D **48**, 2139 (1993).

[32] B. Aubert *et al.* [*BABAR* Collaboration], Phys. Rev. D **76**, 012004 (2007).

[33] B. Aubert *et al.* [*BABAR* Collaboration], Phys. Rev. Lett. **98**, 181803 (2007).

[34] B. Aubert *et al.* [*BABAR* Collaboration], Phys. Rev. Lett. **97**, 051802 (2006).

[35] B. Aubert *et al.* [*BABAR* Collaboration], Phys. Rev. Lett. **100**, 051803 (2008).

[36] M. Gronau and J. Zupan, Phys. Rev. D **73**, 057502 (2006).

[37] M. Gronau and J. L. Rosner, Phys. Lett. **595B**, 339 (2004).

[38] M. Beneke, M. Gronau, J. Rohrer, and M. Spranger, Phys. Lett. **638B**, 68 (2006).

[39] B. Aubert *et al.* [*BABAR* Collaboration], Phys. Rev. D **76**, 052007 (2007).

[40] *PEP-II: An Asymmetric B Factory. Conceptual Design Report*, SLAC-R-418 (1993).

[41] `http://www.slac.stanford.edu/grp/cd/soft/images/pepii_lum.html`.

[42] `http://www-acc.kek.jp/kekb/Commissioning/Record/Luminosity_record.html`.

[43] B. Aubert *et al.* [*BABAR* Collaboration], Nucl. Instrum. Methods Phys. Res., Sect. A **479**, 1 (2002).

[44] G. W. Brandenburg *et al.*, Phys. Rev. Lett. **36**, 703 (1976).

[45] C. Daum *et al.* [ACCMOR Collaboration], Nucl. Phys. **B187**, 1 (1981).

[46] D. A. Bauer *et al.* [TPC/2γ Collaboration], Phys. Rev. D **50**, R13 (1994).

[47] R. Barate *et al.* [ALEPH Collaboration], Eur. Phys. Jour. C **11**, 599 (1999) [arXiv:hep-ex/9903015].

[48] G. Abbiendi *et al.* [OPAL Collaboration], Eur. Phys. Jour. C **13**, 197 (2000).

[49] D. M. Asner *et al.* [CLEO Collaboration], Phys. Rev. D **62**, 072006 (2000) [arXiv:hep-ex/0004002].

[50] P. Gavillet *et al.* [Amsterdam-CERN-Nijmegen-Oxford Collaboration], Phys. Lett. **76B**, 517 (1978).

[51] S. Rodeback *et al.* [CERN-College de France-Madrid-Stockholm Collaboration], Z. Phys. C **9**, 9 (1981).

[52] R. Armenteros *et al.*, Phys. Lett. **9B**, 207 (1964).

[53] A. Astier *et al.*, Nucl. Phys. **B10**, 65 (1969).

[54] L. S. Geng, E. Oset, L. Roca, and J. A. Oller, Phys. Rev. D **75**, 014017 (2007).

[55] G. Goldhaber, Phys. Rev. Lett. **19**, 976 (1967).

[56] R. K. Carnegie *et al.*, Phys. Lett. **68B**, 287 (1977).

[57] H. J. Lipkin, Phys. Lett. **72B**, 249 (1977).

[58] S. Meshkov, C. A. Levinson, and H. J. Lipkin, Phys. Rev. Lett. **10**, 361 (1963).

[59] M. Suzuki, Phys. Rev. D **47**, 1252 (1993).

[60] H.-Y. Cheng, C.-K. Chua, and C.-W. Hwang, Phys. Rev. D **69**, 074025 (2004).

[61] H. Y. Cheng and C. K. Chua, Phys. Rev. D **69**, 094007 (2004)

[62] M. Suzuki, Phys. Rev. D **55**, 2840 (1997)

[63] D. M. Asner *et al.* [BESIII Collaboration], Int. J. Mod. Phys. **A24**, supplement 1, 327 (2009).

[64] K. Abe *et al.* [Belle Collaboration], Phys. Rev. Lett. **87**, 161601 (2001) [arXiv:hep-ex/0105014].

[65] H. Yang *et al.* [Belle Collaboration], Phys. Rev. Lett. **94**, 111802 (2005).

[66] B. Aubert *et al.* [*BABAR* Collaboration], Phys. Rev. Lett. **101**, 161801 (2008).

[67] H. Albrecht *et al.* [ARGUS Collaboration], Phys. Lett. **254B**, 288 (1991).

[68] J. Adler *et al.* [MARK-III Collaboration], Phys. Rev. Lett. **64**, 2615 (1990).

[69] D. Coffman *et al.* [MARK-III Collaboration], Phys. Rev. D **45**, 2196 (1992).

[70] V. Laporta, G. Nardulli, and T. N. Pham, Phys. Rev. D **74**, 054035 (2006); **76**, 079903 (2007).

[71] G. Calderon, J. H. Munoz, and C. E. Vera, Phys. Rev. D **76**, 094019 (2007).

[72] H.-Y. Cheng and K.-C. Yang, Phys. Rev. D **76**, 114020 (2007).

[73] B. Aubert *et al.* [*BABAR* Collaboration], Phys. Rev. D **76**, 012004 (2007).

[74] S. Agostinelli *et al.*, Nucl. Instrum. Methods Phys. Res., Sect. A **506**, 250 (2003).

[75] J. D. Richman, *An Experimenters Guide to the Helicity Formalism*, CALT-68-1148 (1984).

[76] D. J. Herndon, P. Soding, and R. J. Cashmore, Phys. Rev. D **11**, 3165 (1975).

[77] D. Aston, T. A. Lasinski, P. K. Sinervo, *The SLAC Three-Body Partial Wave Analysis System*, SLAC-R-287 (1985).

[78] K. Peters, Int. J. Mod. Phys. **A21**, 5618 (2006).

[79] I. J. R. Aitchison, Nucl. Phys. **A189**, 417 (1972).

[80] R. L. Kelly *et al.* [Particle Data Group], Rev. Mod. Phys. **52**, S1 (1980).

[81] C. Daum *et al.* [ACCMOR Collaboration], Nucl. Phys. **B182**, 269 (1981).

[82] M. G. Bowler, J. B. Dainton, A. Kaddoura, and I. J. R. Aitchison, Nucl. Phys. **B74**, 493 (1974).

[83] J. M. Blatt and V. F. Weisskopf, *Theoretical Nuclear Physics* (John Wiley and Sons, New York, 1952).

[84] M. Nauenberg and A. Pais, Phys. Rev. **126**, 360 (1961).

[85] M. G. Bowler, M. A. V. Game, I. J. R. Aitchison, and J.B. Dainton, Nucl. Phys. **B97**, 227 (1975).

[86] M. G. Bowler, J. Phys. **G3**, 775 (1977); 1503 (1977).

[87] U. Amaldi, M. Jacob, and G. Matthiae, Ann. Rev. Nucl. Sci. **26**, 385 (1976).

[88] R. T. Deck, Phys. Rev. Lett. **13**, 169 (1964).

[89] L. Stodolsky, Phys. Rev. Lett. **18**, 973 (1967).

[90] M. G. Bowler, J. Phys. **G5**, 203 (1979).

[91] C. Daum *et al.* [ACCMOR Collaboration], Phys. Lett. **89B**, 281 (1980).

[92] A. C. Irving, J. Phys. **G6**, 153 (1980).

[93] K. W. J. Barnham *et al.*, Nucl. Phys. **B25**, 49 (1970).

[94] D. Lange *et al.*, Nucl. Instrum. Methods Phys. Res., Sect. A **462**, 152 (2001).

[95] A. de Rùjula, J. Ellis, E. G. Floratos, and M. K. Gaillard, Nucl. Phys. **B138**, 387 (1978).

[96] T. Sjostrand, Comput. Phys. Commun. **82**, 74 (1994).

[97] H. Albrecht *et al.* [ARGUS Collaboration], Phys. Lett. **241B**, 278 (1990).

[98] V. Lombardo, *Branching Fractions in B^0 Meson Decays to $a_1(1260)^{\pm}\pi^{\mp}$ and $a_1(1260)^{-}K^{+}$* (Ph.D. Thesis, Università degli Studi di Milano, 2006).

[99] K. S. Cranmer, Comput. Phys. Commun. **136**, 198 (2001).

[100] S. Stracka, *Search for B^0 decays to $K_1(1270)^{\pm}\pi^{\mp}$ and $K_1(1400)^{\pm}\pi^{\mp}$ with the BABAR experiment* (M.Sc. Thesis, Università degli Studi di Milano, 2007).

[101] M. Pivk and F. R. Le Diberder, Nucl. Instrum. Methods Phys. Res., Sect. A **555**, 356 (2005).

[102] D. Aston *et al.* [LASS Collaboration], Nucl. Phys. **B296**, 493 (1988).

[103] J. C. R. Bloch, Yu. L. Kalinovsky, C. D. Roberts, and S. M. Schmidt, Phys. Rev. D **60**, 111502(R) (1999).

[104] K.-C. Yang, Nucl. Phys. **B776**, 187 (2007).

[105] G. Nardulli and T. N. Pham, Phys. Lett. **623B**, 65 (2005).

[106] H.-Y. Cheng, Phys. Rev. D **67**, 094007 (2003).